NTNU

Norwegian University of
Science and Technology

The effect of Ni-contents above 1% in low alloy steels (LAS) on the susceptibility to hydrogen embrittlement (HE)

Philip Haakon Wagstaff

Subsea Technology
Submission date: June 2017
Supervisor: Roy Johnsen, MTP

Norwegian University of Science and Technology
Department of Mechanical and Industrial Engineering

Abstract

Low alloy ferrite-pearlite steels with 0, 1, 2, and 3 wt% Ni were tested to evaluate the effect of exceeding the 1 wt% Ni (Nickel) restriction in ISO 15156:2. A literature survey was conducted to document the history of the Ni-restriction, hydrogen embrittlement of ferrite-pearlite steels, and existing literature on hydrogen embrittlement of ferrite-pearlite steels with Ni.

The materials were characterized by their overall microstructures, average grain sizes, relative fractions of pearlite, and the interlamellar spacing of pearlite. One of each alloy was tested in an ambient environment, two of each alloy were tested in a 3.5 wt% NaCl-solution with potentiostatic hydrogen charging, and two of each alloy were tested in a 3.5 wt% NaCl-solution with galvanostatic hydrogen charging. The irreversible trapping behaviour of the 0 wt% Ni and 3 wt% Ni samples were evaluated by charging them with hydrogen and storing them in a desiccator for 11 days before slow strain rate testing them. The surfaces and side views of all the tested specimens were examined by use of scanning electron microscopy (SEM).

Using potentiostatic charging, the alloys with 0 wt% Ni were seen to be least susceptible to hydrogen embrittlement. However, the alloys with 1 wt% Ni were only slightly more susceptible, and there were no major differences in the susceptibilities of the samples with 1, 2, and 3 wt% Ni.

With galvanostatic charging, a higher current was used, and the samples with higher Ni-contents were seen to be more susceptible to hydrogen embrittlement. When isolating the effects of the studied microstructural features and comparing them with other studies, the increased susceptibilities of the Ni-containing samples were deemed to be higher than what would have been expected.

In the test series where the irreversible trapping behaviour was evaluated, the alloy with 3 wt% Ni was seen to cause more irreversible trapping of hydrogen than the alloy with 0 wt% Ni. However, it was unclear whether this was due to the increased pearlite fraction of the sample with 3 wt% Ni.

For all alloys tested, the embrittling behaviour could be classified as a loss in tensile ductility. No differences were found in the fracture morphologies of the samples. In the Ni-free alloy, there were more secondary cracks along the gauge area. However, the cracks in the Ni-containing alloys were more severe.

Sammendrag

Lavlegerte stål med mikrostrukturer bestående av ferritt og perlitt ble testet ved bruk av SSRT (strekktesting med lav tøyningsrate) for å evaluere påvirkningen av Nikkel (Ni) på mottageligheten til hydrogensprøhet. Ferritt-perlitt-stål med 0, 1, 2 og 3 wt% Ni ble testet. Dette ble gjort fordi det er fastslått i ISO 15156:2 at Ni-konsentrasjoner over 1 wt% (vektprosent) i stål øker mottageligheten til hydrogensprøhet, og følgelig at de ikke kan brukes i sure olje- og gassmiljøer. Litteratursøk ble gjennomført for å dokumentere bakgrunnen av Ni-restriksjonen, og for å finne lignende studier av hydrogensprøhet av ferritt-perlitt-stål, både med og uten Ni.

Stålene ble karakteriserte ved å vurdere mikrostrukturene, de gjennomsnittlige kornstørrelsene, perlittmengdene og avstanden mellom sementittlinjene i perlittkornene. En av hver legering ble testet i luft, to av hver legering ble testet i en 3.5 wt% NaCl-løsning med hydrogenlading ved konstant spenning, og to av hver legering ble testet i en 3.5 wt% NaCl-løsning med hydrogenlading ved konstant strøm på prøvene. For å vurdere ulikheter ved materialenes evne til å lagre hydrogen, ble legeringen med 0 og 3 wt% ladet opp med hydrogen, for så å plassere dem i en eksikkator i 11 døgn før de ble testet via SSRT. Sidebilder og bruddflatebilder ble tatt av alle prøver via sveipelektronmikroskopi (SEM).

I testseriene hvor konstant potensiale ble brukt, var prøven med 0 wt% Ni minst mottagelig til hydrogensprøhet. Likevel var prøven med 1 wt% bare marginalt mer mottagelig enn prøven med 0 wt% Ni, og det var ingen store forskjeller mellom mottagelighetene til prøvene med 1, 2 og 3 wt% Ni.

I testseriene hvor konstant strøm ble brukt, ble det også brukt en høyere strømtetthet. I alle disse testene var prøvene med 0 wt% Ni minst mottagelige, mens mottagelighetene til de andre prøvene økte med Ni-konsentrasjonen. Ved å sammenligne endringene i mikrostrukturene med lignende studier fra litteraturen, ble det konkludert at økningene i mottagelighetene til stålene med Ni var større enn det de isolerte effektene skulle tilsi.

I testene hvor materialenes evner til å lagre hydrogen ble evaluert, ble det konkludert at stålet med 3 wt% Ni hadde mer lagret hydrogen enn stålet med 0 wt% Ni. Det var imidlertid uklart hvorvidt dette skyldtes den forhøyede perlittmengden i stålet med 3 wt% Ni, eller om det var en direkte konsekvens av Ni.

Hydrogensprøheten som ble observert i alle materialene kunne klassifiseres som tap av duktilitet. Ingen forskjeller ble observert i bruddmekanismemorfologiene mellom prøvene med og uten Ni. I prøven med 0 wt% Ni ble det observert mange små sprekker langs siden. I alle prøvene som inneholdt Ni ble det funnet færre sprekker, men blant de som ble funnet var det større sprekker, som ble ansett som mer kritiske.

Preface

This master thesis is submitted to NTNU as part of the Master's degree program in Subsea Technology, and was written at the Department of Mechanical and Industrial Engineering. Professor Roy Johnsen has supervised this work.

I would like to thank GE Oil & Gas for supplying the steel samples, and for their enthusiasm and advice regarding the experimental work. I would also like to thank Cormet for their detailed replies to any questions about using and troubleshooting their equipment.

I would like to thank my supervisor, Professor Roy Johnsen, for our productive meetings and discussions, and for helping with any unforeseen circumstances.

I would also like to express my gratitude to Nils-Inge J. Nilsen for showing me how to operate the slow strain rate testing machine, and for creating tools, components and practical solutions related to the hydrogen charging setup.

Finally, I would like to give very special thanks to Ph.D Hans Husby for his extensive assistance and guidance throughout the entirety of this work.

Trondheim, 11. of June 2017.

Philip H. Wagstaff

Table of Contents

List of abbreviations

AISI – American Iron and Steel Institute
ASTM – American Society for Testing and Materials
Ag/AgCl – Silver/Silver Chloride
Al – Aluminium
As2O3 – Arsenic Trioxide
CE – Counter Electrode
CLT – Constant Load Test
Cr – Chromium
DBTT – Ductile to Brittle Transition Temperature
DCB – Double-Cantilever Beam
EAC – Environmentally Assisted Cracking
GE – General Electric
H2S – Hydrogen Sulphide
H2SO4 – Sulphuric Acid
HE – Hydrogen Embrittlement
HER – Hydrogen Embrittlement Resistance
HIC – Hydrogen Induced cracking
HSC – Hydrogen Stress Cracking
ISO – International Organization for Standardization
LAS – Low Alloyed Steel
Mn – Manganese
NACE – National Association of Corrosion Engineers
NaCl – Sodium Chloride
NaOH – Sodium Hydroxide
Ni – Nickel
O – Oxygen
OCP – Open Circuit Potential
RA – Reduction in Area
REF – Reference (electrode)
S – Sulphur
SCC – Stress Corrosion Cracking
SEM – Scanning Electron Microscopy
SSC – Sulphide Stress cracking
SSR – Slow Strain Rate
SSRT – Slow Strain Rate Testing
WE – Working Electrode
Wt% - Weight Percent

1. Introduction

1.1 Background

The Ni (nickel) content in low alloy steels (LAS) for use in sour service is limited to 1 wt% by ISO 15156:2 [1], because of a suspicion that Ni reduces hydrogen embrittlement resistance. This is, however, based on controversial research [2], and GE Oil & Gas have initiated a project to challenge the restriction. They delivered LAS samples with Ni contents varying from 0 to 3 wt% for this thesis.

Increasing the Ni content in LAS improves the hardenability, strength, toughness, fatigue life and ductile-to-brittle transition temperature (DBTT), with a slight reduction of weldability. If it should become apparent that Ni concentrations over 1 wt% can be safely used in LAS without increasing HE susceptibility, then lifting the Ni restriction would be of great benefit to the industry, as it would allow for use of stronger and more durable alloys, which would be especially suited for arctic and high pressure oil and gas environments.

The aim of this thesis was to provide experimental results that would be of use in the ongoing endeavour of deciding whether the Ni restriction in ISO 15156:2 is justified or not. A series of LAS with similar ferrite-pearlite microstructures that had four different Ni contents – 0, 1, 2 and 3 wt% – were tested using slow strain rate testing (SSRT) in an ambient environment and in an environment with cathodic hydrogen charging. Two different hydrogen charging methods were used: potentiostatic (constant potential) and galvanostatic (constant current). In addition, the irreversible trapping behaviours of the 0 and 3 wt% Ni samples were compared by charging them both with hydrogen, and then storing them in a desiccator before starting SSRT. Scanning electron microscopy (SEM) was used to examine the surfaces and sides of all the fractured specimens.

The purpose of the experimental work was not to simulate the exact performance in a sour service environment, but rather to screen for differences in hydrogen embrittlement susceptibilities of ferrite-pearlite steels with increasing Ni contents. As will be reviewed in later sections, the premature cracking in sour service environments (sulphide stress cracking) is believed to occur due to hydrogen, thereby justifying the connection between hydrogen embrittlement susceptibility and sulphide stress cracking susceptibility.

2. Theoretical background

In this chapter, the required theoretical background for the experimental work will be looked at.

2.1 Mechanical Properties of Materials

There are two main mechanical properties that will be considered in this project: strength and ductility. In this section, strength and ductility will be defined, and various factors that influence these properties will be looked at.

2.1.1 Properties Obtained by Tension Testing

Tension testing is performed by utilizing a machine that elongates a sample at a constant rate, while simultaneously measuring the instantaneous force required to do so. The machine is usually connected to a computer that records all the data.

Figure 1 shows a typical test specimen that is used for tension testing. The threads fasten the sample in the machine's grips, whose uniaxial motion apply the force.

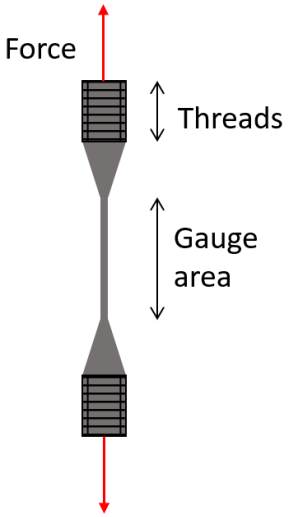

Figure 1 Tensile testing specimen

The measured force and elongation are used to calculate engineering stress (σ) and strain (ε), which are defined in *Equations 1* and *2*, respectively.

$$\sigma = \frac{F}{A} \qquad 1.$$

Where σ is in MPa, F is the force in N, and A is the initial cross-sectional area in mm^2.

$$\varepsilon = \frac{\Delta L}{L} \qquad 2.$$

Where ε is dimensionless, ΔL is the change in the gauge length, and L is the original gauge length.

Plotting stress as a function of strain produces a curve, known as a stress-strain curve. *Figure 2* shows an example of a typical stress-strain curve for a steel specimen.

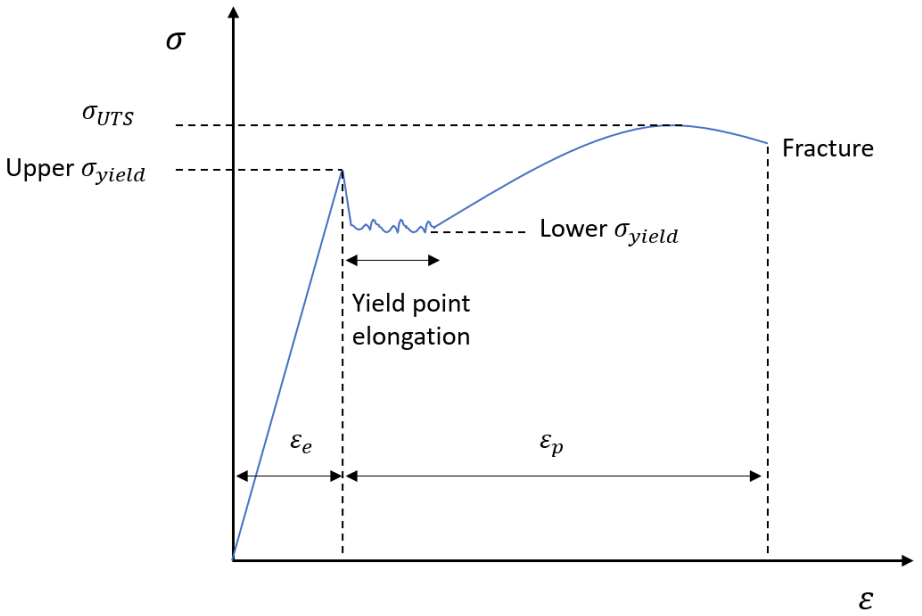

Figure 2 A typical stress-strain curve for steel

In the region marked as ε_e, all deformation is elastic, and will therefore be undone if the tension on the sample is released. The elastic behaviour can be described by Hooke's law, *Equation 3*.

$$\sigma = E\varepsilon \qquad 3.$$

E is the slope of the curve in the elastic region, and is known as the Young's modulus or as the Elastic modulus. This number gives a measure of the material's stiffness, and can be used to find the strain at a given stress, or vice versa, as long as it is in the elastic region.

If the stress exceeds the upper σ_{yield}, the material's yield strength, the strain will be in the plastic region, and the deformation that occurs there will be permanent. The stress increases up to a top point σ_{UTS}, which is the material's ultimate tensile strength. At this point, the reduction in cross-sectional area starts to limit the force that the material can sustain, and the curve descends until the sample fractures. The two pieces of the fractured specimen will then retract, effectively undoing the elastic strain.

Performing a tension test can give quantitative measures of ductility, which is the amount of plastic deformation a material can undergo before fracturing. The two main ductility parameters are Percent elongation and Reduction in cross sectional area. The relations for finding Percent elongation and Reduction in cross sectional area are shown in equations *4* and *5*, respectively.

$$\%EL = \left(\frac{l_f - l_0}{l_0}\right) * 100 \qquad 4.$$

Where l_f is the length of the gauge area at fracture and l_0 is the initial length of the gauge area.

$$\%RA = \left(\frac{A_0 - A_f}{A_0}\right) * 100 \qquad 5.$$

Where A_0 is the initial cross-sectional area, and A_f is the cross-sectional area measured at the point of fracture.

The figure includes a phenomenon called yield point elongation, which can be seen on the curve as a dip and a fluctuating line following the point of upper yield stress. This is common in ductile carbon steels and LAS, and can be described as the onset of an elastic to plastic transition that propagates through the length of the material. These lines of transition are called Lüder bands. This is illustrated in *Figure 3*.

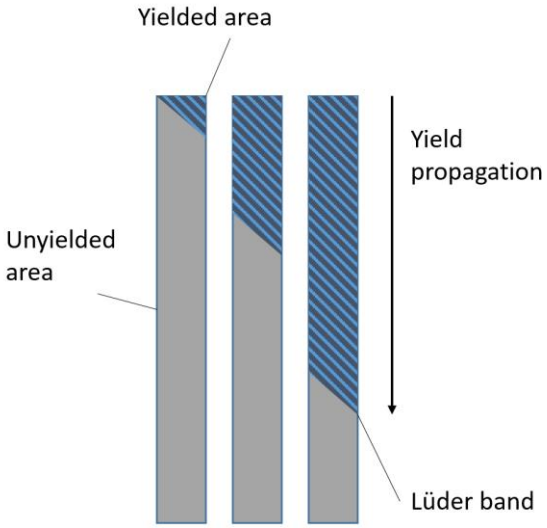

Figure 3 Lüder band

[3]

2.1.2 Ferrite-pearlite Steels – Production, Microstructure and Properties

The most common structural steels have mixed ferrite-pearlite microstructures. They are inexpensive, and can be produced with a wide range of mechanical properties to suit their applications. [4]

In its simplest form, a steel is made up of the elements iron (Fe) and carbon ©. The microstructure that develops depends on both the carbon content and the heat treatment it undergoes during production. A ferrite-pearlite steel typically has between 0.2 and 0.5 wt% carbon [5]. The heat treatment that forms the microstructure is shown in *Figure 4*.

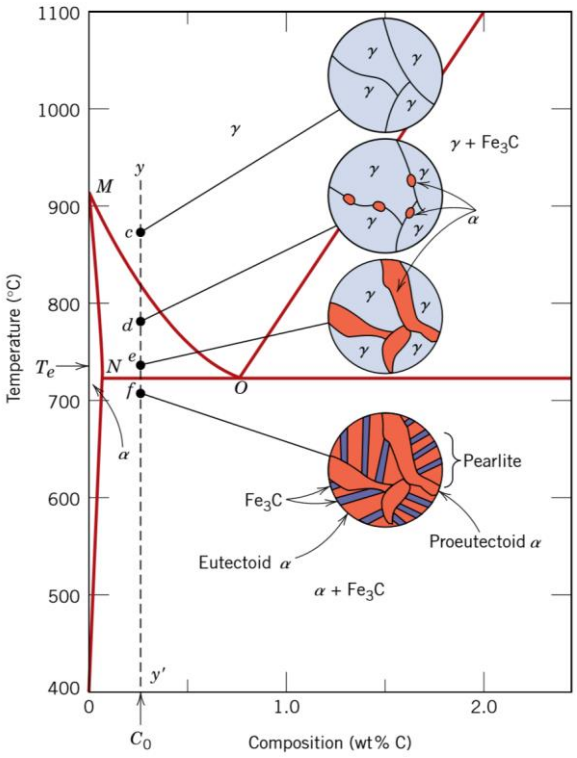

Figure 4 Formation of ferrite-pearlite microstructure. Picture from ref. [3]

The vertical line yy' in *Figure 4* represents slow cooling of a steel with approximately 0.25 wt% carbon, that has been heated at a temperature above the MO line. The circular images at the various points show the phases present in the microstructures at the current points. At point c, the microstructure consists of only the γ-phase, which is called austenite. The individual sections of austenite are the grains, and the edges separating them are the grain boundaries. As the steel is cooled to below the MO line, the ($\gamma + \alpha$) region is reached. At this point the α-phase, ferrite, starts to form along the austenite grain boundaries. The onset of this is illustrated at point d. At point e, the ferrite grains have grown larger and slightly richer in carbon, while the austenite grains are decreasing. The remaining austenite grains turn to pearlite as the temperature crosses the T_e line, the eutectoid temperature.

In the final microstructure in *Figure 4*, ferrite is present in both the ferrite and pearlite phases, as proeutectoid α and eutectoid α, respectively. The proeutectoid α is the ferrite formed in the ($\gamma + \alpha$) region, while the eutectoid α is the ferrite that was formed along with FeC_3 while crossing the eutectoid temperature. [3]

The relative fraction of pearlite can be calculated using the lever rule, *Equation 6*.

$$W_P = \frac{T}{T+U} = \frac{C_0' - 0.022}{0.76 - 0.022} = \frac{C_0' - 0.022}{0.738} \qquad 6.$$

Where W_P is the pearlite fraction, C_0' is the carbon content, T is the distance from the carbon solubility limit in ferrite (0.022) to C_0', and U is the distance from C_0' to the eutectoid point (0.76). This is illustrated in *Figure 5*.

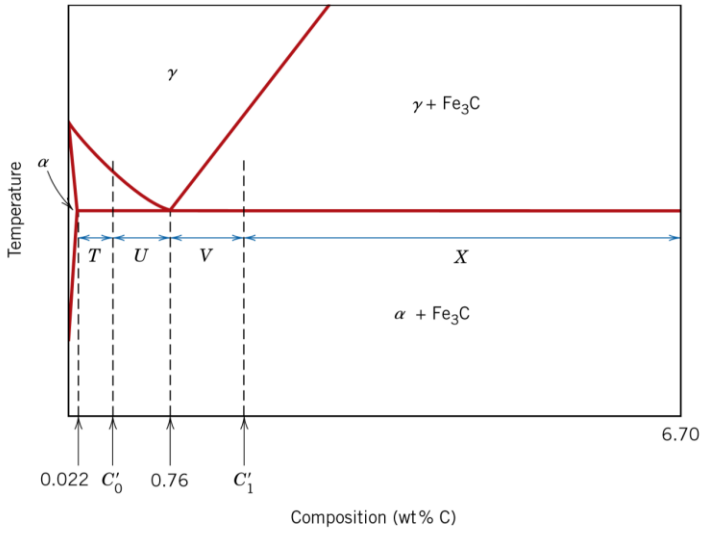

Figure 5 Illustration of points used in the lever rule. From ref. [3]

Figure 6 shows a picture of the microstructure of a ferrite-pearlite steel. The solid white areas are ferrite grains, and the white areas with lamellar black lines are pearlite grains. The edges separating the grains are grain boundaries

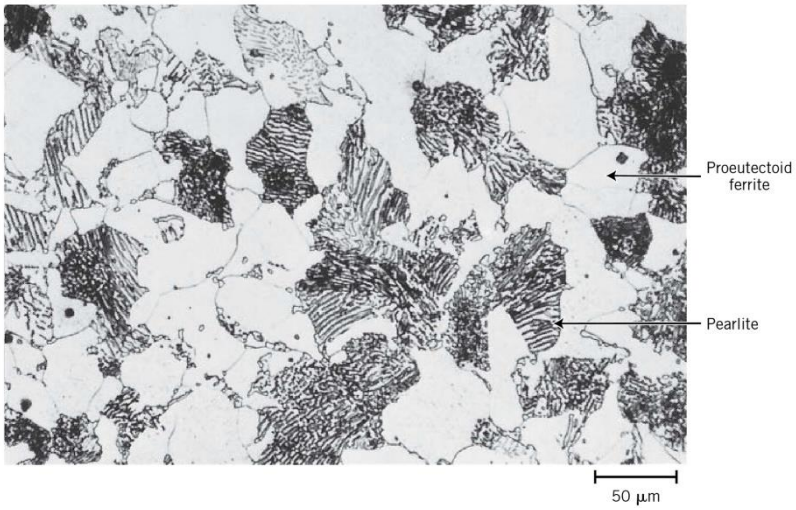

Figure 6 Microstructure of a ferrite-pearlite steel with 0.38 wt% carbon. From ref. [3]

Ferrite properties

The ferrite phase is a solid solution of iron containing carbon or one or more alloying elements, with atoms arranged in a body centred cubic (BCC) structure, as illustrated in *Figure 7*. Alloying elements can be part of the structure in two different ways: interstitial and substitutional. The interstitial elements are those that are small enough to fit in between the iron atoms, such as carbon and

nitrogen, while the substitutional elements are those that are large enough to replace an iron atom in the structure, such as chromium, nickel and manganese. [4]

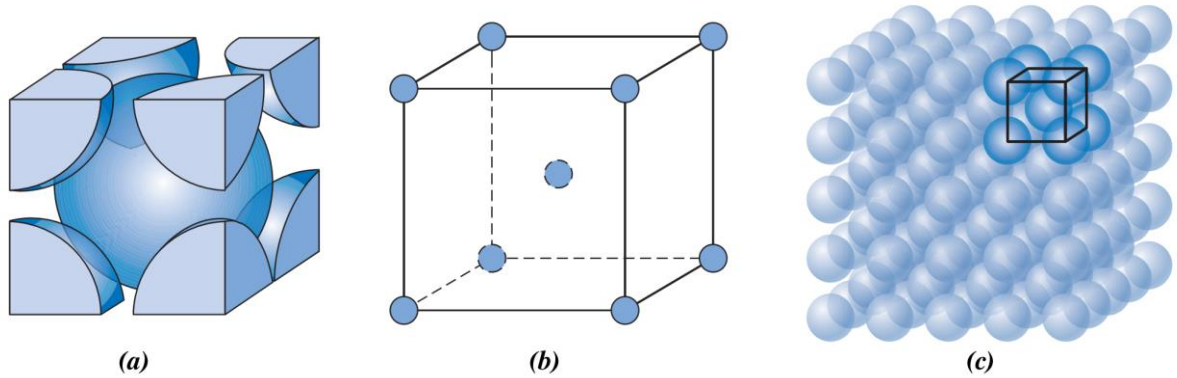

Figure 7 BCC structure illustrated in three different ways: (a), a hard-sphere unit cell, (b) a reduced sphere unit cell and (c) an aggregate of many atoms. From ref. [3]

Compared with other phases, ferrite is relatively soft, relatively weak, and highly ductile; a fully ferritic material will typically fail at an elongation of over 50% [4]. There are two main factors that influence the strength of a ferrite: alloying elements and the grain size.

The influence of some alloying elements on ferrite's yield strength is shown in *Figure 8*. The interstitial elements give a larger strength increase than the substitutional elements.

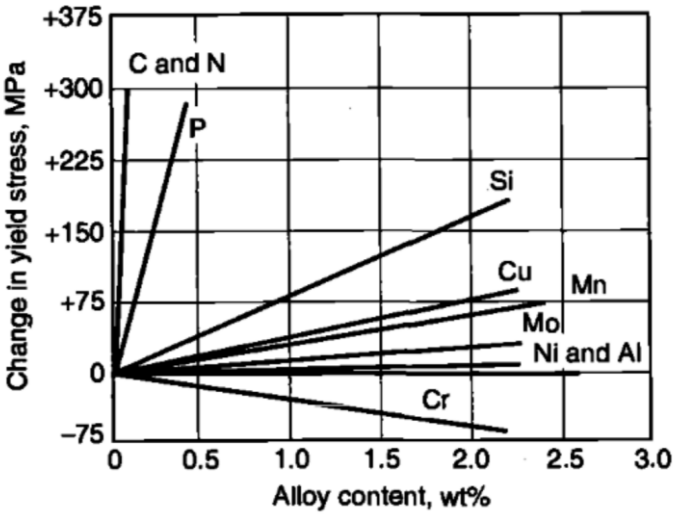

Figure 8 Influence of alloying elements on a ferritic steel's yield strength. From ref. [4]

The effect of the ferrite grain size is determined by the Hall-Petch relationship, as seen in *Equation 7.*

$$\sigma_y = \sigma_0 + \frac{k_y}{\sqrt{d}} \qquad 7.$$

Where σ_y is the yield strength, σ_0 is a constant, k_y is a constant and d is the grain size in m. [4] The yield strength increases as grain size decreases. For mild steel, $\sigma_0 = 70\ MPa$ and $k_y = 0.74\ MPa\sqrt{m}$ [6].

Pearlite properties

The pearlite phase consists of ferrite with layers of cementite (FeC_3) that form lamellar lines, as seen in *Figure 9.* This is essentially a composite microstructure, with the ferrite being soft and ductile, and the cementite hard and brittle.

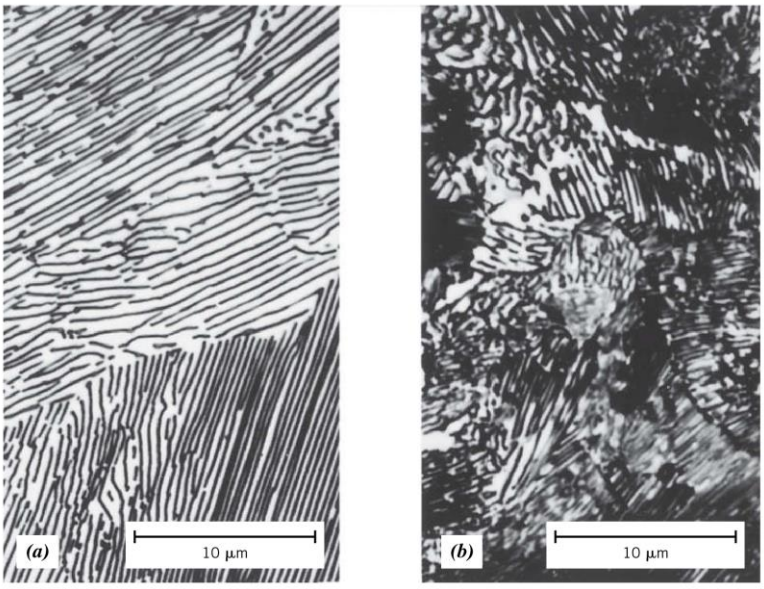

Figure 9 (a) is coarse pearlite, and (b) is fine pearlite. The white areas are ferrite, and the black lines are cementite (FeC_3). In (b), the lines are thinner and closer together, making them appear as solid black areas. From ref. [3]

The pearlite phase is strong, but brittle. A fully pearlitic steel will typically fail at an elongation of 10% [4]. The main factor that governs the yield strength is the interlamellar spacing, λ, which is the distance between the cementite lines. A simple relationship for the yield strength of a fully pearlitic steel as a function of λ is shown in *Equation 8.*

$$\sigma_y = -85.9 + \frac{8.3}{\sqrt{\lambda}} \qquad 8.$$

Where σ_y is the yield strength in MPa, and λ is the interlamellar spacing in mm. This relationship shows that the yield strength will increase as λ decreases.

It has also been shown that the pearlite colony and prior austenite grain sizes affect the yield strength. Hyzak and Bernstein proposed the relationship seen in *Equation 9.* [4]

$$\sigma_y = 52.3 + \frac{2.18}{\sqrt{\lambda}} - \frac{0.4}{\sqrt{d_c}} - \frac{2.88}{\sqrt{d}} \qquad 9.$$

Where σ_y is the yield strength, λ is the interlamellar spacing, d_c is the pearlite colony size and d is the prior austenite grain size. The yield strength will increase when λ decreases, or when d_c and/or d increase.

Equations 8 and 9 do not include the effects of alloying elements. Alloying elements can strengthen the ferrite in the lamellar structure, but not the cementite. Most of the strength in pearlite comes from the cementite.

Ferrite-pearlite properties

For a ferrite-pearlite steel, the mechanical properties will be a combination of those seen in the ferrite and pearlite phases. *Figure 10* shows the effect of increasing carbon content. As the carbon content increases, the fraction of pearlite also increases. As can be seen on the figure, the ultimate tensile strength increases more than the yield strength does when the fraction of pearlite increases. This is because yielding is controlled mainly by ferrite, the continuous phase in the microstructure. Pearlite plays only a minor role in the yielding behaviour. The ductility decreases as the fraction of pearlite increases.

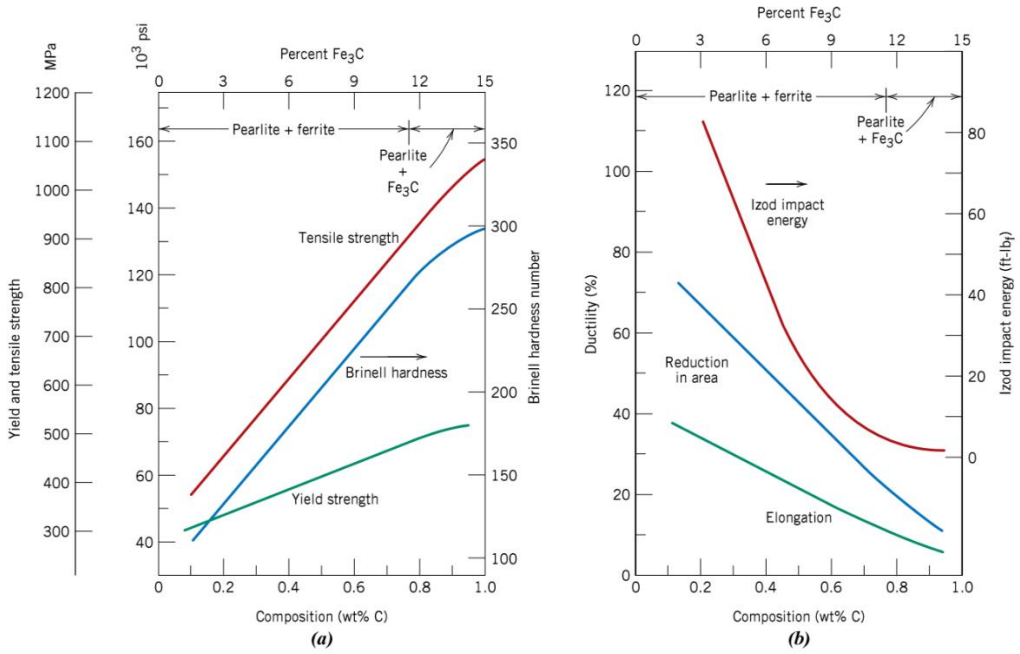

Figure 10 Effect of carbon content on ferrite-pearlite steels. (a) shows strength and hardness and (b) shows ductility. From ref. [3]

There are various equations that are used to relate the strength of ferrite-pearlite steels to microstructural features, such as grain size and pearlite fraction. One such equation for the yield strength of a ferrite-pearlite steel with a carbon content of under 0.25 wt% is given in *Equation 10.*

$$\sigma_y = 53.9 + 32.34 * Mn + 83.2 * Si + 354.2 * \left(N_f\right) + \frac{17.4}{\sqrt{d}} \qquad 10.$$

Where σ_y is the yield strength in MPa, Mn is the Mn content in wt%, Si is the Si content in wt%, $\left(N_f\right)$ is the free nitrogen content (which is usually less than 0.01 wt%) and d is the ferrite grain size. It should be noted that carbon content – and followingly the pearlite fraction – is not included in the equation. This is because the ferrite phase, as stated above, is what determines yielding behaviour. However, as seen in *Figure 10*, the yield strength will in fact be increased somewhat due to the addition of carbon, but this is not considered in the equation

A similar expression for the ultimate tensile strength is given in *Equation 11.*

$$UTS = 294.1 + 27.7 * Mn + 83.2 * Si + 3.9 * (P) + \frac{7.7}{\sqrt{d}} \qquad 11.$$

Where UTS is the tensile strength in MPa, Mn is the Mn content in wt%, Si is the Si content in wt%, (P) is the pearlite content in %, and d is the ferrite grain size. It should be noted that the pearlite content is included here, and that the ferrite grain size plays a smaller role than it does for the yield strength. [4]

2.1.3 Effect of Nickel in Ferrite-pearlite Steels

Kappes et al. [2] published a review in 2014, where the effects of Ni on microstructure, processing and mechanical properties on LAS were studied. Their findings are summarized below.

Austenite transformation

Nickel is an austenite stabilizer, which means that it increases the temperature range where austenite is stable during heat treatment. This can be seen on the Fe-C diagram, in that Ac_1 and Ac_3 decrease, as illustrated in *Figure 11*.

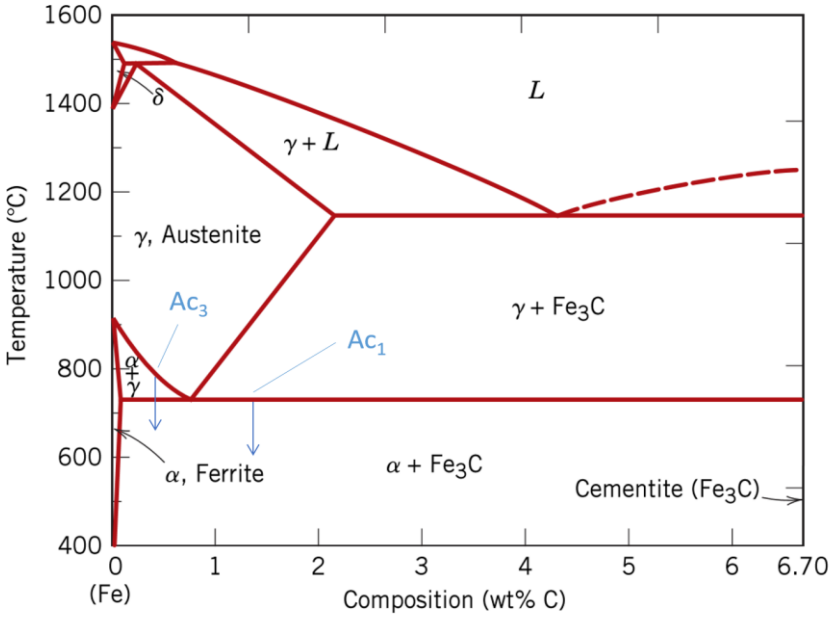

Figure 11 Fe-C diagram. From ref. [3]

Ac_1 and Ac_3 for LAS are most commonly determined by the relationships in *Equations 12* and *13*, which are valid for C < 0.6 wt%, Cr < 5 wt%, Ni < 5 wt%, W < 4.1 wt%, and Mo < 5.4 wt%.

$$Ac_1 = 723 - 10.7 * Mn - 16.9 * Ni + 29.1 * Si + 16.9 * Cr + 290 * As + 6.38 * W \quad 12.$$

$$Ac_3 = 910 - 203 * \sqrt{C} - 15.2 * Ni + 44.7 * Si + 104 * V + 31.5 * Mo + 13.1 * W \quad 13.$$

Where Ac_1 and Ac_3 are in degrees Celsius, and the elements are in wt%.

Furthermore, the addition of Ni causes the carbon content in the eutectoid point to decrease, thereby shifting the eutectoid point to the left, increasingly so with increasing Ni-contents, as shown in *Figure 12*.

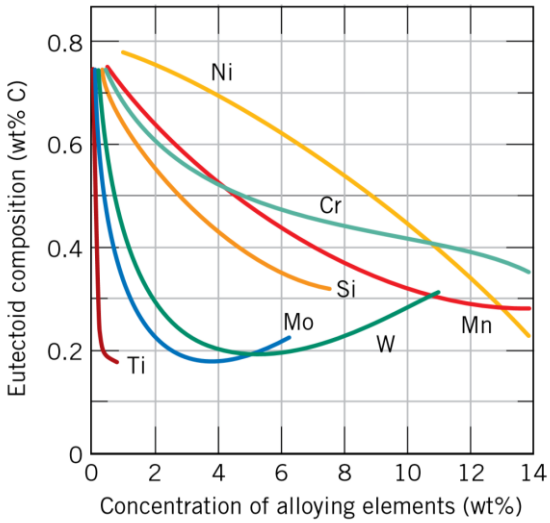

Figure 12 Influence on alloying elements on eutectoid composition. From ref. [3]

The combined effects of the movement of Ac_1, Ac_3 and the eutectoid point have been used to make the plot in *Figure 13*, which shows the difference between the Fe-C diagram of a 0 wt% and 3 wt% Ni steel.

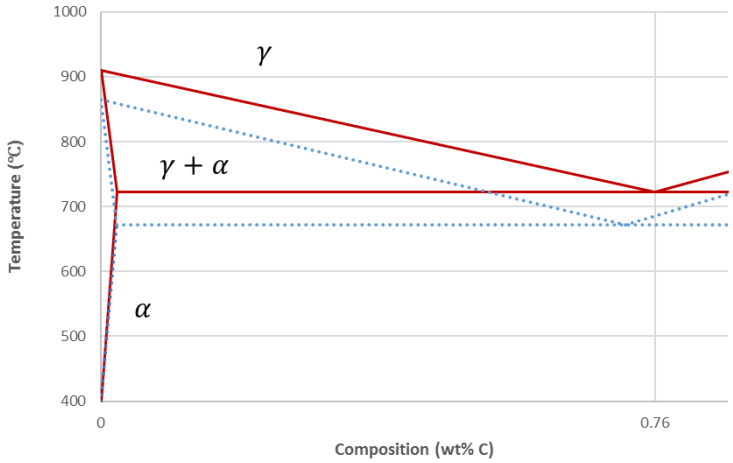

Figure 13 Plot of an Fe-C diagram for a 0 wt% Ni (red line) and 3 wt% Ni (blue dotted line) steel.

For a ferrite-pearlite steel, the shift in eutectoid composition causes the relative fraction of pearlite in the microstructure to increase.

Hardenability

The addition of Ni increases hardenability in steel, which is the ability to delay diffusion controlled processes during cooling of austenite. This is best shown using a Time-Temperature-Transformation (TTT) diagram, as in *Figure 14*.

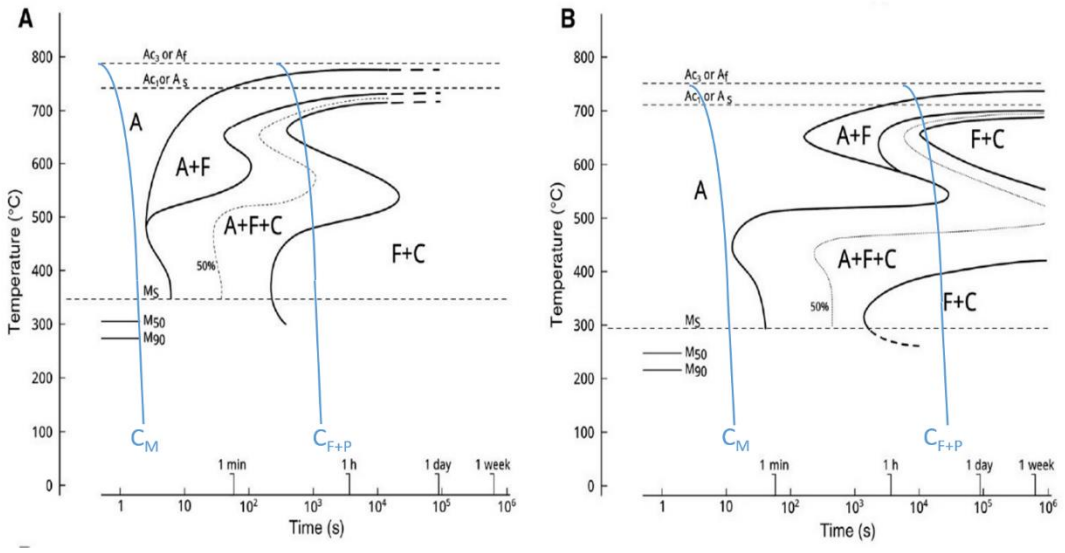

Figure 14 TTT diagrams for LAS without (A) and with (B) nickel. The superimposed blue lines represent differing cooling rates with subscripts that denote the respective microstructures that would be produced. A is austenite, M is martensite, F is ferrite and P is pearlite.

Steel A is UNS G41400 (SAE/AISI 4140) with 0.37 wt% C, 0.77 wt% Mn, 0.98 wt% Cr and 0.21 wt% Mo. Steel B is UNS G43400 (SAE/AISI 4340) with 0.42 wt% C, 1.79 wt% Ni, 0.78 wt% Mn, 0.80 wt% Cr and 0.33 wt% Mo. Figure from ref. [2]

Figure 14 shows two different steels with similar compositions, except for Ni content; steel A having 0 and steel B having 1.79 wt% Ni. Following one of the blue cooling lines would produce the microstructures denoted in the subscripts of the respective lines. The diffusion-controlled processes start upon crossing any of the solid black lines, which are all shifted to the right due to the Ni in steel B.

The cooling line C_M shows an example of cooling that would produce martensite. The transformation of austenite to martensite starts at M_S. At M_{50} and M_{90}, 50 and 90 percent, respectively, of the austenite will have transformed to martensite. Comparing the C_M lines for steels A and B shows that a much higher cooling rate is necessary for A than for B to produce martensite. Attempting to do so for steel A would require a quenching time of only a few seconds, which would be highly impractical. The cooling happens at the surface of the specimen, and as such, the appropriate temperature may not be met quickly enough throughout the thickness of the specimen, resulting in residual austenite, increasingly so with increasing depth, which severely impacts the mechanical properties. Looking at C_m for steel B, the cooling time is approximately an order of magnitude longer, thereby allowing for more time to form martensite throughout the thickness of a specimen. It should also be noted that M_s, M_{50} and M_{90} are lower for steel B, which means that the final temperature met during the quenching also should be lowered. The martensite transformation is not a diffusion-controlled process, and is not delayed by the addition of Ni.

The cooling line C_{F+P} shows an example of a cooling procedure that would produce a mixed ferrite-pearlite microstructure. Upon entering the A+F area, ferrite will start to form along the prior austenite grain boundaries. At the dotted line, 50% of the austenite will have transformed to pearlite, and upon reaching the solid line at the boundary of the F+C area, 100% of the austenite will have transformed to pearlite. Once all the austenite has transformed, nothing more will happen upon further cooling. The main difference between C_{F+P} for steels A and B is the rate of cooling, and followingly, the time spent in the A+F and A+F+C regions, due to the reduction in the carbon diffusion rate. In the A+F region, where ferrite forms, a lower carbon diffusion rate causes the ferrite grains to be finer. In the A+F+C region, where pearlite forms, a lower carbon diffusion rate reduces the

distance the carbon travels, resulting in finer and thinner lamellae. The refinement of the ferrite grains gives a higher yield strength, whereas the refinement of the pearlite gives a higher tensile strength, while at the same time decreasing the ductility. [3]

Fracture toughness

Because of the increased hardenability, the fracture toughness will increase. The ductile-to-brittle-transition-temperature (DBTT) will reduce because of the grain refinement following the increase in hardenability, and by Ni being in solid solution in the ferrite phase. This has been shown by conducting tests with steel and pure iron (ferrite), which were both seen to have a lower DBTT with the addition of Ni. Manganese (Mn) also increases the hardenability and DBTT of steels, but not in pure iron, which would suggest that the increase in DBTT for this case is exclusively due to the increase in hardenability.

Segregation of metalloid elements

Ni and Cr, especially when present together, promote the segregation of metalloid elements, such as antimony, phosphorus, tin and arsenic, to prior austenite grain boundaries at temperatures between 350 and 600 °C. This is believed to be the cause of temper embrittlement, which is a decrease in fracture toughness, characterized by a decrease in DBTT [2]. Segregation of metalloid elements may be prevented by imposing restrictions on impurity levels during production, and may be reversed by tempering in the 350 to 600 °C range, which dissolves and distributes the elements back into the grains.

2.2 Hydrogen Embrittlement

This chapter deals with Hydrogen Embrittlement. In the first section, some background information and terminology is provided. The subsequent sections are about hydrogen sources, how hydrogen enters a material, how hydrogen affects the material once inside, testing for hydrogen embrittlement, and fractographic features of hydrogen embrittlement.

2.2.1 Hydrogen Embrittlement Terminology and Definitions

Hydrogen embrittlement, a form of Environmentally Assisted Cracking (EAC), is a collective term for several types of deterioration that can occur when atomic hydrogen enters a metal. *Figure 15* shows a hierarchy of EAC terminology. [7] [8]

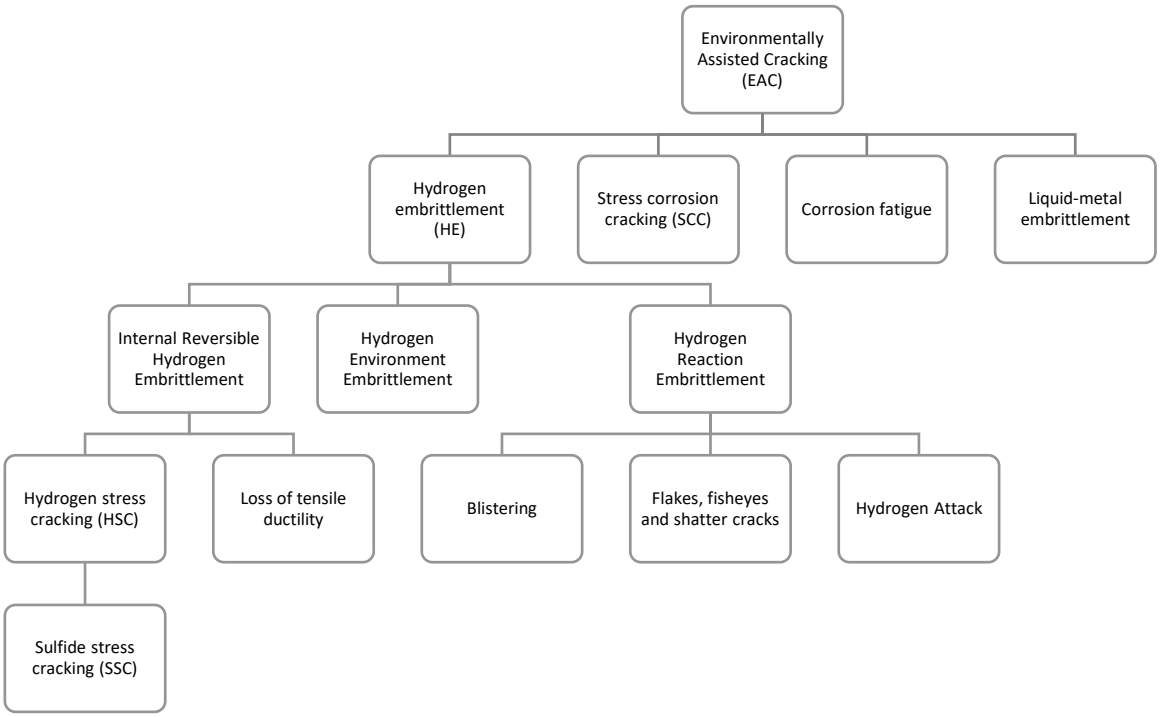

Figure 15 Hierarchy of EAC terminology. Compiled using information from ref. [7] and [8]

Hydrogen embrittlement (HE) is divided into three different types: Internal reversible hydrogen embrittlement (IRHE), Hydrogen environment embrittlement (HEE) and Hydrogen reaction embrittlement (HRE). All three are characterized by different chemical and physical reactions, as shown in *Table 1*.

Table 1 The necessary physical and chemical reactions for different types of HE. Table from ref. [9]

STEPS NECESSARY FOR EMBRITTLEMENT		OCCURRENCE OF EMBRITTLEMENT STEPS — TYPES OF EMBRITTLEMENT: HYDROGEN ENVIRONMENT	INTERNAL REVERSIBLE	HYDROGEN REACTION
1→2 MOLECULAR PHYSISORPTION	ADSORPTION	YES	NO	YES/NO
2→3 DISSOCIATION	ADSORPTION	YES	NO	YES/NO
3→4 CHEMISORPTION	ADSORPTION	YES	NO	YES/NO
4→5 SOLUTION (ABSORPTION)		YES	YES	YES
5→6 LATTICE DIFFUSION		?	YES	YES/NO
5/6→7 HYDROGEN REACTION TO FORM HYDRIDES AND/OR GAS BUBBLES		NO	NO	YES

Internal Reversible Hydrogen Embrittlement (IRHE) is a form of HE, with mechanical effects ranging from loss of tensile ductility to cracking. For it to be fully reversible, the embrittlement must occur without the hydrogen undergoing any type of chemical reaction or causing microscopic cracks [7]. There are two forms of IRHE: Hydrogen stress cracking (HSC) and loss of tensile ductility.

Hydrogen stress cracking (HSC) is commonly associated with high strength steels, and is when a susceptible material fractures at a lower stress than usual, due to a combination of atomic hydrogen and stresses. The stresses can be external stresses that the material is subjected to during its lifetime, as well as internal residual stresses due to manufacturing [10]. The external stresses are usually static or slowly-changing loads that are sustained over a longer period [5]. Sulphide stress cracking (SSC) is a form of HSC, and is, similarly, when a susceptible material fractures at a stress that is lower than usual, due to a combination of atomic hydrogen and stresses, but with the distinction that the hydrogen comes from attacks of H_2S-corrosion on the metal's surface. This distinction is important, because the presence of sulphides promotes the entry of hydrogen into the metal [10]. HSC and SSC are usually associated with failures in industrial applications, where the material has been used at a stress that is below its yield strength.

Loss of tensile ductility is commonly associated with low strength steels, and is used for when a metal fails at a lower elongation than it otherwise would have, without the stress necessarily being any lower. The specimen's cross sectional area will undergo less reduction than it did in the absence of hydrogen [5]. This form of HE is commonly associated with experimental work, such as tensile tests, where the material is stressed beyond its yield strength. The failure will occur in the plastic region of the curve.

Hydrogen environment embrittlement (HEE) is usually used when referring to the damage that can occur due to high pressure hydrogen gas, such as is found in a hydrogen storage tank. The hydrogen gas dissociates to atomic hydrogen, and enters the metal. The mechanism is not yet fully understood, and there is disagreement on whether it is a form of internal reversible hydrogen embrittlement, or if it is a distinct form of hydrogen embrittlement [11]. One of the main arguments for there being different mechanisms behind HEE and IRHE, is that high strength nickel alloys, such as Inconel 718, are generally susceptible to HEE, while generally unsusceptible to IRHE. This is believed to be related to some undefined surface characteristic of nickel alloys. Other materials, such as steels, exhibit similar susceptibilities to both HEE and IRHE. [9]

Hydrogen reaction embrittlement (HRE) is an irreversible form of HE, and refers to the damage that can occur from hydrogen reactions. Once hydrogen is adsorbed, it can react near the surface or diffuse into the metal before reacting.

Hydrogen-induced blistering, also referred to as Hydrogen induced cracking (HIC), is most commonly found in low-strength alloys that have been exposed to aggressive environments and cleaning processes, such as an H_2S-containg environment and cleaning by acid pickling. Atomic hydrogen is absorbed into a metal, and then recombines as molecular hydrogen at internal voids, laminations, or inclusion/matrix interfaces. This can build up pressure great enough to produce internal cracks, and if they occur close to the surface, the hydrogen can push out a portion of the metal, creating a visible bulge that resembles a blister. This can occur in the absence of stress. [8] [7]

Shatter cracks, flakes, and fisheyes are features of hydrogen damage in forgings, weldments, and castings. They are attributed to hydrogen pickup during melting operations when the melt has a higher solubility for hydrogen than the solid alloy. During cooling from the melt, hydrogen diffuses to and precipitates in voids and discontinuities, creating the same effects as blistering. [8]

Hydrogen attack happens at high temperatures (usually over $200℃$) and high pressures when a carbon- or low-alloy steel is exposed to hydrogen for an extended time. Hydrogen enters and reacts with carbon in solution or carbide form, creating methane gas. This can form cracks and fissures, or can decarburize the steel, resulting in reduced strength. [8]

Stress corrosion cracking (SCC), which is a different form of EAC, is when a material cracks due to a synergistic effect of mechanical stress and corrosion. If the corrosion is caused by the metal reacting with hydrogen, though, HE and SCC could potentially be happening at the same time. A common distinction between the two is based on what the effects would be if the potential were changed: if increasing the potential accelerates crack growth, then it is SCC. Similarly, if decreasing the potential increases crack growth, then it is HE. [8]

2.2.2 Hydrogen Sources

Cathodic Protection

Cathodic protection is used to protect a metal from corrosion. To understand how cathodic protection works, it is necessary to first have a look at how corrosion works.

Corrosion of an arbitrary metal M can be described by the oxidation reaction, *Equation 14*:

$$M \rightarrow M^{n+} + ne^{-} \qquad 14.$$

For the oxidation reaction above to occur, there must be a reduction reaction as well. In aqueous environments, the two most common reduction reactions are hydrogen evolution, as seen in *Equation 15*, and reduction of dissolved oxygen, as seen in *Equation 16*.

$$2H^{+} + 2e^{-} = H_2(g) \qquad 15.$$

$$\frac{1}{2}O_2(dissolved) + H_2O + 2e^{-} = 2OH^{-} \qquad 16.$$

The potentials and currents for the reactions above can be plotted in an Evans diagram, as shown in *Figure 16*.

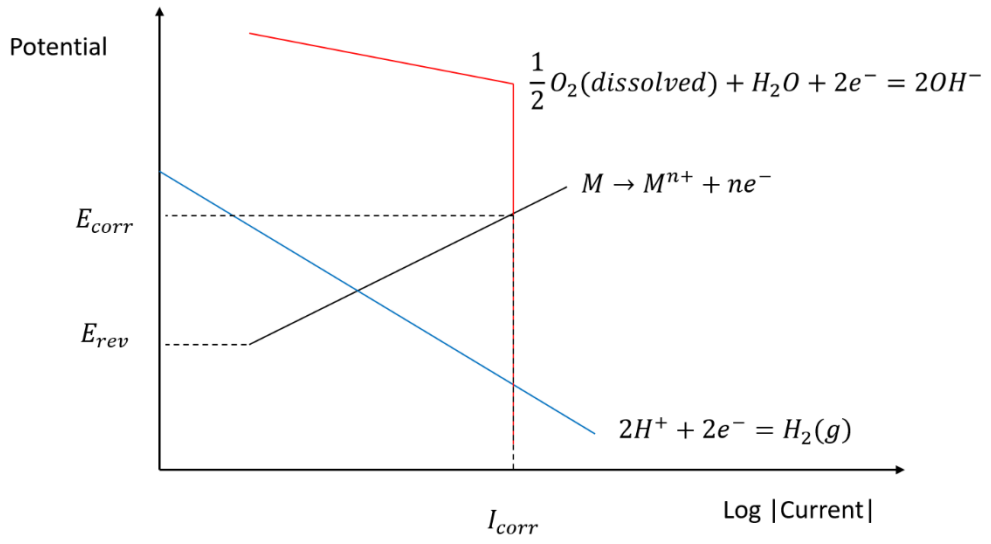

Figure 16 Evans diagram

In *Figure* 16, the metal M is corroding freely at a potential E_{corr} and current I_{corr} due to a combination of hydrogen evolution and oxygen reduction. Since the scale is logarithmic, the current of the oxygen reduction is several orders of magnitude greater than the hydrogen evolution.

To prevent the metal M from corroding, an external current can be impressed to shift the potential down to a point that is below E_{rev}. This is illustrated in *Figure 17*.

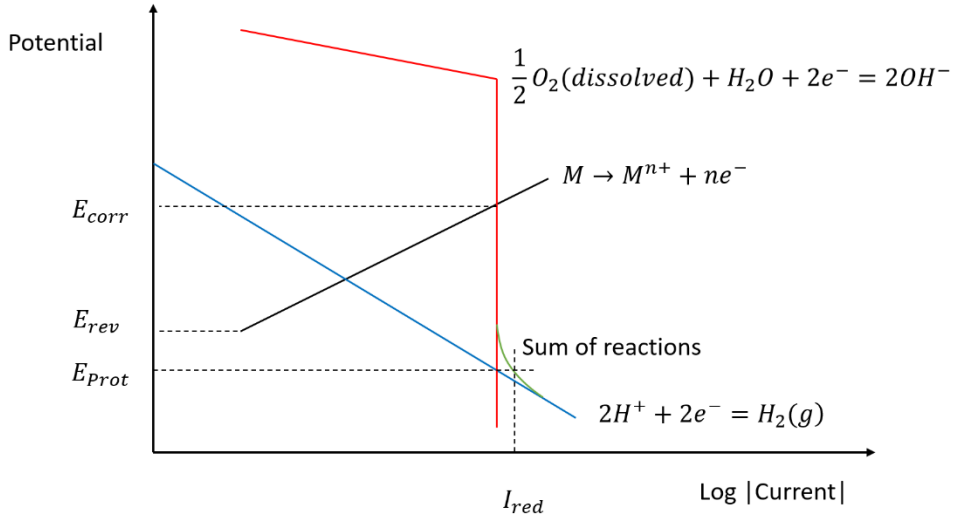

Figure 17 Evans diagram showing the effects of an impressed current

The potential in the case shown in *Figure 17* is so low that metal M will be immune to oxidation. The oxygen reduction and hydrogen evolution reactions are however still happening, but with the external current as their driving force instead of the oxidation of metal M. The potential at which the reactions find place now corresponds to I_{red}, which is higher than the current I_{corr} in *Figure 16*. This means that the reduction reactions are happening at a faster rate. At this potential, the current for the hydrogen evolution reaction has increased to a current that is the same as the oxygen reduction reaction. Lowering the potential even further will cause the hydrogen evolution reaction to happen at a faster rate. [12]

The consequences of this are that although the metal is protected from corrosion, there will be atomic hydrogen present.

Hydrogen Sulphide (H_2S)

In sour service oil and gas environments, hydrogen sulphide (H_2S) is present in the formation, and can act as a hydrogen source. When in contact with water, H_2S dissolves into H^+ and HS^-, which decreases the pH and can cause pitting and crevice corrosion. The main concern, however, is that H_2S is a recombination poison, which means that it suppresses the recombination of hydrogen to hydrogen gas, thereby promoting the entry of hydrogen into the metal. [13] [7]

Manufacturing Processes

Manufacturing processes such as welding, electroplating, pickling and phosphating can cause trapping of hydrogen in the metal. This is usually prevented by adhering to the regulations that are set for the processes, but there have been cases of hydrogen embrittlement failures caused by manufacturing processes alone. [7]

2.2.3 Hydrogen Entry, Diffusion and Trapping

Hydrogen Entry

The total reaction for the reduction of atomic hydrogen into hydrogen gas at the surface of a metal is given in *Equation 17*. [12]

$$2H^+ + 2e^- = H_2(g) \quad 17.$$

The reaction in *Equation 17* happens in two steps. First, a hydrogen atom is adsorbed at the metal M's surface by a charge transfer reaction, as seen in *Equation 18.* The adsorbed hydrogen atom can then react with another adsorbed hydrogen atom, as in *Equation 19,* or it can react with a proton and an electron, as in *Equation 20*. Both reactions result in the adsorbed hydrogen atom leaving the metal as hydrogen gas. The designation $MH_{(ads)}$ is used to refer to a hydrogen atom that is adsorbed at the metal M's surface.

$$H^+ + e^- + M \rightarrow MH_{(ads)} \quad 18.$$

$$MH_{(ads)} + MH_{(ads)} \rightarrow M + H_2(g) \quad 19.$$

$$H^+ + e^- + MH_{(ads)} \rightarrow M + H_2(g) \quad 20.$$

However, a small amount of the adsorbed hydrogen atoms will, instead of reacting with other adsorbed hydrogen atoms, be absorbed by the metal M, as in *Equation 21*, where $MH_{(abs)}$ signifies a hydrogen atom absorbed by metal M. [14]

$$MH_{(ads)} \rightleftarrows MH_{(abs)} \quad 21.$$

The absorption reaction of hydrogen is in equilibrium, and the rate at which it finds place is controlled by diffusion.

Hydrogen Diffusion

Diffusion is the process by which matter is transported from one part of a system to another because of random atomic motions [3]. The rate of mass transfer is known as the diffusion flux (J), and can be calculated using *Equation 22*, Fick's first law. This is valid in the case of steady state diffusion in one direction (x).

$$J = -D\frac{dC}{dx} \tag{22.}$$

Where J is the diffusion flux in kg/m^2s or $atoms/m^2s$, $\frac{dC}{dx}$ is the concentration gradient and D is the diffusion coefficient, expressed in m^2/s. The diffusion coefficient is a constant that is determined by factors such as temperature, diffusing species, material composition, environment, and stress. In Fick's first law, the only driving force behind the diffusion is the concentration gradient, and time is not considered.

The case of steady-state diffusion in Fick's first law is an idealized scenario; most practical diffusion situations will be time-dependent (non-steady-state). Non-steady-state diffusion is described by Fick's second law, *Equation 23*.

$$\frac{\delta C}{\delta t} = \frac{\delta}{x}\left(D\frac{\delta C}{\delta x}\right) \tag{23.}$$

Fick's second law is usually made solvable by setting appropriate boundary conditions. In the literature, there are comprehensive collections of solutions to Fick's second law that apply for specific cases. One of these collections is by Crank, who presented *Equation 24*, which is applicable for diffusion into a thin sheet. The conditions set are that the diffusing species must have a uniform initial concentration C_0 and a constant surface concentration C_S [15].

$$\frac{C - C_0}{C_S - C_0} = 1 - \frac{4}{\pi}\sum_{n=0}^{\infty}\frac{(-1)^n}{2n+1}\exp\left\{-\frac{D(2n+1)^2\pi^2 t}{4l^2}\right\}\cos\frac{(2n+1)\pi x}{2l} \tag{24.}$$

Where l is the thickness, D is the diffusion coefficient and C is the concentration at distance x into the sheet at time t. The equation assumes that the sheet is so thin that the diffusion through the edges is negligible [15].

Equation 24 may be used in the case of hydrogen diffusion in a thin sheet, given that the concentration of hydrogen at the surface is known to be constant, and that the initial concentration of hydrogen throughout the specimen is uniform. Furthermore, as a simplification, the equation may also be used to approximate hydrogen diffusion into a cylindrical specimen. Here the hydrogen diffusion is assumed to take place from all around the cylinder, and thus, the cylinder's radius is inserted as the thickness l. *Figure 18* illustrates hydrogen diffusion in (a) a thin sheet and (b) a cylinder.

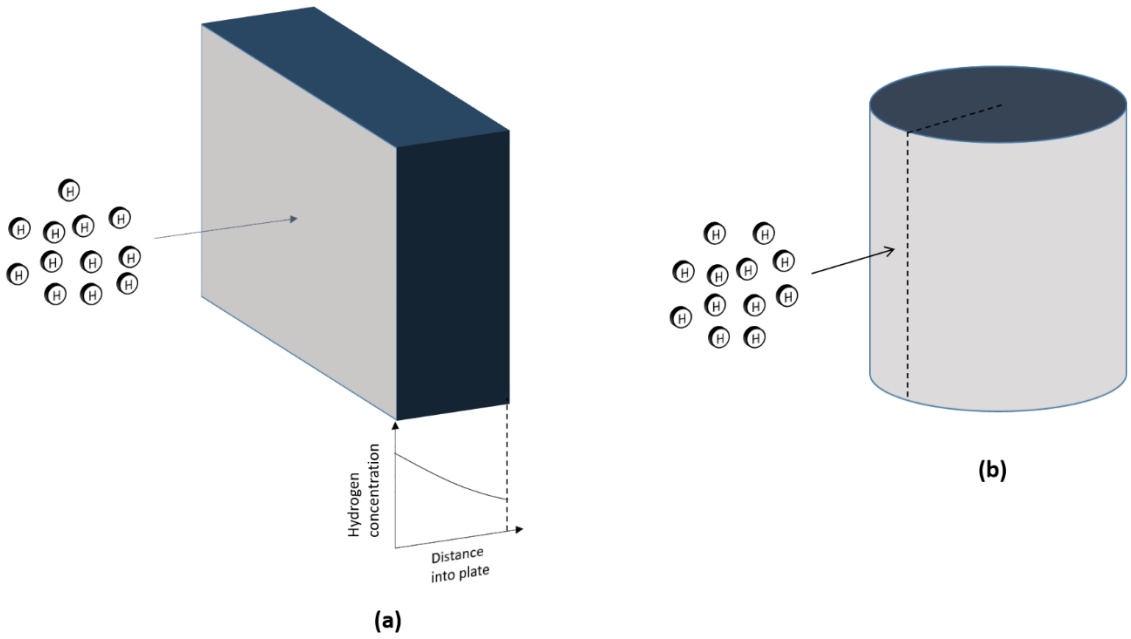

Figure 18 (a) Diffusion of hydrogen in a thin plate, with hydrogen concentration profile. (b) Diffusion of hydrogen in a cylinder.

Hydrogen Trapping

While hydrogen atoms are diffusing into a metal, they will be drawn to and held in place in sites called traps. Traps can be metallurgical defects such as vacancies, dislocations, interstitials, substitutional atoms, internal surfaces, grain boundaries and precipitates or inclusions. The trapping mechanisms are divided in two groups:

- Attractive traps draw the hydrogen atoms in by electronic forces, stress fields or temperature gradients, without modifying the lattice structure.
- Physical traps are physical discontinuities in the lattice structure, such as grain boundaries and voids, where a hydrogen atom may enter due to the favourable energy situation. These may be mobile (dislocations, stacking faults) or stationary (grain boundaries, carbide particles, individual solute atoms). [8]

The division of attractive and physical trapping is a simplification, and most traps will be combinations of the two types. Depending on how much time a hydrogen atom spends in the traps, they can be classified as either reversible or irreversible, where the reversible traps are short-duration, and irreversible traps are long duration. Physical traps have higher binding energies than attractive traps, and are more likely to be irreversible. In the literature, there is a lot of uncertainty as to the exact nature of different traps. For instance, a dislocation in itself is generally seen as a reversible trap, but the point defects that accompany dislocations, such as vacancies and interstitial atoms, may or may not be irreversible [8] [16].

In general, traps reduce the diffusivity of steel. In consequence, the likelihood of forming and developing hydrogen collectors increases, which again increases the tendency of embrittlement [17].

2.2.4 Theories for Hydrogen Damage Mechanisms

The exact mechanisms behind the degradation that occurs once hydrogen has entered a metal are not yet fully understood, and there are a lot of different theories that seek to explain various aspects of hydrogen damage. In this section, some of the most renowned theories are listed and explained, starting with the early models.

The pressure theory is one of the very first models. The model attributes hydrogen embrittlement to the diffusion of atomic hydrogen into the metal, where it accumulates in voids and recombines to form hydrogen gas, creating high internal pressure that initiates cracking. This model is reasonable enough when it comes to blistering and hydrogen induced cracking (HIC), which happen in the absence of stress, but falls short in explaining the synergistic effects of hydrogen and stress that are observed in for instance HSC. [8]

The surface adsorption theory is another early model, and it suggests that hydrogen adsorbs on the free surface of a growing crack, as illustrated in *Figure 19*. This decreases the surface free energy and enhances crack propagation. This model has been criticized for greatly underestimating the work required for fracture, and does not explain the discontinuous crack growth that has been observed in hydrogen cracking. [8]

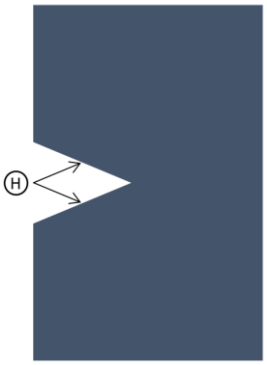

Figure 19 Hydrogen adsorption on the surface of a growing crack

Hydrogen-Enhanced Decohesion (HEDE) infers, based on quantum-mechanical calculations, that hydrogen weakens intermetallic bonds between the atoms in a metal matrix. This may cause the atoms in regions of higher hydrogen contents and stresses, such as in a crack tip, grain boundary or near an inclusion, to separate rather than slip along its crystal plane, as would be the case in the absence of hydrogen [8] [18]. This is illustrated in *Figure 20*.

Due to the nature and scale of the events thought to take place during HEDE, it is hard to obtain direct experimental evidence of the mechanism. As an indirect form of evidence, however, slip planes by the crack tips in steels embrittled by hydrogen have been observed to be oriented in ways that would rule out slipping [18].

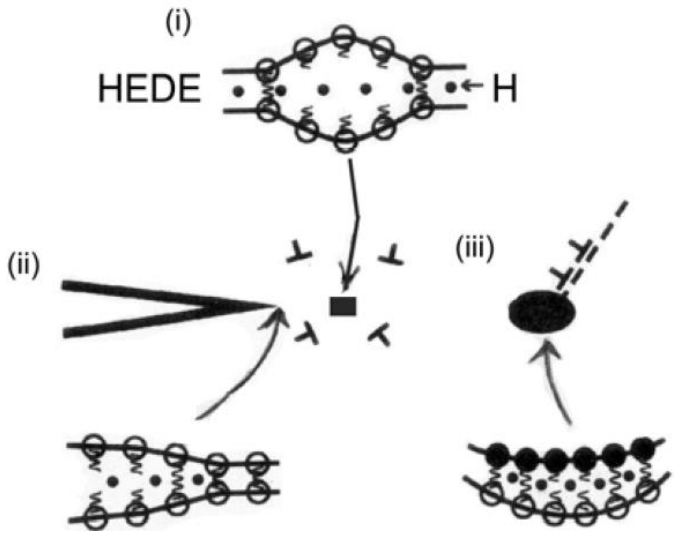

Figure 20 Schematic diagrams illustrating the HEDE mechanism by (i) hydrogen in the lattice, (ii) adsorbed hydrogen, and (iii) hydrogen at particle-matrix interfaces. Figure and description from ref. [18]

Hydrogen-Enhanced Localized Plasticity (HELP) proposes, based on elasticity theory and atomistic calculations, that atomic hydrogen enhances and creates dislocations (generally screw dislocations) at surfaces and/or crack tips, causing local softening of the material [8] [18]. A schematic representation of this mechanism can be seen in *Figure 21*.

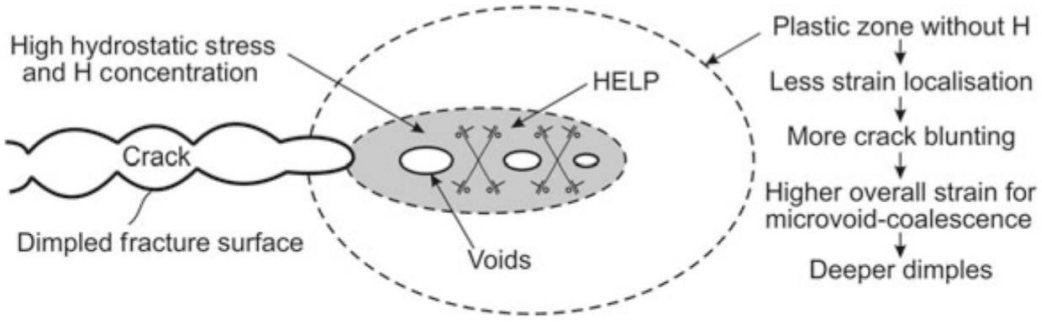

Figure 21 Schematic representation of HELP mechanism. From ref. [18]

Figure 21 shows a propagating crack with an area of a higher hydrogen concentration in front of the tip, where it gathers due to both higher hydrostatic stress and ease of entry at this point, and increases the mobility of dislocations, creating more strain localization, less crack blunting, lower overall strain for microvoid-coalescence and shallower dimples than the case would have been in the absence of hydrogen, as implied by the highlighted fracture characteristics of the "Plastic zone without H" on the figure. Strain localization is when increased plasticity of an area produces a higher deformation at the given point. Crack blunting is when a crack's propagation is resisted due to dislocation immobility or other barriers. Microvoid-coalescence is when small voids grow together into a larger body [3]. [18]

The original circumstance that lead to the development of the theory, was the observation of smaller and shallower dimples on the fracture surface of a hydrogen embrittled specimen, which would suggest increased mobility. By use of in-situ transmission electron microscopy (TEM), direct observations of thin foils as hydrogen was introduced showed the onset of movement of dislocations that were formerly stationary, as well as increased velocity in the already-moving dislocations. [18]

Lower yield strengths have sometimes been reported during tensile tests of hydrogen charged specimens, but hardening has also been found to occur. There are many variables, such as material composition, impurity levels, temperature, and strain rate, that may play a part, and it is hard to isolate a single factor as the sole cause. [18]

Adsorption-Induced Dislocation Emission (AIDE) has its background in the discovery of similarities between the fractographic features of hydrogen embrittlement and liquid-metal embrittlement failures, which was taken to signify similarities between the mechanisms as well.

In the AIDE model, hydrogen is adsorbed at the tip of a crack, where it weakens the interatomic bonds, which, along with the stress from the cracking in progress, is believed to cause severing and reformation, as it were, of interatomic bonds in the metal's lattice, as illustrated in *Figure 22*. The lattice slip creates an emission of dislocations that facilitate cracking. Additionally, the initial crack produces a plastic zone of higher stress, with dislocations and voids, which, when met by the dislocation emissions, promote further cracking. [18]

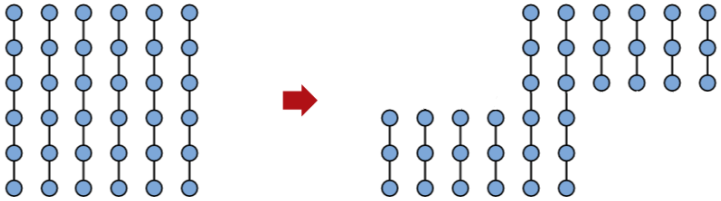

Figure 22 Lattice slip. Figure edited, original from ref. [3]

One of the strengths of the AIDE model, is that the cracking mechanism explains the high crack propagation velocities that are observed in hydrogen embrittlement. This is difficult to account for using the HEDE and HELP models, as both of them rely on the transport of hydrogen. [18]

2.2.5 Testing for Hydrogen Embrittlement

In this section, some of the common test methods used to evaluate HE susceptibility are presented. The NACE TM 0177 test methods are used to qualify materials that deviate from the restrictions set in ISO 15156 for use in sour service environments. Yet, if one were to use these methods to qualify for instance AISI 4340 (which has 1.65 to 2 wt% Ni), the qualification would only hold for the given supplier of the steel, with the specific manufacturing route. Extensive quality control processes would also be required. As such, the industry seldom does this type of qualification for specific alloys.

Slow strain rate testing (SSRT) is another test method, that is mainly used to screen for differences in HE susceptibility with varying metallurgical factors. Unlike the NACE TM 0177 methods, SSRT results cannot be used to qualify specific alloys for use in sour service environments. Still, though, the method is more suited than the NACE TM 0177 methods when it comes to challenging general guidelines (such as the 1 wt% Ni limit), because it is highly sensitive, and can show differences that the other methods do not. As such, a collection of SSRT results that show that there is no correlation between Ni content and HE susceptibility could aid the removal of the Ni restriction in ISO 15156 altogether.

NACE TM 0177 Test Methods

These methods are meant to represent behaviour in sour service environments. For all methods, the test specimen is submersed in a specified solution with specified amounts of gas (such as H_2S and CO_2) that is deemed appropriate for the test. [19]

Method A – NACE Standard Tensile Test – A smooth sample of standardized dimensions is tested by uniaxial tension under a sustained load that is within 10% of the material's yield strength. The test duration is 720 hours, and the material fails the test if it separates or has any visible cracks at a 10X magnification.

Method B – NACE Standard Bent Beam Test – A straight standardized test specimen is placed horizontally, supported between a point at each end, and is deflected by applying a bending stress at the middle, creating a stress concentration at this point. The test duration is 720 hours, and failure is when a material cracks. Multiple samples are tested at various deflections, and the results are used to find a critical stress level at which failure is 50% likely.

Method C – NACE Standard C-Ring Test – A standardized test specimen, shaped as a C, is tested under hoop stress. A hole is drilled through the top and bottom of the C-shape, a bolt that goes through both holes is inserted, and nuts are fastened at both ends. The stress is applied by fastening the nutes, bringing the semi-circle together. The test duration is 720 hours, and failure is when cracks are initiated. The highest stress at which no cracking occurs is reported.

Method D – NACE Standard Double-Cantilever-Beam (DCB) Test – A specimen with two cantilevers is loaded by inserting the narrow end of a double-tapered wedge. The results are used to find a critical stress intensity threshold, expressed as K_{ISSC}.

Slow Strain Rate Testing (SSRT)

In a slow strain rate test, a specimen of standardized dimensions is pulled to failure at a constant strain rate, typically within the range of $1 * 10^{-7}s^{-1}$ to $1 * 10^{-5}s^{-1}$. The machine has a built-in vessel that goes around the specimen during testing, which can be used to simulate a wide range of service environments, thereby making the method suitable for screening for different kinds of EAC. The results of SSRT are meant to be used comparatively to look for trends, rather than giving exact representations of behaviour under normal working conditions. *Figure 23* shows a typical SSR machine and a standard test specimen with a table of specified dimensions [20].

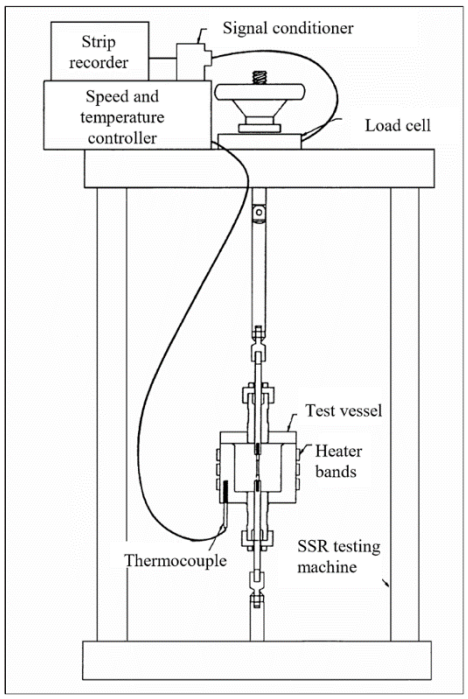

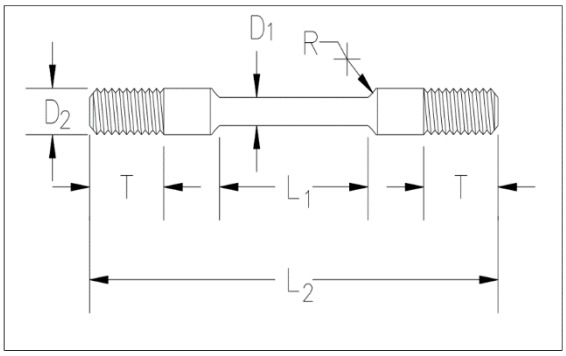

	mm
L_1	25.4
L_2	Not specified
D_1	3.81 $\pm$0.05
D_2	6.35 $\pm$0.05
R	6.35 min.
T	Not specified
Thread	Not specified

Figure 23 A typical SSR machine and standard test specimen. Figures and table from ref. [20]

After SSRT in a specific environment has been performed, there are two basic ways to analyse the results in search of EAC:

1. The fractured specimen should be examined visually to look for cracks and abnormalities in the gauge area. This is commonly done using scanning electron microscopy. Additionally, a macroscopic view of the specimen is often used to look at the three-dimensional geometry.
2. The numerical results should be used to calculate ductility parameters, which are to be compared with the baseline performance in air.

The following equations and ratios are used to calculate the ductility parameters:

RA (reduction in area) for a specimen with a circular cross sectional area, *Equation 25*.

$$RA(\%) = \frac{D_I^2 - D_F^2}{D_F^2} * 100 \qquad 25.$$

Where D_I and D_F are the diameters before and after SSRT, respectively. D_F is the diameter measured at the point of fracture

Reduction in area ratio (RAR), *Equation 26*.

$$RAR(\%) = \frac{RA_E}{RA_A} * 100 \qquad 26.$$

Where RA_E and RA_A are the reductions in area measured in the test environment and in air, respectively.

Plastic elongation, *Equation 27*.

$$E_{plastic}(\%) = \left(\varepsilon_{fracture} - \varepsilon_{yield}\right) * 100 \quad 27.$$

Where $\varepsilon_{fracture}$ and ε_{yield} are the strains measured at the yield point and at the point of fracture, respectively.

Plastic elongation ratio, *Equation 28*.

$$E_{plastic}R(\%) = \frac{E_{p_E}}{E_{p_A}} * 100 \quad 28.$$

Where E_{p_E} and E_{p_A} are the plastic elongations in the test environments and in air, respectively.

Ratios of up to 100 indicate high resistance to EAC, whereas low ratios indicate low resistance to EAC. [20, 21]

2.2.6 Fractography

Fractures of low strength steels in hydrogen environments are usually characterized by ductile dimple rupture, tearing, cleavage, quasi-cleavage, and, in some special cases, intergranular cracking. Fractures in high strength steels are usually either by intergranular cracking or quasi-cleavage. [13]

Figure 24 shows a collection of images of the mentioned fracture characteristics. (a) is dimple rupture. This is a ductile feature, usually observed in tests in air. The sizes and depths of the dimples are indicative of the ductility; areas of larger and deeper dimples are more ductile. The dimples seen in hydrogen environments will usually be smaller and shallower than those observed in air (b) is a picture of quasi-cleavage and tearing. This looks like a combination of dimples and cleavage, and may be observed in areas between ductile and brittle features. (c) shows flat cleavage planes, which are seen in brittle fractures. (d) shows cleavage that has gone straight through the grains and grain boundaries, while (e) shows cleavage that has gone along them.

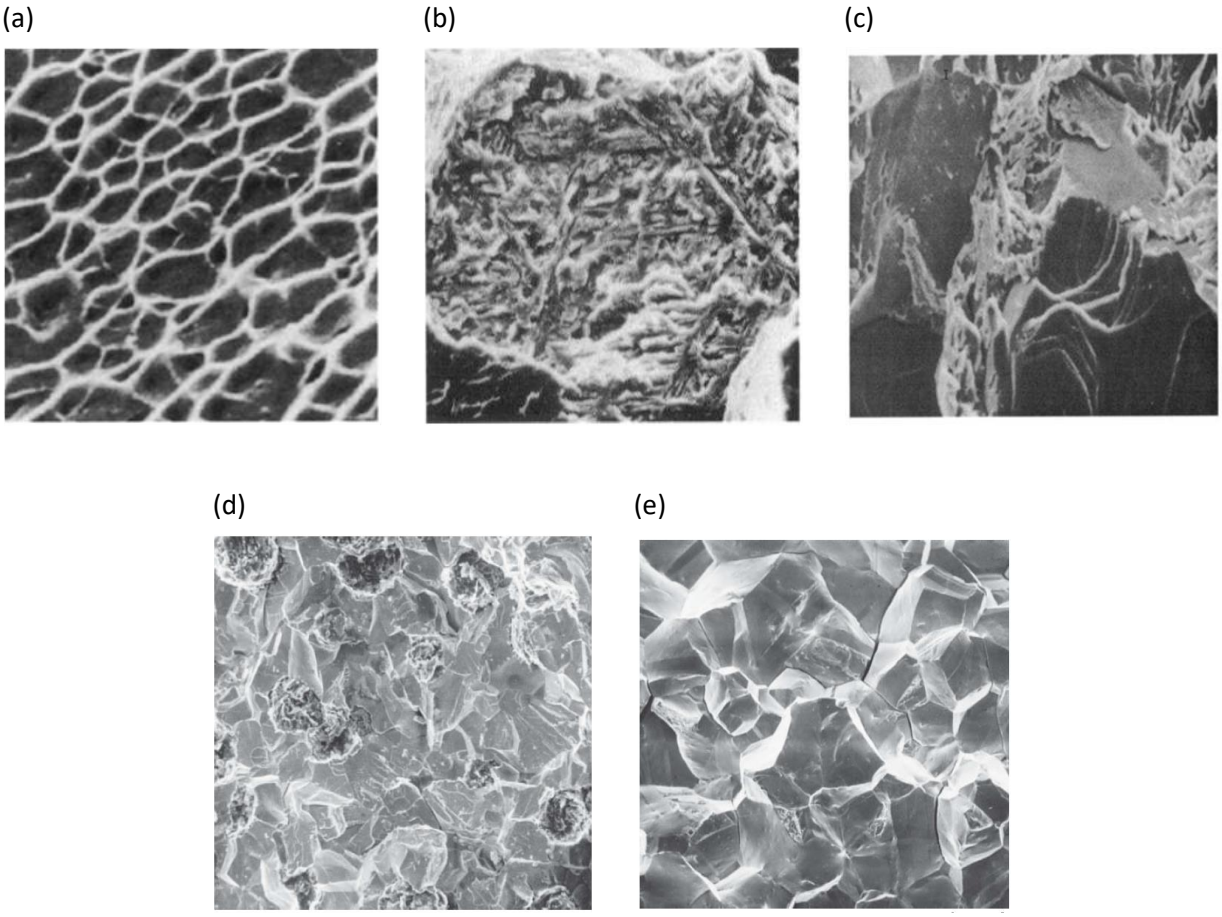

Figure 24 (a) dimple rupture (b) quasi-cleavage and tearing (c) cleavage (d) transgranular cleavage (e) intergranular cleavage. Pictures from ref. [22] and [3]

2.3 Literature Survey

2.3.1 Effect of Nickel on Sulphide Stress Cracking of Low Alloy Steels

In this section, a history of the role of Ni on SSC of LAS is given. This literature survey is based on reviews of the subject that were published by Craig (1988) [23], Jarvis (1992) [24] and Kappes (2014) [2].

The Ni restriction in ISO 15156:2 [1] is based on research by Treseder and Swanson (1968) [25], and Dunlop (1978) [26], that was performed using the NACE Standard Bent Beam Method [19] [2]. Treseder and Swanson [25] reported that quenched and tempered steels with more than 1 wt% Ni all failed to meet the stress intensity limit $S_C > 10$, even though the hardness of the materials were below the acceptable level set by NACE [25]. This is shown in *Figure 25*.

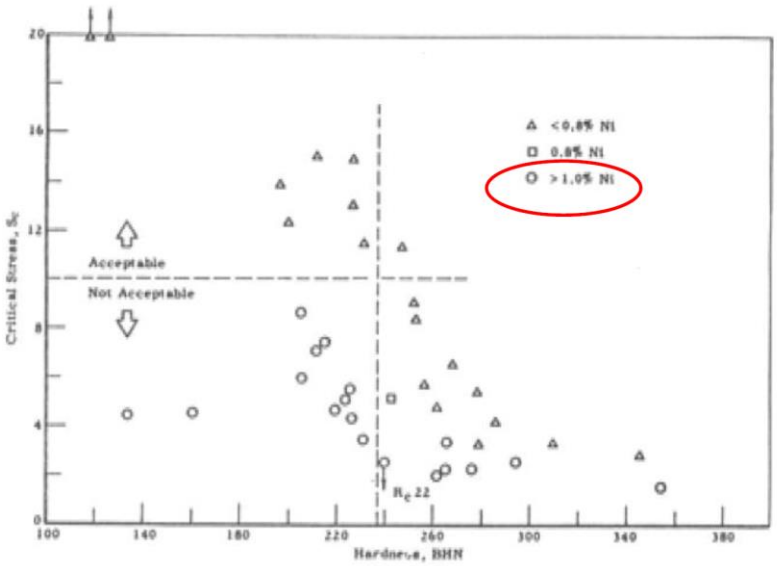

Figure 25 On the X-axis, the Brinell hardness is shown. A Brinell hardness of 235 is roughly equivalent to 22 HRC. On the Y-axis, the critical stress S_C is shown. The triangles, squares and circles represent Ni-contents of below 0.8, 0.8 and above 1.0 wt%, respectively. Figure from ref. [25]

Treseder and Swanson [25] took these findings to mean that all steels with Ni contents above 1.0 wt% were unfit for sour service use. This has been widely criticised by other researchers, and it has been pointed out that the tempering temperatures used did not account for the effects of Ni on the austenite transformation temperature [2]. As an example, AISI 4340 was tempered at 718°C; using *Equation 12* along with the specifications of the lowest possible amounts of alloying elements for AISI 4340, the AC_1 temperature is estimated to be 701°C. Additionally, the quenched and tempered Ni-containing steels were considerably stronger than the Ni-free counterparts they were compared to, which is also believed to have affected the results [23]. Steels that have yield strengths higher than 930 MPa have been shown to crack in H_2S environments regardless of their compositions [2]

Kobayashi et al. [27] tested quenched and tempered high strength steels with chemical compositions as given in *Table 2*. Using constant load tests, bent beam tests and wedge-opening load tests in combination with cathodic hydrogen charging done in 700 hours in tap water with a charging density of 16 A/m^2, no differences were found in fracture toughness nor critical stress threshold K_{ISCC} between the samples with 0 and 2 wt% Ni.

Table 2 Chemical compositions and mechanical properties. Picture from ref. [27]

TABLE 1 Chemical Compositions (wt. %)

	C	Si	Mn	P	S	Ni	Cr	Mo	Cu	B
4340	0.36	0.30	0.77	0.017	0.020	1.85	0.73	0.18	0.14	
10B35	0.38	0.24	0.99	0.019	0.026	0.02	0.09		0.01	0.0012

TABLE 2 Mechanical Properties

Material	Tempering temperature (K)	0.2 % proof stress (MPa)	Tensile strength (MPa)	Elongation (%)	Reduction of area (%)
4340	373	1569	2118	11.0	
	473	1579	1932	10.2	40.5
	573	1412	1667	10.2	49.9
	673	1373	1510	9.0	
	773	1177	1236	12.0	
	873	1049	1118	18.2	54.3
10B35	473	1589	1912	12.1	46.1
	673	1147	1236	12.6	59.7
	873	706	804	21.5	66.0

Sieradzki [28] studied the dependence of H_2S partial pressure on the threshold for crack propagation in a high strength (1580 MPa yield strength) quenched and tempered AISI 4340 sample. When the curves were compared with similar tests of AISI 4340 and AISI 4140 (which has 0 wt% Ni), the slopes were found to be similar; not only for H_2S, but also for charging in H_2. This was taken to mean that Sulphur did not play a significant role in SSC, and that the cracking phenomena in H_2S were due to hydrogen embrittlement. The results are shown in *Figure 26*. The findings indicate that high-strength LAS with Ni are no more susceptible to SSC than equivalent steels without Ni [23].

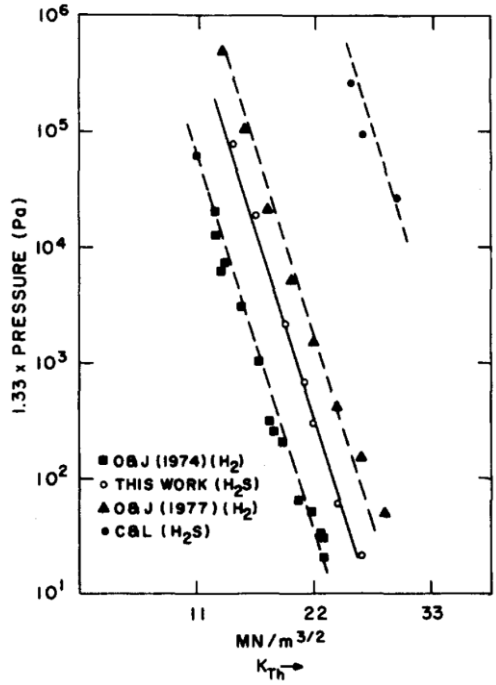

Figure 26 O&J refers to similar studies by Oriani and Josephic, who tested 4340 in H_2 and H_2S (see legend). C&L is an AISI 4140 specimen tested by Clark & Landers [23]. Figure from ref. [28]

Payer et al. conducted a study to evaluate how different heat treatments of steels with Ni-contents ranging from 0 to 3 wt% influenced the susceptibility to SSC. The authors stated that all the materials had adequate SSC resistances after having undergone appropriate heat treatments. An additional tempering step rendered the higher Ni-steels resistant to SSC. This was believed to be due to the tendency of Ni to segregate during solidification, causing an area of a higher concentration of alloying elements, where the AC_1 temperature is lower, which again leads to retained austenite in the area [29]. In these cases, a second tempering step is necessary to transform the entire microstructure into tempered martensite [2].

More recent studies have found conflicting results; most of them finding no correlation between Ni content and SSC [2]. Instead, it is generally accepted that the microstructure gives a better indication of the SSC resistance.

The most recent found during this literature search was conducted in 2016. Hui et al. [30] performed constant load tests (CLT) and SSR tests with cathodic hydrogen charging to examine the HE susceptibilities of quenched and tempered medium-carbon high-strength notched steel specimens with 0, 0.5 and 1.0 wt% Ni. The chemical compositions of the steels are given in *Table 3*. Results of the SSR tests are shown in *Figure 27*, and a summary of all tests and HE susceptibilities are shown in *Table 4*.

Table 3 Chemical compositions in wt%. Table from ref. [30]

Steel	C	Si	Mn	P	S	Cr	Ni	Mo	V	Nb
N1	0.43	0.19	0.52	0.005	0.005	1.05	–	0.35	0.25	0.03
N2	0.42	0.20	0.52	0.005	0.005	1.05	0.55	0.36	0.25	0.03
N3	0.43	0.20	0.51	0.005	0.005	1.06	1.02	0.36	0.25	0.03

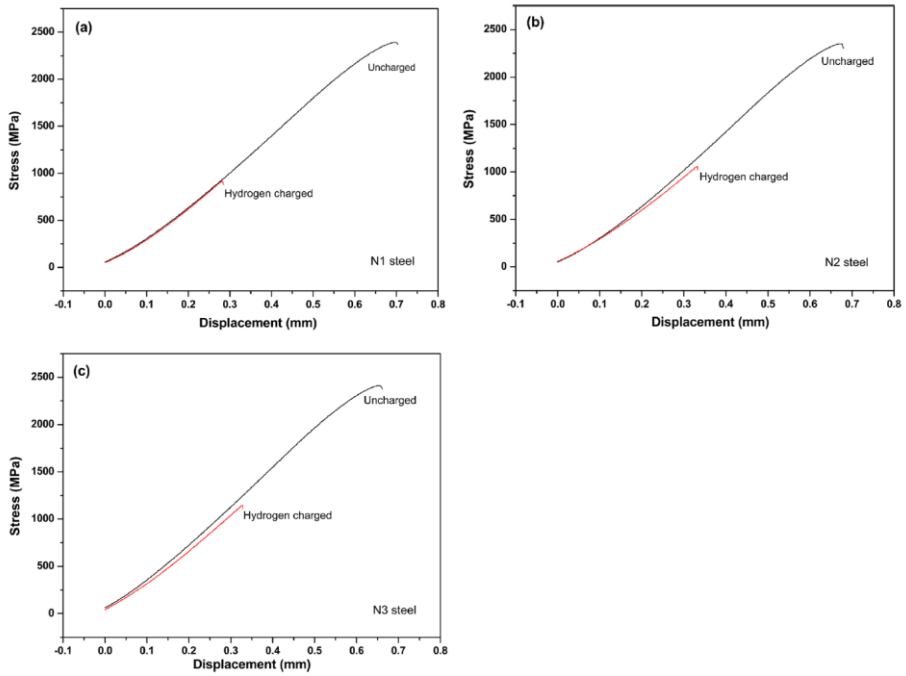

Figure 27 SSR tests. Figure from ref. [30]

Table 4 Summary of SSR and CLT results. From ref. [30]

Sample	Tensile strength R_m (MPa)	Fracture stress in air σ_{NC0} (MPa)	Critical DF stress σ_{NC} (MPa)	HE index HEI_C (%)	HE index HEI_S (%)
N1	1445	2445	1900	22.3	59.3
N2	1445	2417	2050	15.2	52.3
N3	1465	2404	2075	13.7	51.9

In *Table 4*, HEI_C and HEI_S are the HE indexes found from CLT and SSRT, respectively. Both ratios are defined as the losses in notch tensile strengths that were reported during the respective tests. As such, a lower number means a lower susceptibility to HE. The authors concluded that the steels of higher Ni-contents in the tested range were less susceptible to HE. However, the decrease in HE susceptibility appeared to decline somewhat when comparing N1 with N2 and N2 with N3. [30]

2.3.2 Hydrogen Embrittlement of Ferrite-pearlite steels

Ferrite-pearlite steels are considered low strength steels, in that they generally have yield strengths that are below 700 MPa [8]. Followingly, their predominant embrittling character will normally be a loss in tensile ductility during tensile testing, or blistering and HIC under high hydrogen fugacity.

In hydrogen embrittlement studies of ferrite-pearlite steels, the discovery of greater strengths in hydrogen than in air have sometimes been reported. One such study was conducted by Shved et al [31], who studied the effect of carbon content on this behaviour. Samples of pure iron, ST20 (0.2% C), ST45 (0.45% C) and U8 (0.8% C) were vacuum annealed for one hour, and different sets were tensile tested in air and in an H_2SO_4 solution with cathodic hydrogen charging during testing. The gauge lengths were 12 mm, and the crosshead velocity was 1.85 mm/min (strain rate $2.7*10^{-3}$/s). Their findings are summarized in *Table 5.* The yield strengths and tensile strengths in air increased with increasing carbon contents. In hydrogen, the yield strengths also increased, but more so (percent-wise) for the Armco iron and 0.2% C samples than the others. The tensile strength in hydrogen increased in the Armco iron sample, remained the same in the 0.2% C sample, and decreased in the 0.45% C and 0.8% C samples. This was believed to be due to the interaction of hydrogen with dislocations. In pure iron, the hydrogen was thought to pin mobile dislocations, creating a higher resistance to deformation. In the samples with increasing amounts of pearlite, an increasing number of cracks were observed along the pearlite grains.

Table 5 from ref. [31]

	Testing in	Armco iron	0.2% C	0.45% C	0.8% C
Yield Strength MPa	Air	165	255	367	409
	26%H_2SO_4, 1000 A/m^2	190	275	383	428
Ultimate Strength MPa	Air	302	336	631	852
	26%H_2SO_4, 1000 A/m^2	344	334	585	806

Singh et al [32] did a series of tests to document the effect of ferrite grain size on strengthening of steel in environments with cathodic hydrogen charging. LAS with 0.1 wt% carbon were recrystallized at various times to have three different ferrite grain sizes: 8, 21.5 and 32.5 µm. Hydrogen charging at 50 mA/cm^2 was carried out in three different electrolytes: 0.1 N NaOH, 0.1 N H_2SO_4 and 1.4 N H_2SO_4 for time periods varying from 2 to 24 hours. All electrolytes were poisoned with 5 mg/l As_2O_3 to prevent recombination of hydrogen. The samples were then removed and rinsed before tensile testing. The specimens had gauge lengths of 60 mm, and were tested by uniaxial displacement at 1.2 mm/min (strain rate $3.33*10^{-4}$/s). The yield strengths were found to be lower in hydrogen than in air, more so with larger grain sizes. As shown in *Figure 28*, however, the UTS increased with increasing grain sizes in 0.1 N NaOH and in 0.1 N H_2SO_4 after some of the shorter charging durations. In the stronger 1.4 N H_2SO_4 solution though, the UTS decreased with increasing grain sizes and charging durations. The authors believed this was due to blistering under the higher hydrogen fugacity. The effects of grain sizes and charging times on the elongations are also shown in *Figure 28*. All the samples were found to be more ductile in 0.1 N NaOH; more so with increasing grain sizes and charging times, up until the longest charge time. The same was found for the samples in 0.1 N H_2SO_4, but only for the shorter charging durations. As the charging durations increased, a sudden change was met, at which point the samples with the larger grain sizes saw a dramatic reduction in ductility.

In the 1.4 N H_2SO_4 solution, all the samples were less ductile than they were in air, but more so for the smaller grain sizes.

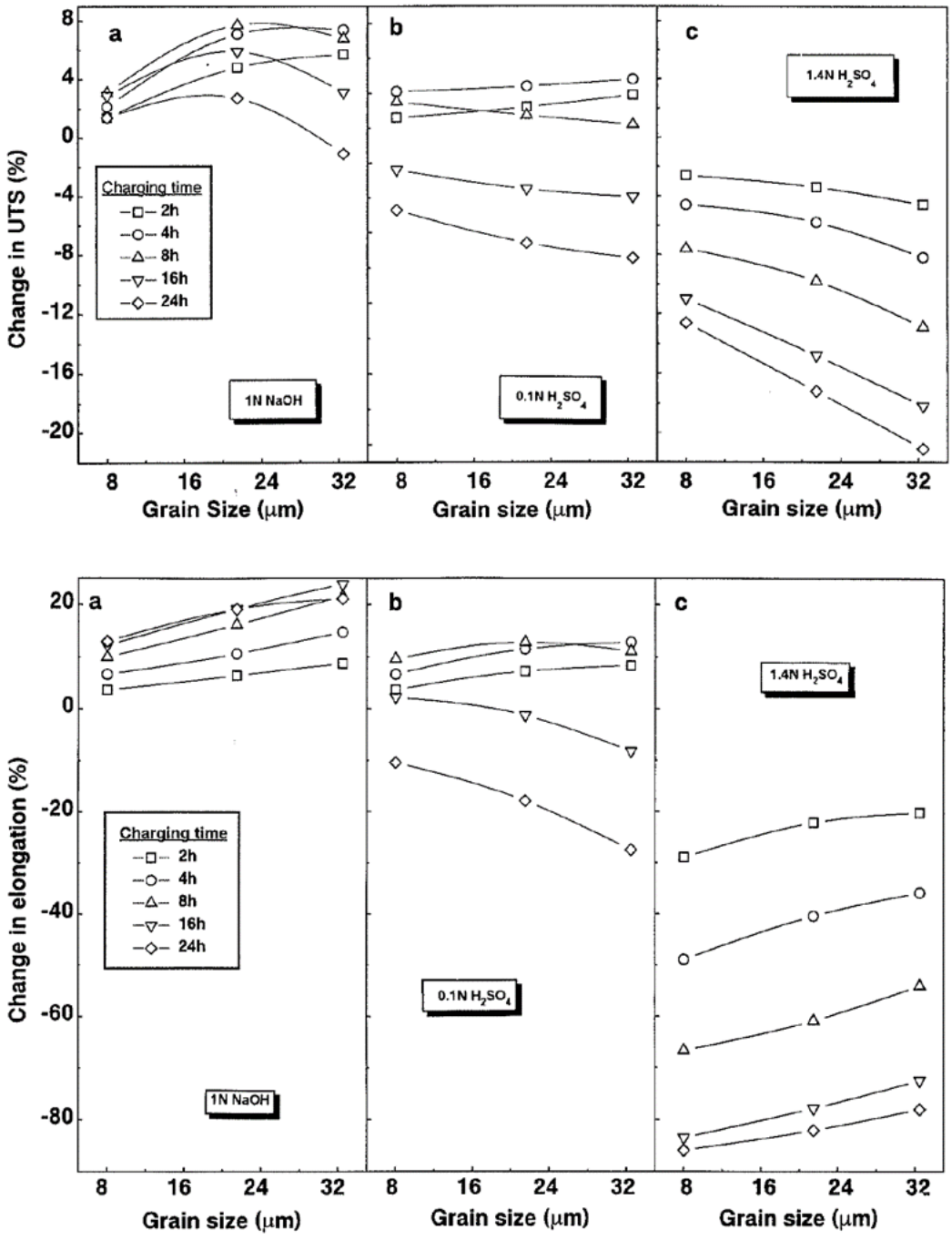

Figure 28 from ref. [32]

In the literature, it is generally accepted that steels with higher strengths are more susceptible to HE [8]. Hardie et al [33] conducted a study of HE susceptibility of banded ferrite-pearlite pipeline steels of API grades X60, X80 and X100 with average grain sizes of 8,4 and 3 μm, respectively, to document the effects of strengths. The composition of the steels were 0.1–0.15% carbon, 1.4–2.0% manganese, 0.2–0.5% silicon, 0.03–0.05% aluminium, 0.01–0.02% phosphorus and <0.003% sulphur. The samples were tested in air and after charging for 15 minutes at different cathodic current densities in a 0.5 M

H_2SO_4 solution that was poisoned with 5 g/l KH_2AsO_4. Testing was done by SSRT at a strain rate of $2.8*10^{-5}$/s. Their results are shown in *Table 6.* There is a slight scatter in the strengths recorded in air and in hydrogen. Notably, X80 has a higher yield and tensile strength after charging at 0.11 mA/mm^2 than it did in air. The reduction in area for X100 undergoes a very dramatic change from 0.44 to 0.66 mA/mm^2, although the total elongation does not. Images of the fracture surface, as seen in *Figure 29*, showed that the cracks mainly went along ferrite/pearlite interfaces.

Table 6 from ref. [33]

Steel	Current density mA mm^{-2}	Yield stress MPa	Ultimate tensile strength MPa	Failure time h	% Elongation	% Reduction in area
X60	**0**	**527**	**560**	**2.27**	**20**	**78**
X60	0.11	489	545	1.30	8	28
X60	0.44	497	558	1.40	10	25
X60	0.66	505	567	1.51	11	28
X80	**0**	**614**	**650**	**2.31**	**19**	**78**
X80	0.11	624	660	1.18	6	26
X80	0.44	618	634	0.95	4	25
X80	0.66	594	611	1.03	5	17
X100	**0**	**833**	**858**	**2.05**	**17**	**76**
X100	0.03	848	850	1.69	12	67
X100	0.06	828	841	1.35	9	54
X100	0.11	830	843	1.15	6	32
X100	0.22	814	830	1.25	5	32
X100	0.44	825	839	1.09	4	30
X100	0.66	799	801	1.11	6	11
X100[a]	0.66	723	816	1.80	15	77

[a] Left one week in air at room temperature before straining.

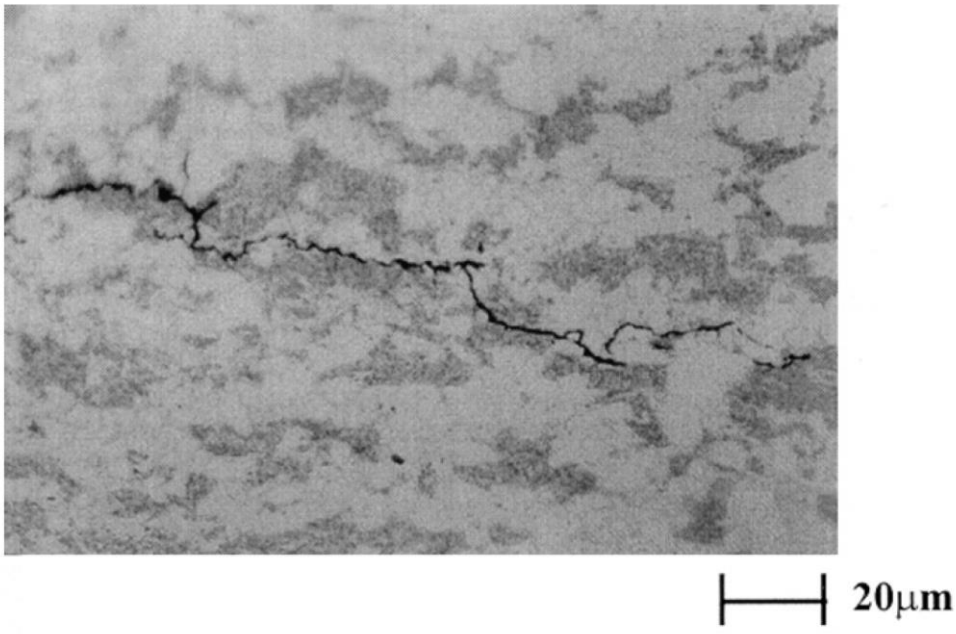

Figure 29 Fracture along ferrite/pearlite interfaces in X60. Picture from ref. [33]

The authors concluded that there was a correlation between the strengths of the materials and the HE susceptibility, but only for the higher current densities.

Loss of tensile ductility of ferrite-pearlite steels is believed to occur mainly due to hydrogen enhancing decohesion at Fe_3C-interfaces, causing growth and formation of voids, leading to cracking [8] [17]. As it follows, a change in the pearlite fraction would be expected to influence the HE susceptibility. Chan et al. [34] studied the effects of differing carbon contents in ferrite-pearlite steels on HE. High purity Fe-C alloys with carbon contents ranging from 0.18 to 0.76 wt% were treated to all have grain sizes of approximately 40 µm. Hydrogen charging was done by charging in NACE H_2S-saturated saline solution for 2 and 4 hours. The samples were then coated with copper to inhibit the leaving of hydrogen. The samples had gauge lengths of 9.65 mm, and were tested by uniaxial displacement at a rate of 1 mm/min (strain rate $1.73*10^{-3}$/s). The results of this are shown in *Figure 30*.

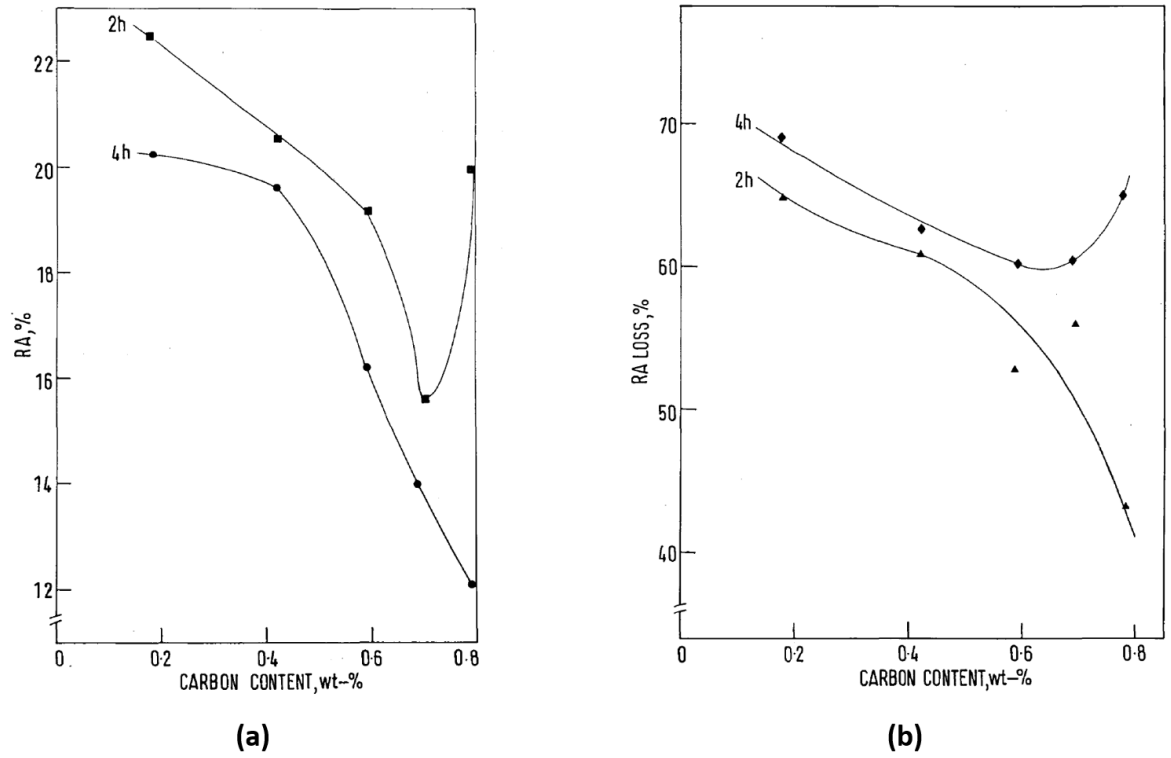

Figure 30 (a) Reduction in area after hydrogenation of ferrite-pearlite steels with varying carbon contents (b) The relative losses in reduction in area when hydrogenated samples were compared to their counterparts tested in air. From ref. [34]

As can be seen in *Figure 30 (a)*, the reduction in area ratios decrease with increasing carbon contents. Since increasing the carbon content also reduces the ductility in air, this result is not entirely unexpected. However, *Figure 30 (b)* shows that the percentwise losses in ductility were greater for the lower carbon contents, and followingly, the steels with lower carbon contents were proportionally more susceptible to HE.

Another factor that plays a role in the embrittlement of ferrite-pearlite steels, is the interlamellar spacing of pearlite. Snape [35] carried out a study in 1968 to evaluate the role of composition and microstructure in SSC of steel. Notched samples were tested by three-point bend testing, similar to NACE Standard Bent Beam Method, as described in section 2.2.5. Before testing, the samples were immersed for six days in a 5 wt% NaCl solution with 0.5% CH_3COOH and 3000 ppm H_2S gas. The results of the bend tests of the microstructures with carbides are shown in *Table 7*. The threshold stress is the highest stress at which no failure occurred during the test period of 28 days.

Table 7 Threshold Stress Values of Normalized and Tempered and lsothermally Transformed Steels Free of Untempered Martensite. Description and table from ref. [35].

No.	Steel Type	0.2% Yield Stress, psi	Microstructure	Threshold Stress, psi(1)
1D	Plain Carbon	34,900	Coarse Lamellar Carbides	>Yield Stress
2F	2% Ni Steel	47,200	Coarse Lamellar Carbides	>Yield Stress
1E	Plain Carbon	49,300	Coarse Lamellar Carbides	>Yield Stress
1C	Plain Carbon	50,000	Coarse Lamellar and Spheroidized Carbides	>Yield Stress
1F	Plain Carbon	54,500	Fine Lamellar Carbides	>Yield Stress
2G	2% Ni Steel	62,900	Fine Lamellar Carbides	>Yield Stress
25H	Commercial 4340	68,300	Coarse Lamellar Carbides	>Yield Stress
2H	2% Ni Steel	68,500	Fine Lamellar and Spheroidized Carbides	>Yield Stress
25I	Commercial 4340	80,700	Coarse Lamellar Carbides	56,000
26B	Commercial 4140	86,500	Lamellar and Spheroidized Carbides	52,000
4H	2.5% Mn Steel	94,100	Fine Lamellar Carbides	38,000
26C	Commercial 4140	100,700	Coarse and Fine Lamellar Carbides	30,000
25K	Commercial 4340	103,400	Fine Lamellar Carbides	31,000
26E	Commercial 4140	104,700	Fine Lamellar Carbides	31,000
25G	Commercial 4340	111,400	Lamellar and Spheroidized Carbides	33,000

(1) Threshold Stress = Yield strength x highest percentage of yield deflection at which no failure occurred in 28 days. Where the threshold stress was greater than the yield stress, no estimate was temped.

Looking at *Table 7*, most of the steels with coarse lamellar carbides have threshold stress intensities that are greater than their yield strengths. The steels with finer lamellar carbides are stronger, but the threshold stress intensities are substantially lower relative to their yield strengths. The steel with the lowest threshold stress is AISI 4140 when it is treated to be composed of both coarse and fine lamellar carbides. The effect of finer lamellar carbides appears to be more damaging when it comes to HE of the steels that contain more alloying elements, such as AISI 4340.

Chan [36] studied the effect of different microstructures and carbon contents on hydrogen trapping and diffusion in steels. The samples were charged in NACE H_2S and saline solution for various time periods, and the hydrogen contents were measured afterwards by the vacuum hot extraction method. The diffusion rates were found by using methods developed by Demarez et al. [37] and by a Devanathan-Stachurski [38] permeation cell. Residual hydrogen was measured using a carrier-gas fusion apparatus (Strohlein H-mat 250). To assess the influence of grain sizes on hydrogen trapping, pure iron samples with grain sizes varying from 30 to 200 µm were tested. The results of this are shown in *Figure 31*. Ferrite-pearlite steels of different carbon contents and interlamellar spacings were also tested. The results of these tests are shown in *Figure 32*. The effects of carbon content on the apparent diffusivity is shown in *Figure 33*.

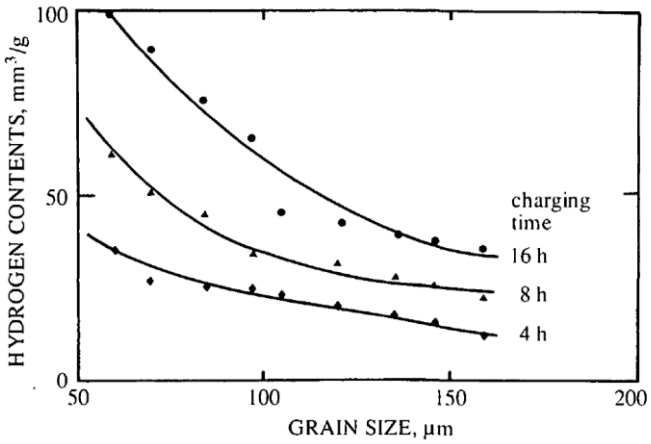

Figure 31 Effect of pure iron grain sizes on hydrogen content. Figure from ref. [36]

As can be seen in *Figure 31*, the hydrogen content decreased with increasing ferrite grain sizes. This was believed to be due to hydrogen trapping in the grain boundaries; an increase in the grain size means a decrease in the total grain boundary length.

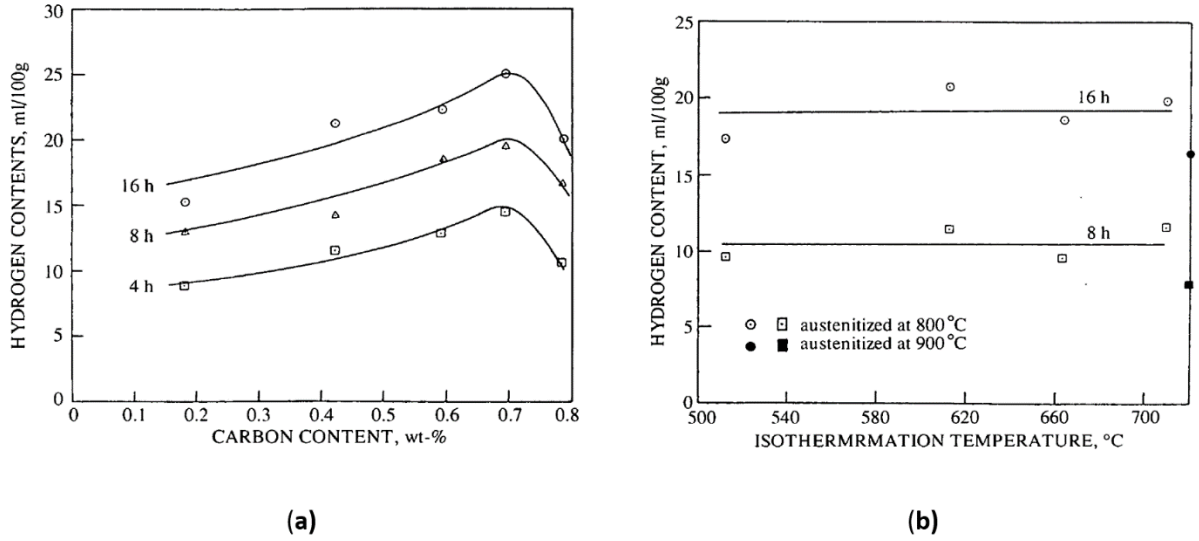

Figure 32 (a) The effect of carbon content on hydrogen trapping (b) Hydrogen content of a 0.59 wt% C steel that was austenized at different temperatures to have different interlamellar spacings of pearlite. [36]

Figure 32 (a) shows the effect of carbon content on hydrogen trapping of ferrite-pearlite steels. Up until the eutectoid composition, an increase in the pearlite fraction caused more trapping of

hydrogen. This was believed to suggest that the ferrite/pearlite interfaces are stronger hydrogen traps than pearlite/pearlite interfaces. *Figure 32 (b)* shows the results of the hydrogen trapping tests where a 0.59 wt% C steel was austenized at different temperatures to have different interlamellar spacings, the lowest temperature being 512°C, and the highest being 709°C, after which the interlamellar spacings were 0.1 and 0.5 µm, respectively. The conclusion was that the interlamellar spacing does not have a significant effect on the hydrogen trapping ability.

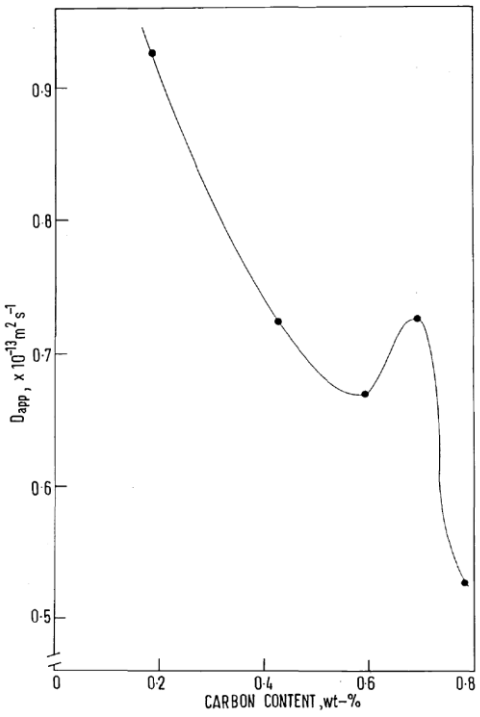

Figure 33 The effect of carbon content on apparent diffusivity in Fe-C steels. From ref. [34]

As seen in *Figure 33*, an increase carbon content was found to reduce the hydrogen diffusivity of ferrite-pearlite steels.

Summary

- Increases and decreases in strength in air and in a hydrogen-containing environment may be found. This may or may not be impacted by the ferrite grain size. At low hydrogen contents, a decrease in yield strength and increase in elongation may occur.
- At a low hydrogen fugacity, a larger ferrite grain size may cause less susceptibility to HE. At intermediate to high hydrogen fugacity, a smaller grain size is expected to be less susceptible. At a hydrogen fugacity that is great enough to induce blistering, the grain size is not believed to play a significant role.
- Changes in material strengths in air are not believed to greatly affect the HE susceptibility, unless the hydrogen fugacity is high.
- An increase in the pearlite fraction is believed to make the steel less ductile, but proportionally less susceptible to HE. Furthermore, the diffusion rate will decrease and the trapping ability will increase.
- Finer pearlite is thought to be more susceptible to HE. Differences in interlamellar spacings of pearlite are not expected to significantly impact the diffusion and trapping behaviour.

2.3.3 Effects of Nickel on Hydrogen Embrittlement of Ferrite-pearlite Steels

Dunlop [26] performed the NACE Standard Bent Beam [19] test on normalized steels that had chemical compositions as given in *Table 8*. To study the effects of cathodic protection, ASTM A203 Grade E was also tested with different cathodic current densities at different partial pressures of H_2S with the same experimental setup as was used for the NACE Standard Bent Beam test, though for 15 days only. The results of this are shown in *Table 9*.

Table 8 NACE Standard Bent Beam test of ASTM A203 grades B and E. Sc is in 10^4 psi. Thus, Sc values of 2.5 and 1.5 are roughly equivalent to 173 and 103 MPa, respectively. The yield strengths of 57.7 and 52.1 thousand psi are roughly equivalent to 398 and 359 MPa, respectively. Table from ref. [26]

(30 days at room temperature in 0.5 Wt% acetic acid with 1 atmosphere partial pressure of H_2S)

less than 22 HRC

Low Nickel Steel	Nominal Nickel Wt%	Hardness, Brinnell	S_c
ASTM A203(1)			
Grade B	2-1/4	148	~2.5
Grade E	3-1/2	169	~1.5
ASTM A350			
Grade LF3	3-1/2	161	<1

Analyses:	C	Mn	P	S	Si	Ni
Grade B	0.12	0.37	0.015	0.028	0.18	2.21
Grade E	0.11	0.52	0.009	0.030	0.20	3.35

Mechanical Properties of Normalized (1 hour at 1500 to 1550 F) 1/2 inch plates

	YS, psi	UTS, psi	% Elongation in 2 Inches
Grade B	57,700	77,200	24
Grade E	52,100	83,900	24

As shown in *Table 8*, the S_c values are lower for A203 Grade E than it is for Grade B, and the main compositional difference is the Ni content. Grade E has a higher Mn-content, lower yield strength, higher tensile strength and Brinell hardness than Grade B, all of which may have affected the results somewhat. As pointed out on the figure, the hardness of all the alloys are lower than 22 HRC, which is the hardness restriction set in ISO 15156 [1].

Table 9 Results of the bent beam tests of steel ASTM A203 Grade E with cathodic protection. Table from ref. [26]

(15 days at ambient temperature in 0.5 Wt% acetic acid with H_2S as shown continuously sparged at 10 cc/minute)

Test Apparatus	A Hydrometer Cylinder		B Modified Resin Kettles		
Specimen Type	S_c	S_c	S_c	S_c	U-Bend[1]
Specimen Ref.	941-62-26	941-62-25	941-79-1	941-79-2	941-79-3
Cathodic Current ma/cm^2	5.5[2]	0	0.45[3]	0	0
Partial Pressure H_2S, atm	0.01	0.01	1.0	1.0	1.0
Nominal Max. Stress, S, psi x 10^{-4}	20	20	20	20	–
Stress Corrosion[4] Cracking Results	0	X	Slight	X	X

(1) 1/4 x 2 x 1/16 inch bent around 1/2 inch ϕ mandrel and restrained with bolt.
(2) Anode was platinum wire.
(3) To minimize possible side reactions, a carbon steel anode (current density on anode = 0.02 mA/cm^2) was used, thus making the anode reaction $Fe = Fe^{++} + 2e^-$ (followed by $Fe^{++} + S^= = FeS\downarrow$).
(4) X indicates cracking; 0, no cracking.

The results in *Table 9* show that cathodic protection caused a decrease in the embrittlement of ASTM A203 Grade E. This was a somewhat unexpected result, since the H_2S in the solution suppressed the recombination of hydrogen, thereby causing more hydrogen to enter the material. The authors took this as evidence that SSC was in fact not because of HE, but rather anodic dissolution.

Koval et al. [39] performed a study of the effects of alloying elements on the susceptibility to SSC. Materials based on Armco iron (0% C), ST20 (0.2% C) and U8 (0.8% C) were alloyed with Ni contents ranging from 0.5 to 20 wt%. The alloys were annealed after casting, and milled and forged into plate specimens measuring 100 X 15 X 2 mm that were normalized and ground to surface finish V7. The specimens were tested at a constant load of $0.9 * \sigma_{yield}$ in a solution with 0.5% CH_3COOH saturated with H_2S gas. The time to failure was measured. Results of this are shown in *Figure 34*.

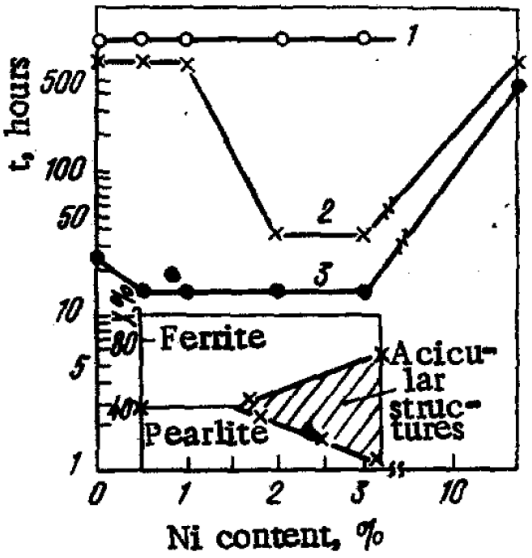

Figure 34 Time to failure of Armco iron (1), ST20 (2) and U80 (3) with different Ni contents. Figure from ref. [39]

As seen in *Figure 34*, the pure iron specimens saw no reduction in the time to failure with increasing Ni contents. ST20 neither, up until the Ni content exceeded 1 wt%, at which point the time to failure decreased drastically. The time to failure of U8 decreased once the Ni content exceeded 0.5 wt%. The authors attributed this to the formation of acicular (needle-like) structures of ferrite and pearlite, brought on by the lowering of the AC_1 and AC_3 temperatures that occurs when alloying with Ni. In addition, the fact that Ni increases the pearlite fraction was also pointed out as a possible cause of the higher susceptibility to SSC. [39]

Since the study by Koval et al. [39] attributed the higher SSC susceptibility of ferrite-pearlite steels with higher Ni contents to be partly due to the formation of acicular structures, a literature search was done to assess the SSC susceptibility of microstructures that contain acicular structures. Zhao et al. [40] studied the role of different microstructures on SSC of pipeline steels. Steels consisting of acicular ferrite, equiaxed ultrafine ferrite, and banded ferrite-pearlite, were tested by NACE Standard Bent Beam test [19]. Two different chemical compositions, shown in *Table 10,* were used in the making of the three different microstructures.

Table 10 from ref. [40]

Steel	C	Si	Mn	Cu	Ni	Nb	V	Ti	Al	Mo	S	P	O	N
1	0.025	0.24	1.56	—	—	0.04	0.02	—	—	0.32	0.0006	0.002	0.0043	0.0062
2	0.07	0.25	0.9	0.2	0.2	0.04	0.04	0.015	0.023	—	0.0015	0.007	0.004	0.004

Steels of chemical compositions that were the same as steel 1 were treated to produce microstructures A and B, which consisted of acicular ferrite and ultrafine ferrite, respectively. Steel 2 was made to produce microstructure C, a banded ferrite-pearlite microstructure. The results of the NACE Standard Bent Beam tests are given in *Table 11*.

Table 11 Results of bent beam tests for different microstructures. A is acicular ferrite, B is ultrafine equiaxed ferrite, and C is banded ferrite-pearlite. Table from ref. [40]

	A		B		C	
S, MPa	Number of Specimen	Number of Cracking Specimen	Number of Specimen	Number of Cracking Specimen	Number of Specimen	Number of Cracking Specimen
90 pct YS	2	0	2	0	2	0
630	2	0			3	0
700			2	0		
770	2	0			3	0
840			2	0		
910	2	0			5	0
1000			2	0		
1050	2	0	2	0	4	3
1120	3	0	3	0	3	3
1260	3	0	2	2	2	2
Sc, MPa	more than 1260		1190		1008	

The results in *Table 11* show that the critical stress intensity S_C was highest for the acicular ferrite-dominated microstructure, and lowest for the banded ferrite-pearlite microstructure.

Husby et al. [41] conducted a study to evaluate the effects of Ni on the hydrogen transport kinetics of LAS. The hydrogen permeabilities of ferrite-pearlite low alloy steels with nominal Ni contents of 0, 1, 2 and 3 wt% were tested at 15, 45 and 70°C, using a Devanathan-Stachurski [38] permeation cell. The results of the diffusion rate calculations are shown in *Figure 35,* the hydrogen contents in sub-surface lattice and trap sites are shown in *Figure 36*, and the hydrogen permeation transients are shown in *Figure 37*.

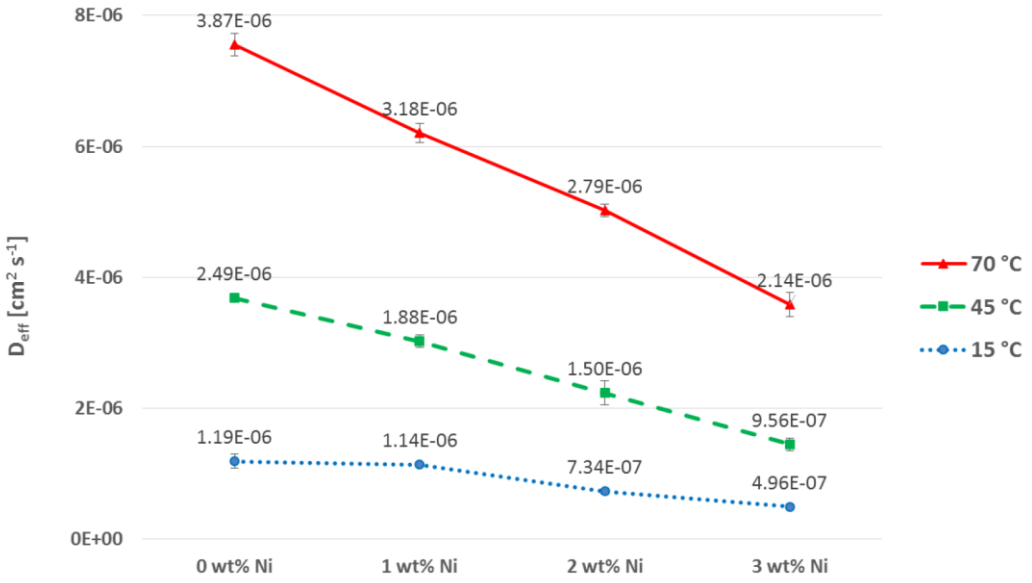

Figure 35 Diffusion rates of ferrite-pearlite LAS with different Ni-contents. Figure from ref. [41]

As seen in *Figure 35*, the diffusion rates decreased as the Ni-contents increased; more so at higher temperatures.

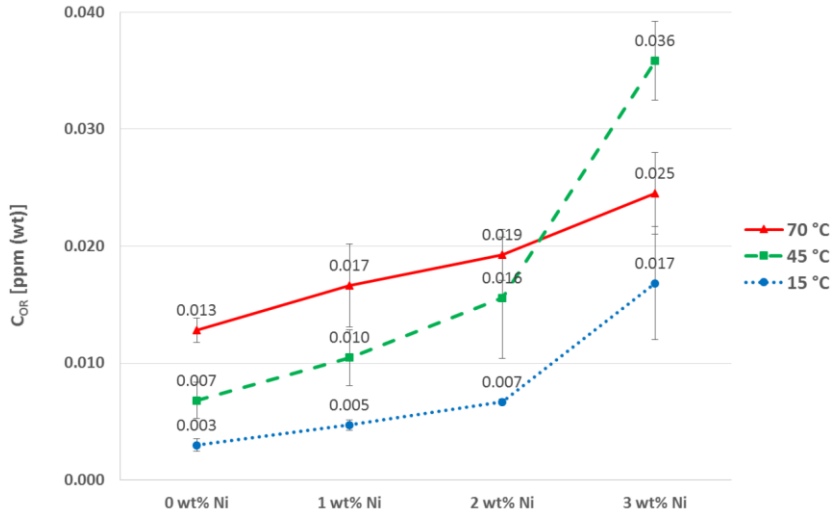

Figure 36 Hydrogen concentrations in lattice and trap sites. The bullets are averages of three permeation transients. Error bars show the standard deviations. Lines added to aid visualization. Description and figure are from ref. [41]

As seen in *Figure 36*, the hydrogen contents in sub-surface lattice and trap sites were found to increase with increasing Ni contents. It should be noted that this was calculated using an equation that accounted only for reversible traps.

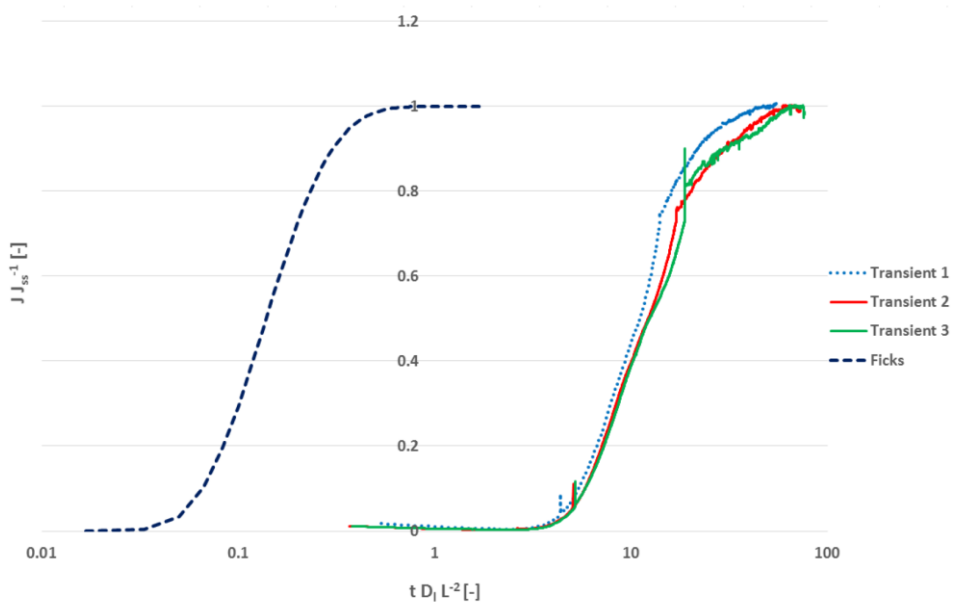

Figure 37 Permeation transients for 3 wt% Ni sample at 45 °C plotted as steady-state normalized permeation flux vs. the logarithm of normalized time. Ideal bcc lattice diffusion is plotted for comparison and is labeled "Ficks". Description and figure from ref. [41]

Figure 37 shows negligibly small differences in the permeation transients for the 3 wt% Ni alloy, which, as per ISO 17081 [42], means that irreversible trapping was not taking place.

The author concluded that an increase in hydrogen solubility and a decrease in hydrogen diffusion rate took place when Ni contents increased, and that there was no evidence of irreversible trapping. It was also stated that the effects of Ni contents on the microstructure may have affected the results – especially due to the increased pearlite fraction in the higher Ni-samples – and that the influence of this was infeasible to quantify in the given materials.

Summary

In summary, changes in the HE susceptibilities are expected to occur when ferrite-pearlite steels are alloyed with Ni. The influencing factors are as follows:

Effects of Ni that increase susceptibility	Effects of Ni that decrease susceptibility
• Segregation of metalloid elements • Possible formation of unevenly distributed acicular structures • Possibly more hydrogen trapping	• Grain size refinement • Lower diffusion rate • Increase in the pearlite fraction

As it follows, analysing the effects of Ni on the HE susceptibility of ferrite-pearlite steels is not entirely straightforward. The effects listed above need to be isolated and considered independently, to reach a conclusion as to whether Ni changes the HE susceptibility to a degree that is consistent with these changes.

3 Experimental and material

3.1 Material Characterization

The chemical compositions of the materials are given in *Table 12*, and an illustration of the heat treatment processes is given in *Figure 38*.

Table 12 Chemical composition of test specimens. Iron (Fe) balances to 100 wt%. From ref [41]

Alloy	Ni [wt%]	Mn [wt%]	Si [wt%]	C [wt%]
0 Ni	0.00	1.30	0.24	0.17
1 Ni	0.97	1.30	0.24	0.17
2 Ni	1.85	1.28	0.23	0.17
3 Ni	2.86	1.30	0.24	0.17

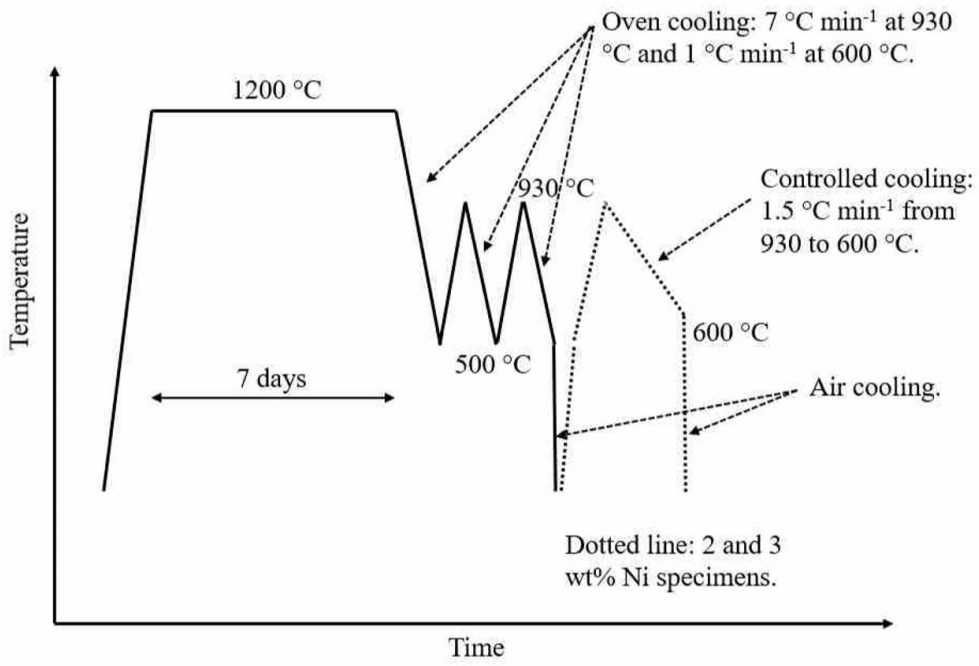

Figure 38 The solid line was followed for the 0 wt% and 3 wt% Ni samples, while the dashed line was followed for only the sample with 3 wt% Ni. Figure is from ref [41]

Seven days of heat-treating at 1200 ℃ was done to homogenize the samples. They were then oven cooled to 500 ℃ and heated to 930 ℃ twice before a final oven cooling to 500, followed by air cooling to room temperature. To obtain comparable microstructures for all the samples, an additional heating step was applied to the sample with 3 wt% Ni [41]. The samples were received after the heat treatment processes.

Because of the differences in Ni contents, there were variations in the microstructural features of each alloy. These changes were characterized by use of SEM imaging. The following factors were considered: overall appearance of the microstructure, average grain size, pearlite fraction, and the interlamellar spacing of the cementite lamellae that make up pearlite.

The samples were ground with increasingly fine grinding paper, the finest being P1200 grit, before polishing with diamond slurry at first 3 and then 1 µm. Afterwards, the samples were immersed in ethanol and placed in an ultrasonic bath. The samples were then electropolished at 40 V for 30 seconds with Struers A2 as the electrolyte.

To document the **overall appearances** of the microstructures, SEM images were taken at various magnifications, the lowest being 200X and the highest 5000X.

The average grain sizes were estimated manually by use of the Heyn Linear Intercept Procedure, described in ASTM E122 [43]. This was done digitally, by creating arrays of fixed horizontal and vertical lines, as shown in *Figure 39*, that were pasted on top of pictures of the microstructure of each alloy. The number of times the lines intersected grain boundaries were then counted. The scale bar in the SEM image was measured, and this was used to measure the line lengths. Finally, the sum of the line lengths was divided by the sum of counted intersections.

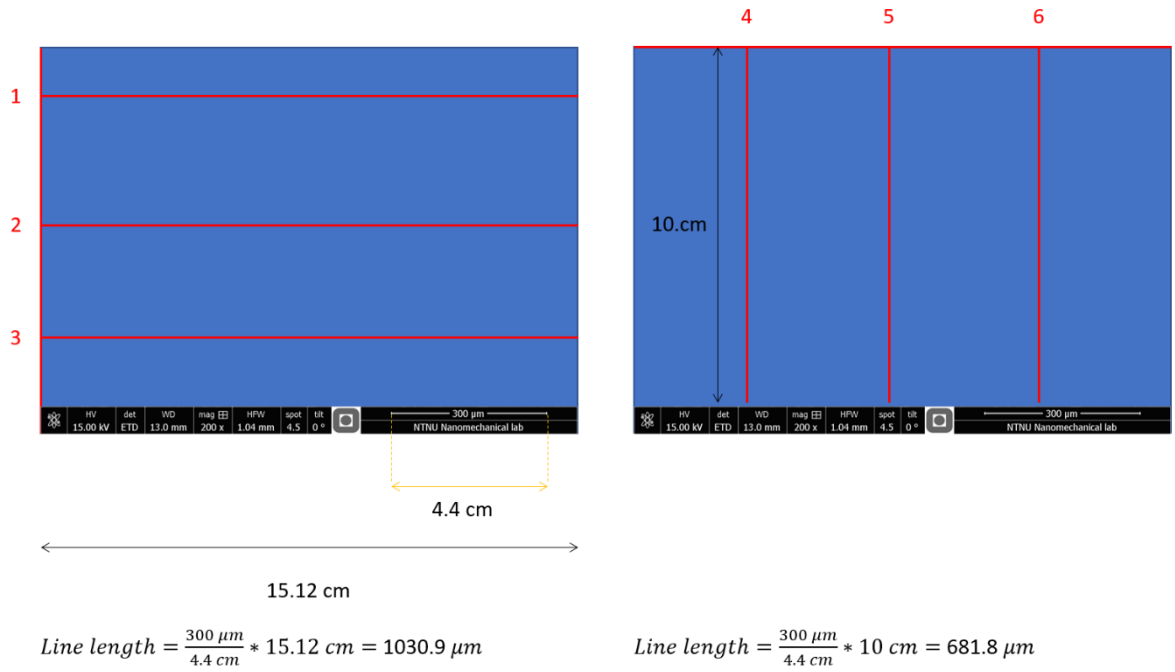

Figure 39 Horizontal and vertical arrays with scale calculations.

The pearlite fraction of each material was estimated using two methods: The first method involved weighing a printout of the microstructure image, cutting out all the visible pearlite, then weighing the picture once more to work out the difference. An example of this is shown in *Figure 40*. The second method was done using image editing software, where the images were converted to 8 bit, and a brightness filter was applied to single out the pearlite grains. This was done by localising the very brightest ferrite grain, and setting the filter just past the point where it was no longer visible. An example of this process is shown in *Figure 41*.

Figure 40 Cutting out visible pearlite manually.

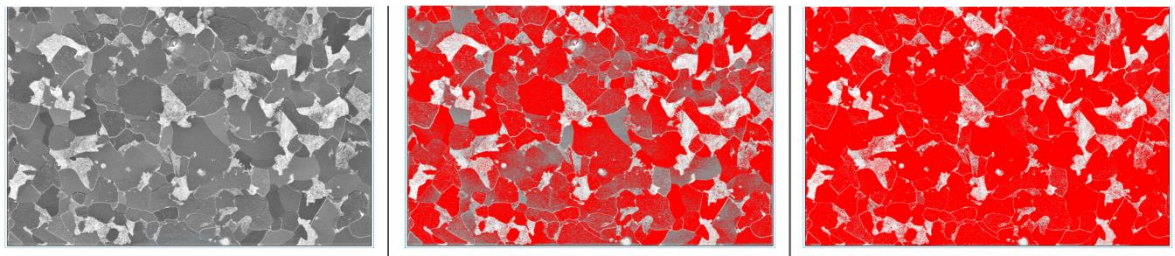

Figure 41 Applying a filter to a microstructure image.

The interlamellar spacing of pearlite was determined as per the recommended practice by Voort [44]. For each alloy, 15 images of randomly selected pearlite colonies were taken at 20,000X. A circular grid with a fixed circumference was used. Intersections between the circular grid and the cementite lamellae were counted manually. An example of the counting process is shown in *Figure 42*.

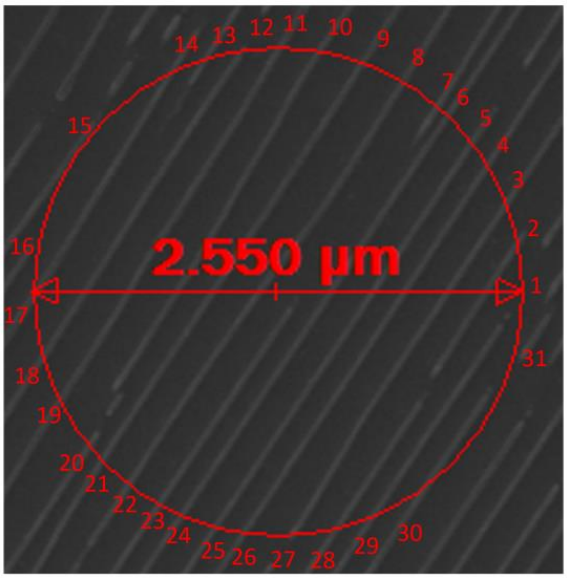

Figure 42 SEM image of pearlite at 20,000X with circular grid. Numbers indicate the amount of counted intersections, starting at the far right of the circle, and going through counter clockwise.

3.2 Polarization curves

Two disks, one of 0 Ni and one of 3 Ni, were used to record polarization curves with hydrogen evolution as the dominant cathodic reaction. The specimens are illustrated in *Figure 43.*

Figure 43 Illustration of the specimens used for recording polarization curves

For both samples, the following procedure was used:

To begin with, all the equipment that would be in contact with the specimen and/or electrolyte was rinsed in cold water, distilled water, and ethanol. The 3.5 wt% NaCl solution, which was to be used as the electrolyte, was placed in a sealed beaker with an inlet tube through which nitrogen gas flowed from a tank, to supress the oxygen in the solution.

The test specimen was ground with increasingly fine sandpaper, the finest being P1200 grit. The specimen was then rinsed with distilled water and ethanol, and inserted in a beaker filled with ethanol. The beaker, with both the ethanol and test specimen still inside, was placed in an ultrasonic bath for one minute. The specimen was placed in the sample holder.

The setup was assembled as shown in *Figure 44*.

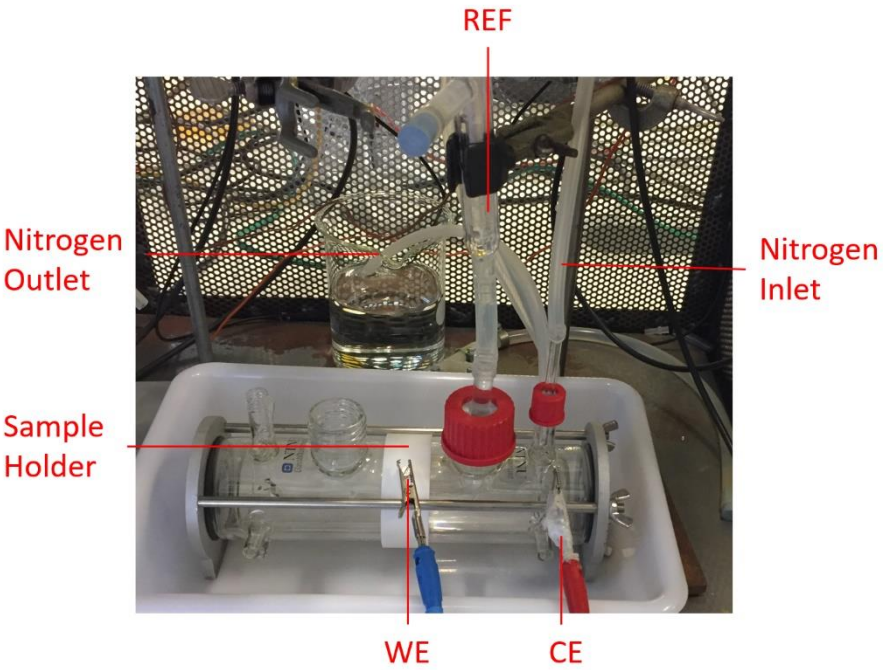

Figure 44 Setup for recording polarization curves. The chamber and tubes are filled with the 3.5 wt% NaCl solution.

REF was the reference electrode, which in this case was Ag/AgCl. Before use, its potential was controlled by measuring it in a setup with a known potential

WE was the working electrode, which in this case was the LAS specimen.

CE was the counter electrode, which in this case was a spool made of platinum.

The inlet was used to let in a continuous flow of nitrogen gas, whereas the outlet was used to release nitrogen gas and gas from the corrosion reactions.
After the setup was assembled, the OCP (open circuit potential) was left to stabilize, which took approximately one hour, before the polarization was initiated. The polarization was done from -1150 mV to 0.1 V vs Ag/AgCl with a speed of 0.2 mV per minute. The temperature was measured to be 21.5 ℃

Figure 45 shows the specimens after testing, and the diameters of the corroded areas.

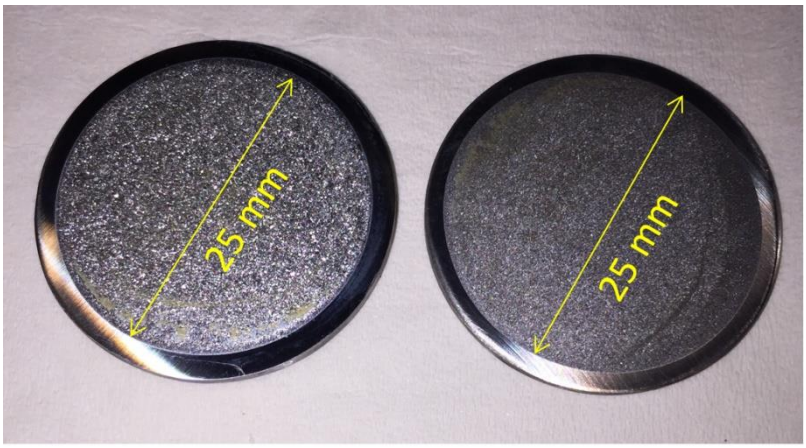

Figure 45 Picture of the specimens after the polarization curves were recorded. 0 Ni to the left, and 3 Ni to the right. Both the diameters of the corroded areas were 25 mm.

3.3 Slow Strain Rate Testing

A sketch of the test specimens used for SSRT is shown in *Figure 46*.

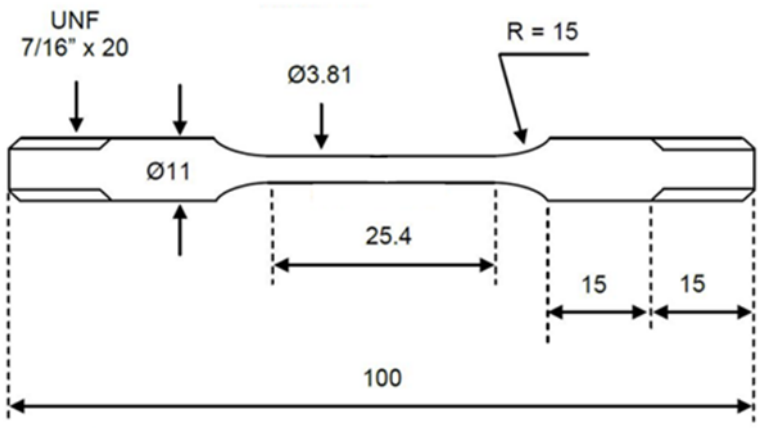

Figure 46 Sketch of SSRT specimen

An overview of the SSR tests that were performed is given in *Table 13*

Table 13 SSRT Overview of tests

Test Series	Alloys Tested	Environment	Hydrogen Charging
Air	0 Ni, 1 Ni, 2 Ni and 3 Ni	Air	None
H1	0 Ni, 1 Ni, 2 Ni and 3 Ni	3.5 wt% NaCl Solution	Potentiostatic
H2	0 Ni, 1 Ni, 2 Ni and 3 Ni	3.5 wt% NaCl Solution	Potentiostatic
H3	0 Ni, 1 Ni, 2 Ni and 3 Ni	3.5 wt% NaCl Solution	Galvanostatic
H4	0 Ni, 1 Ni, 2 Ni and 3 Ni	3.5 wt% NaCl Solution	Galvanostatic
IRT	0 Ni and 3 Ni	3.5 wt% NaCl Solution	Galvanostatic

Cleaning, preparing and measuring the specimen

Before SSR tests, the specimens were cleaned, prepared, and measured as follows:

Compressed air was used to remove dirt in the threads at both ends of the specimens. They were also rubbed with a paper with ethanol. The specimens' gauge areas were ground with P1200 grit sandpaper, sprayed with ethanol, and then measured. Three locations of the gauge areas were measured: bottom, middle and top parts. Two measurements perpendicular to each other were taken at each location. The specimens were rinsed in cold tap water, distilled water, and ethanol. They were then placed in a container with ethanol, which was put in an ultrasonic bath for one minute. Finally, the specimens were dried with a hair dryer.

Initiating SSR tests

An image of the SSRT machine is shown in *Figure 47 (a)*, and the equipment used to fasten the sample in the machine is shown in *Figure 47 (b)*.

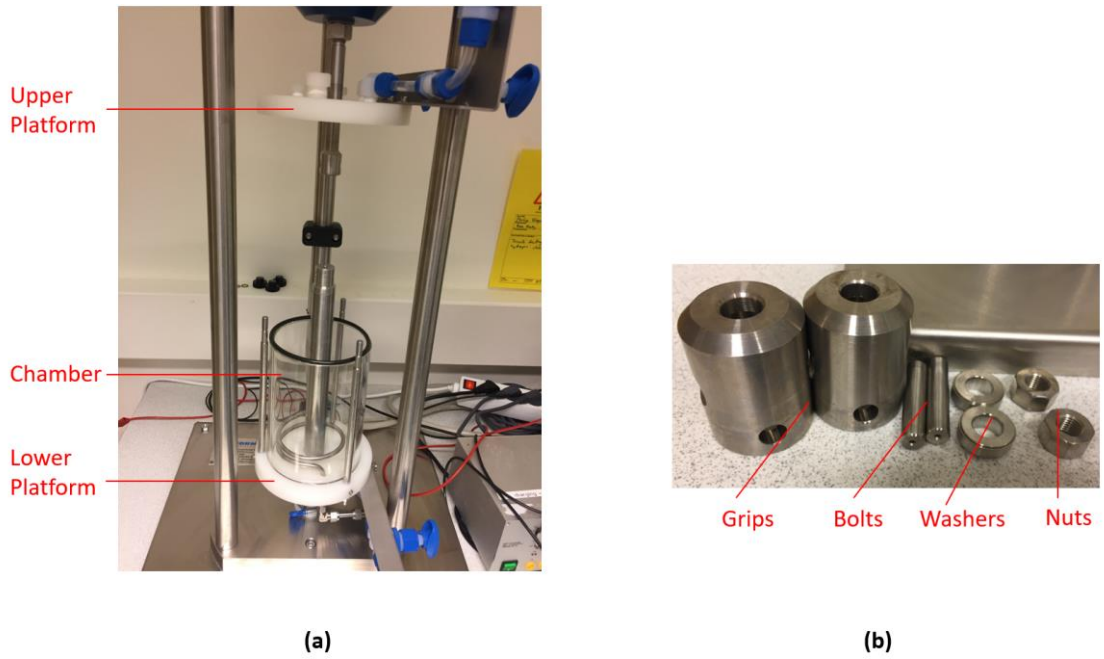

Figure 47 (a) SSRT Machine (b) Equipment used to fasten sample.

The upper and lower grips of the SSRT machine were removed, and the specimen was inserted between them. Special care was taken to avoid the gauge area from scraping against the grips during insertion. The washers were inserted, and the specimen was locked in the grips by fastening a nut on each end, which was fastened until it stopped, and then loosened very slightly. This was to allow for a little bit of give, to avoid the nuts getting stuck during testing. The grips with the specimen inside were placed back into the machine, and were locked in place by two rods that were inserted through slots in both grips. During this process, the machine typically had to be adjusted for everything to align properly, and this was done by using the designated software on the connected computer. Once everything was in place, minor manual adjustments were made to make sure that the specimen was centred in both grips.

Using the software on the computer, very small movements were induced, while monitoring the force readings, until the force reading increased. Once the force reading increased, the specimen was checked, to see if it was properly in place and centred. After everything was controlled, the current position was set as the reference for zero force and displacement.

Recording of data was started. For all tests, a resolution of one reading per five seconds was selected. The SSRT settings were checked, and information about the specimen was entered. The gauge length was set to 25.4 mm, and the diameter entered was the mean value of the six measurements. The upper displacement limit was set. SSRT was initiated.

Test Series

The tests in air (referred to as the Air-series) were performed without any additional equipment. The chamber was not used during these tests, leaving the specimens exposed to the ambient environment, as shown in *Figure 48*.

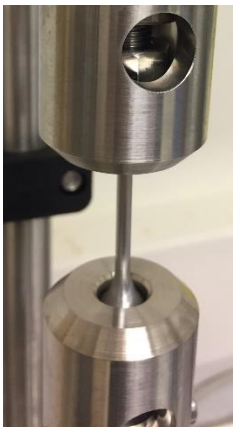

Figure 48 SSRT in air.

The SSR tests with potentiostatic hydrogen charging (referred to as series H1 and H2) were performed with the chamber surrounding the specimen. The chamber was filled with a 3.5 wt% NaCl solution. Hydrogen charging was done using a potentiostat setup, where Ag/AgCl was used as reference electrode, a platinum plate was used as counter electrode, and the specimen was the working electrode. A constant potential of $-1050\ mV$ vs Ag/AgCl was used. Hydrogen charging was started 48 hours (see Appendix A) before SSRT was initiated, and was continued throughout the SSR test. The current on the platinum plate, and the ambient temperature, was measured regularly. A picture of the setup during these tests is shown in *Figure 49*. In these tests, the specimen was in metallic contact with the machine.

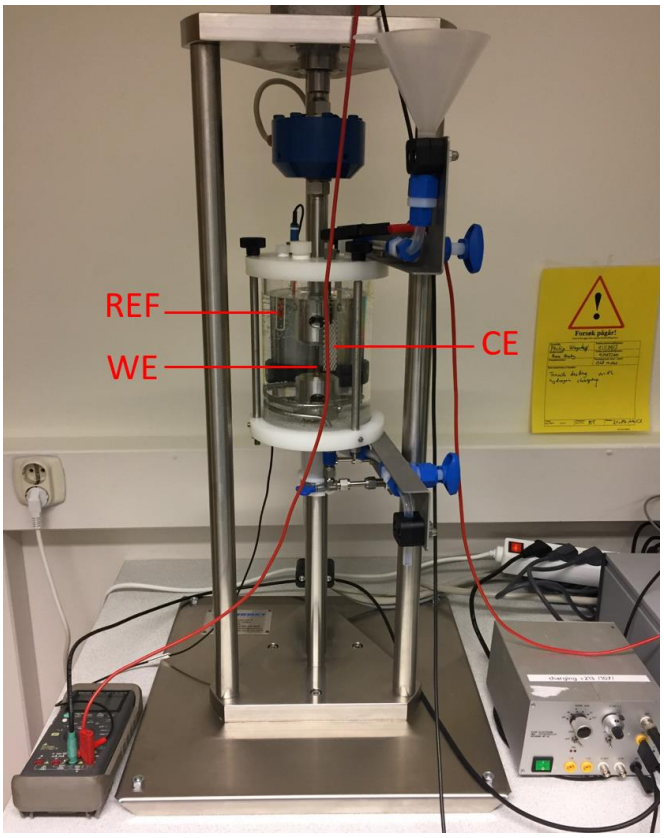

Figure 49 SSRT Setup during potentiostatic hydrogen charging. REF is the Ag/AgCl reference, CE is the platinum counter electrode, and WE is the working electrode.

The SSR tests with galvanostatic hydrogen charging (referred to as series H3 and H4) were performed as the potentiostatic tests were, but with a different potentiostat that could deliver a constant current, and with nitrogen bubbling to suppress the oxygen. The specimen was connected to the potentiostat by two wires; one at each end of the specimen, where they were held in place by nuts. The wires were isolated from the machine by use of ceramic washers. A constant current of -550 mA (15 mA/cm^2 – see Appendix B) was used, and the charging was started 24 hours (see appendix A) before the SSRT was initiated, and continued throughout the test. The potential was recorded every 10 seconds by the potentiostat software on the computer, and temperature measurements were taken once per day. *Figure 50* shows a close-up of the chamber during these tests. During the first series of galvanostatic tests (series H3), the chamber was seen to take on a dusty appearance, as shown in *Figure 51*. This was thought to be due to the counter electrode, which was thus replaced upon completion of the series. The H4 series was tested using the new platinum counter electrode, which, as it turned out, did not fix the dustiness.

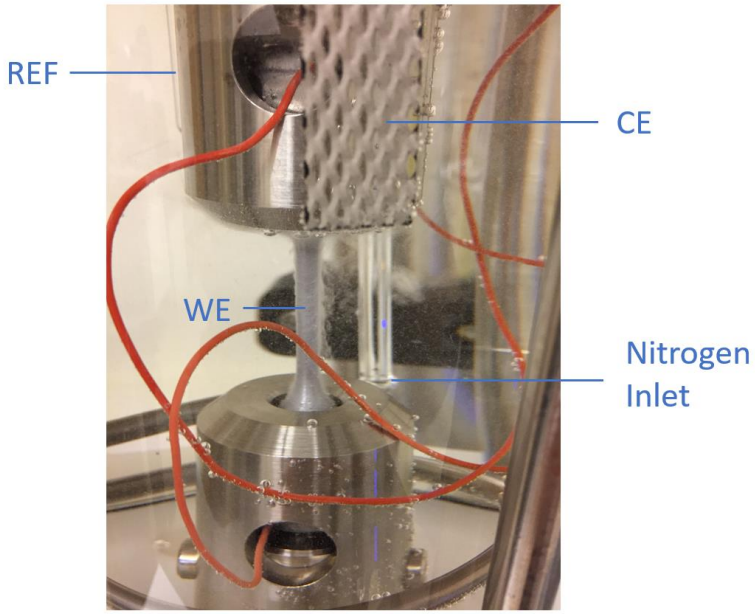

Figure 50 REF is the Ag/AgCl reference (which is obscured by the upper gip on the figure). CE is the platinum counter electrode. WE is the working electrode, which in this case was the test specimen only.

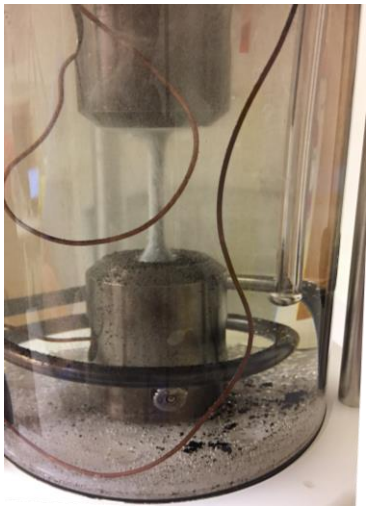

Figure 51 Dusty appearance in chamber.

The irreversible trapping tests (referred to as IRT) were done using the same setup and charging current as was used for the galvanostatic tests. After 24 hours of charging, though, the charging was halted, and the samples were removed, rinsed, and left in a desiccator with silica gel for 11 days before SSR testing.

After all tests, both parts of the fractured specimen were sprayed with ethanol and placed in an ultrasonic bath for one minute. The samples were stored in a desiccator with silica gel.

Between all the tests where hydrogen charging was used, the removable machine parts, such as the grips, bolts, washers, nuts, chamber, and O-rings, were rinsed in warm water, distilled water, and ethanol. The fixed parts of the machine were cleaned with distilled water.

3.4 Scanning Electron Microscopy

The fracture surfaces were examined via SEM. Pictures of the fracture surfaces were taken from two different angles: from above, and from the side, as shown in *Figure 52*.

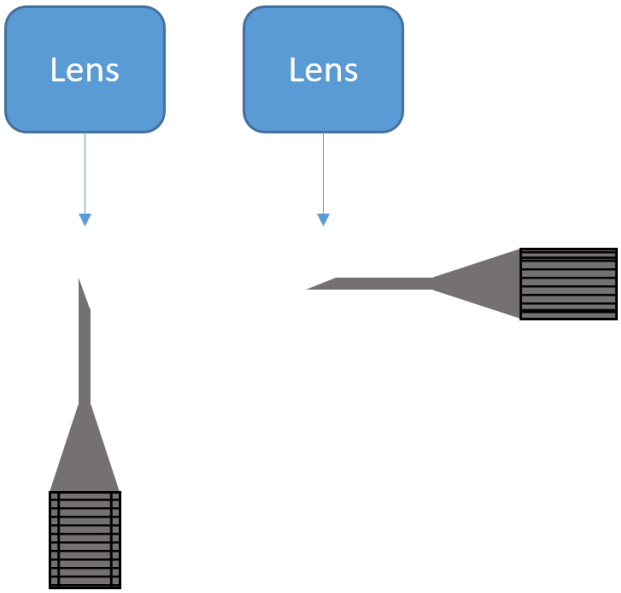

Figure 52 Angles from which the images were taken.

After fine focus was achieved, the specimens' fracture surface diameters were measured by use of the SEM software. Two measurements of each fracture surface were taken: one horizontal and one vertical diameter measurement.

4 Results

4.1 Material Characterization

The micrographs that were taken of the alloys are shown in *Figure 53*.

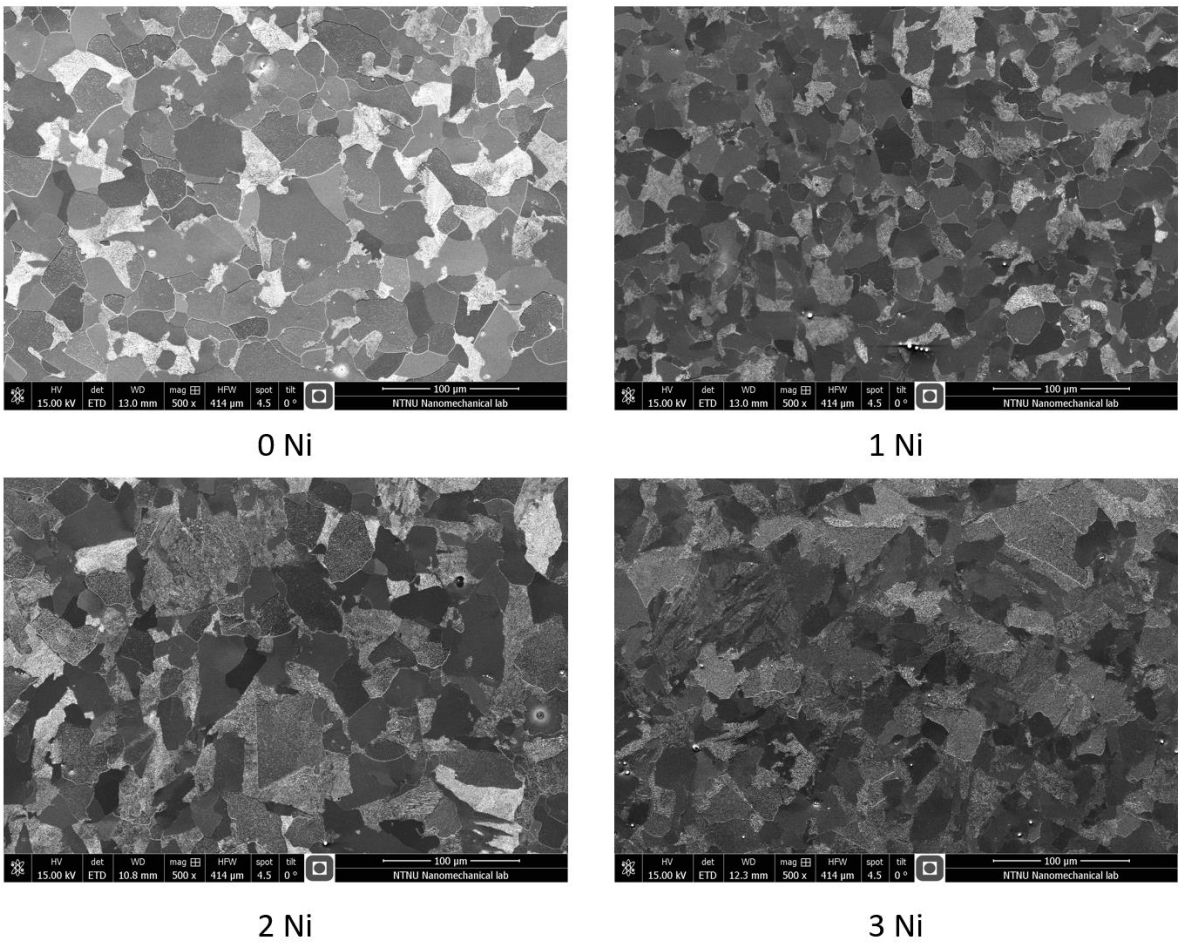

Figure 53 Micrographs. Taken at 500X magnification

Several needle-like structures were observed in the microstructures of 2 Ni and 3 Ni. Close-ups of some of these are shown in *Figure 54*. No such structures were found in 0 Ni and 1 Ni.

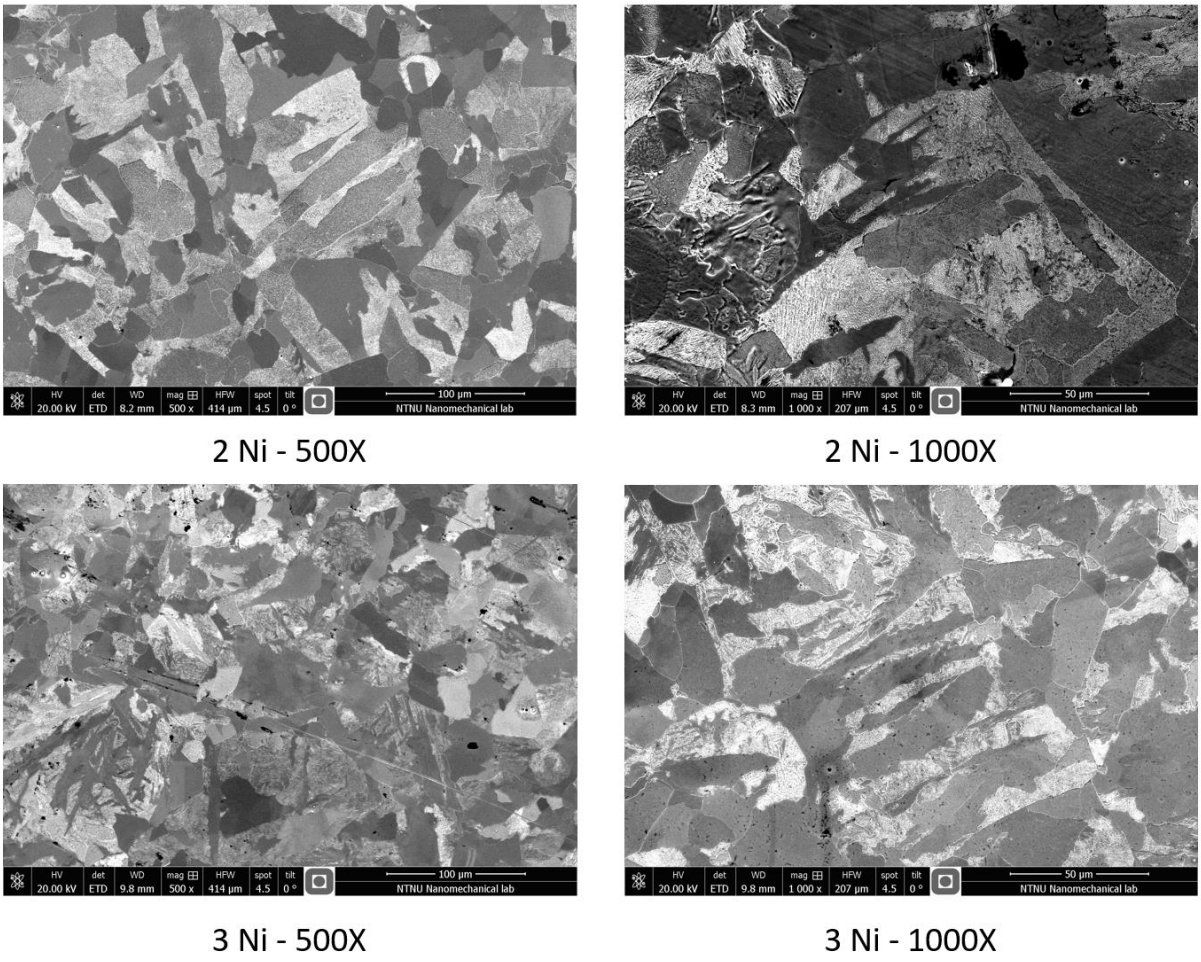

Figure 54 Needle-like structures in 2 Ni and 3 Ni. All four images are taken at separate locations.

Table 14 gives an overview of the microstructure properties that were obtained.

Table 14 Microstructure properties

Alloy	Average grain size [µm]	Pearlite fraction (manual method) [%]	Pearlite fraction (image software method) [%]	Interlamellar spacing of pearlite [nm]
0 Ni	18.2	21.6	18.5	351.4
1 Ni	13.5	22.5	19.6	316.2
2 Ni	17.1	25.6	23.0	323.9
3 Ni	15.5	29.3	25.9	271.9

4.2 Polarization curves

Figure 55 shows the OCP measurements for 0 Ni and 3 Ni. *Figure 56* shows the polarization curves plotted together.

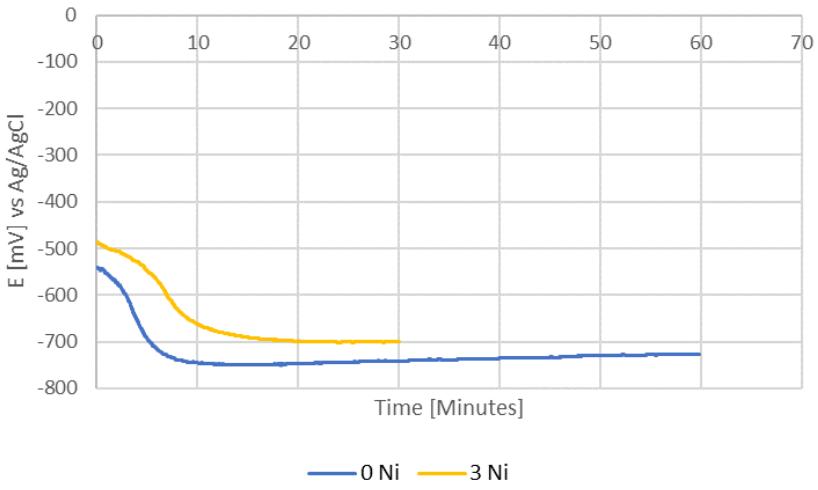

Figure 55 OCP for 0 Ni and 3 Ni.

The stabilized OCP values for 0 Ni and 3 Ni were -728 and -700 mV vs Ag/AgCl, respectively.

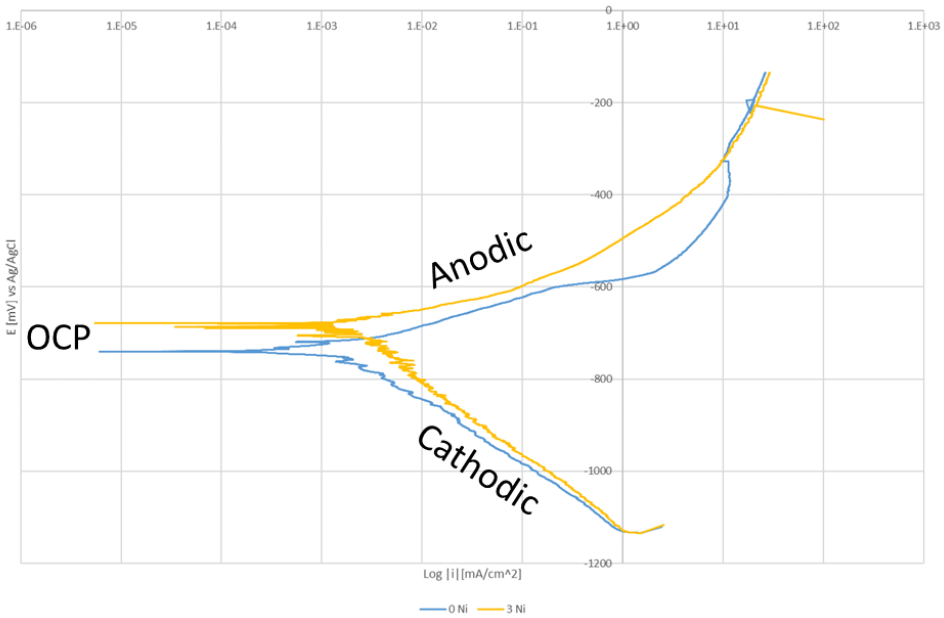

Figure 56 Polarization curves. Anodic and cathodic regions are marked.

The OCP values, as marked on the figure, are the flat lines. The lines that are beneath the OCP correspond to hydrogen evolution on the metal's surface, while the lines that are above the OCP correspond to corrosion of the metal. Both lines are higher up for 3 Ni than they are for 0 Ni, which means that 3 Ni is more noble than 0 Ni.

At a potential of -1050 mV, the corrosion current densities were $0.30\ {}^{mA}/_{cm^2}$ and $0.38\ {}^{mA}/_{cm^2}$ for 0 Ni and 3 Ni, respectively.

4.3 Slow Strain Rate Testing

Figure 57 shows the baseline curves for all the materials tested in air. All the materials containing Ni were stronger than the Ni-free alloy. All the materials, except for 1 Ni, were less ductile in air than 0 Ni. The exact values of these tests are given in *Table 16*.

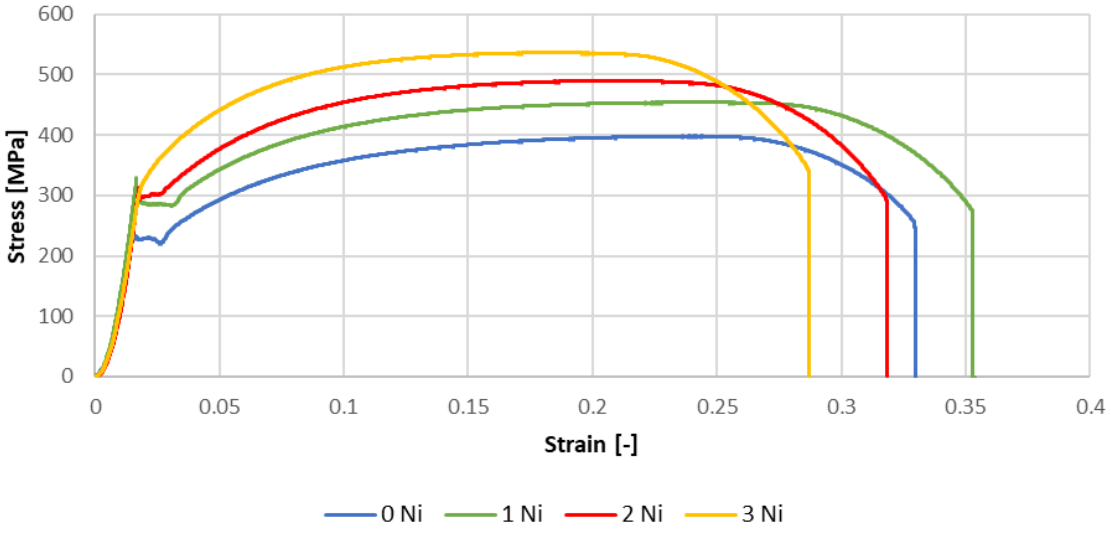

Figure 57 SSRT in air.

Figure 58 shows the baseline tests in air for each material, along with the tests where potentiostatic hydrogen charging was used. As seen on the figure, all the samples underwent a loss in tensile ductility when in the hydrogen-containing environment. Some small strength increases can be seen on the curves as well. The exact values can be seen in *Table 15*.

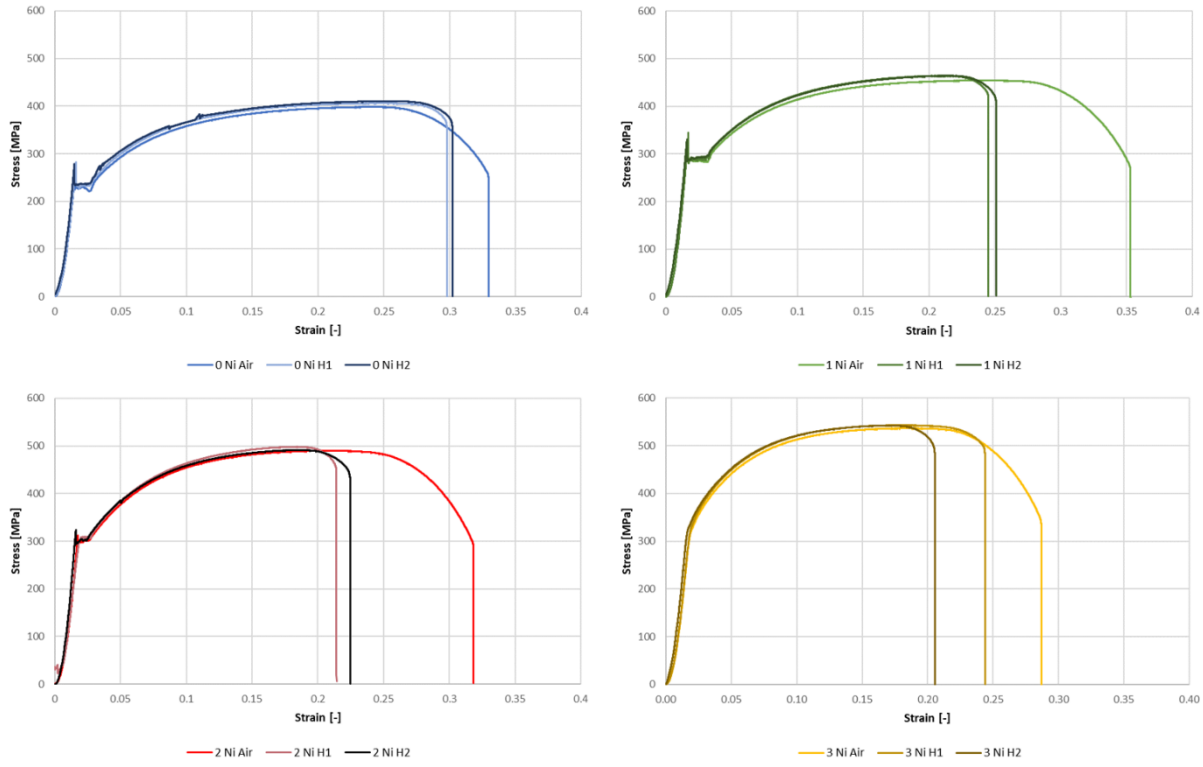

Figure 58 Air tests vs potentiostatic tests (H1 and H2).

Figure 59 shows the baseline tests in air for each material, along with the tests where galvanostatic hydrogen charging was used. A larger decrease in tensile ductility was seen for these tests, but a higher increase in strengths as well. The exact values are given in *Table 16*.

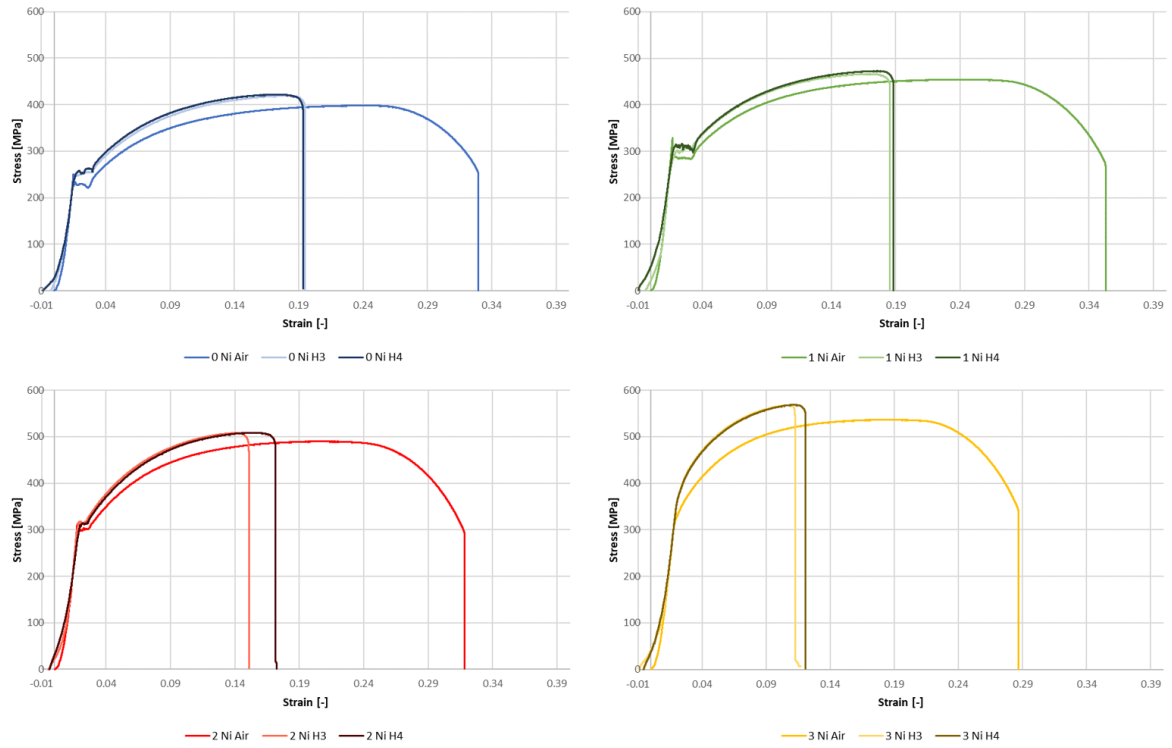

Figure 59 Air tests vs galvanostatic tests (H3 and H4).

Figure 60 shows the baseline tests in air for 0 Ni and 3 Ni, along with the irreversible trapping tests (IRT). As can be seen on the figure, 0 Ni saw an increase in ductility and some minor changes in strength. 3 Ni underwent a loss in ductility, and an increase in strength. Exact values are given in *Table 16*.

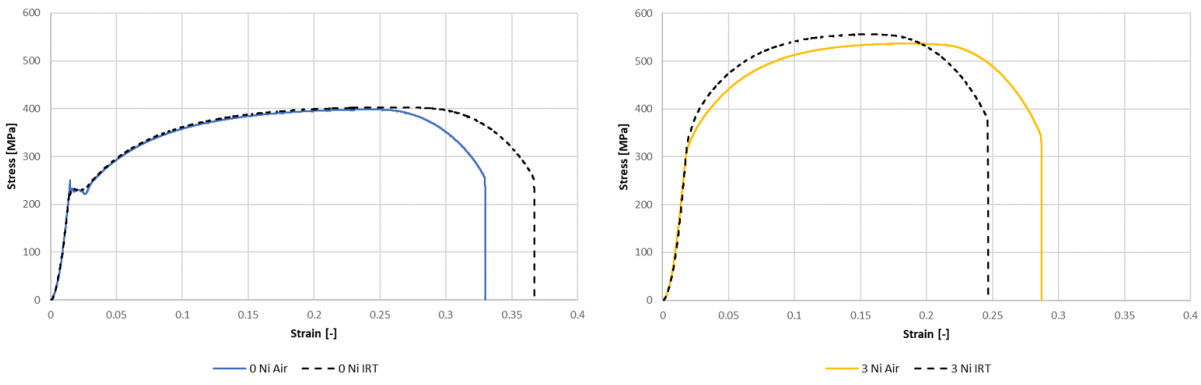

Figure 60 Irreversible trapping tests (IRT)

An overview of all tests, along with information about the test environments, is given in *Table 15*.

Table 15 Overview of different test and environmental factors during testing.

	Environment					Notes
Test	**Hydrogen Charging**	**Precharge time [hrs]**	**Mean Current [mA]**	**Mean Potential vs Ag/AgCl [mV]**	**Mean Temperature [℃]**	A strain rate of $1*10^{-6}$/s was used for all tests.
0 Ni Air	None					
0 Ni H1	Potentiostatic	48	11.2	-1050	23.9	
0 Ni H2	Potentiostatic	48	8.8	-1050	23.5	
0 Ni H3	Galvanostatic	24	550	-2029.80	24.4	
0 Ni H4	Galvanostatic	24	550	-1891.64	24.5	Counter Electrode**
1 Ni Air	None					
1 Ni H1	Potentiostatic	48	14.7	-1050	24.3	
1 Ni H2	Potentiostatic	48	12.9	-1050	24.3	
1 Ni H3	Galvanostatic	24	550	-2113.48	24.6	
1 Ni H4	Galvanostatic	24	550	-1935.25	24.6	Counter Electrode**
2 Ni Air	None					
2 Ni H1	Potentiostatic	48	11.0	-1050	24.1	
2 Ni H2	Potentiostatic	48	16.2	-1050	24.3	
2 Ni H3	Galvanostatic	24	550	-2003.03	24.5	
2 Ni H4	Galvanostatic	24	550	-1917.23	24.7	Counter Electrode**
3 Ni Air	None					
3 Ni H1	Potentiostatic	48	8.3	-1050	23.6	
3 Ni H2	Potentiostatic	48	9.1	-1050	23.8	
3 Ni H3	Galvanostatic	24	550	-2015.35	24.5	
3 Ni H4	Galvanostatic	24	550	-1934.30	24.1	Counter Electrode**
0 Ni IRT	Galvanostatic	24	550	Unknown*	24.4	Sample removed after 24 hours hydrogen charging. SSRT started 11 days later with no charging. Counter Electrode**
3 Ni IRT	Galvanostatic	24	550	-1901.99	24.1	Sample removed after 24 hours hydrogen charging. SSRT started 11 days later with no charging. Counter Electrode**

**The PC crashed during hydrogen charging. The potentiostat continued the polarization independently of the PC, but the measurements were lost.*

***The platinum plate that was used as counter electrode was replaced with another similar platinum plate during the H4- and IRT-tests.*

A different charging time was used for the potentiostatic and galvanostatic tests. This is reviewed in Appendix A. The cathodic current densities of the galvanostatic tests were approximated to be 15 mA/cm^2. (See Appendix B). No attempt was made to estimate the cathodic current densities of the potentiostatic tests, due to the large deviations that were found, and also due to the complicated geometry of the total polarized surface area.

Complete overviews of the strength and ductility measurements are given in *Tables 16* and *17*.

Table 16 Table of strength and ductility parameters for the air tests, potentiostatic tests and galvanostatic tests.

	Strength			Ductility						
Test	**Yield strength (Upper) [MPa]**	**Yield Strength (Lower) [MPa]**	**Tensile strength [MPa]**	**Plastic elongation**	**Plastic elongation Ratio [%]**	**RA [%]**	**RA ratio [%]**	**Time to failure [hours]**	**Time to failure ratio [%]**	**HER* [%]**
0 Ni Air	250.7	227.4	398.4	0.3148		76.07		90.21		
0 Ni H1	282.5	233.0	406.4	0.2820	89.58	35.78	47.04	81.47	90.3	42.1
0 Ni H2	278.8	236.3	410.5	0.2873	91.26	36.27	47.68	82.64	91.6	43.5
0 Ni H3	249.0	252.7	418.9	0.1778	56.46	19.97	26.26	54.13	60.0	14.8
0 Ni H4	258.0	258.2	421.8	0.1787	56.76	20.92	27.51	54.12	60.0	15.6
1 Ni Air	328.7	285.9	454.2	0.3361		78.66		96.52		
1 Ni H1	344.8	292.7	464.1	0.2279	67.80	31.82	40.45	67.02	69.4	27.4
1 Ni H2	331.0	291.8	464.3	0.2423	72.07	35.84	45.56	68.63	71.1	32.8
1 Ni H3	301.0	303.3	466.1	0.1656	49.26	18.70	23.78	51.99	53.9	11.7
1 Ni H4	315.0	309.2	472.7	0.1688	50.21	18.90	24.03	54.36	56.3	12.1
2 Ni Air	312.8	300.0	490.0	0.3008		76.33		87.08		
2 Ni H1	309.5	300.7	498.2	0.1928	64.12	33.23	43.53	58.58	67.3	27.9
2 Ni H2	323.4	300.7	491.4	0.2086	69.36	34.26	44.88	61.46	70.6	31.1
2 Ni H3	317.5	315.0	508.2	0.1319	43.84	15.71	20.58	42.61	48.9	9.0
2 Ni H4	310.0	312.7	508.4	0.1517	50.42	17.41	22.80	48.09	55.2	11.5
3 Ni Air	328.0	None	536.4	0.2667		73.09		78.49		
3 Ni H1	335.0	None	543.2	0.2237	83.88	33.35	45.63	66.72	85.0	38.3
3 Ni H2	330.5	None	542.4	0.1878	70.42	28.60	39.13	56.20	71.6	27.6
3 Ni H3	360.0	None	567.9	0.0922	34.59	13.08	17.90	33.36	42.5	6.2
3 Ni H4	360.1	None	568.6	0.1004	37.66	14.59	19.96	34.64	44.1	7.5

Table 17 Table of strength and ductility parameters of IRT tests. Air tests included for comparison.

	Strength			Ductility						
Test	**Yield strength (Upper) [MPa]**	**Yield Strength (Lower) [MPa]**	**Tensile strength [MPa]**	**Plastic elongation**	**Plastic elongation Ratio [%]**	**RA [%]**	**RA ratio [%]**	**Time to failure [hours]**	**Time to failure ratio [%]**	**HER* [%]**
0 Ni Air	250.7	227.4	398.4	0.3148		76.07		90.2		
0 Ni IRT	230.8	230.7	402.6	0.3502	111.22	76.75	100.9	103.5	114.8	112.2
3 Ni Air	328.0	None	536.4	0.2667		73.09		78.5		
3 Ni IRT	343.0	None	543.2	0.2267	83.88	66.18	90.5	67.1	85.5	75.9

*HER (Hydrogen Embrittlement Resistance) was created in this thesis to supplement the ductility parameters. It was defined as $Plastic\ Elongation\ Ratio * RA\ Ratio * 10^{-2}$. As such, the numbers should ordinarily be within the range of 0 to 100, where 100 means a higher resistance to HE.

The mean values of the plastic elongation and reduction in area ratios for the H1 and H2 tests are represented visually in *Figure 61*. As can be seen, they are all higher for 0 Ni, but they are all similar for the Ni-containing alloys.

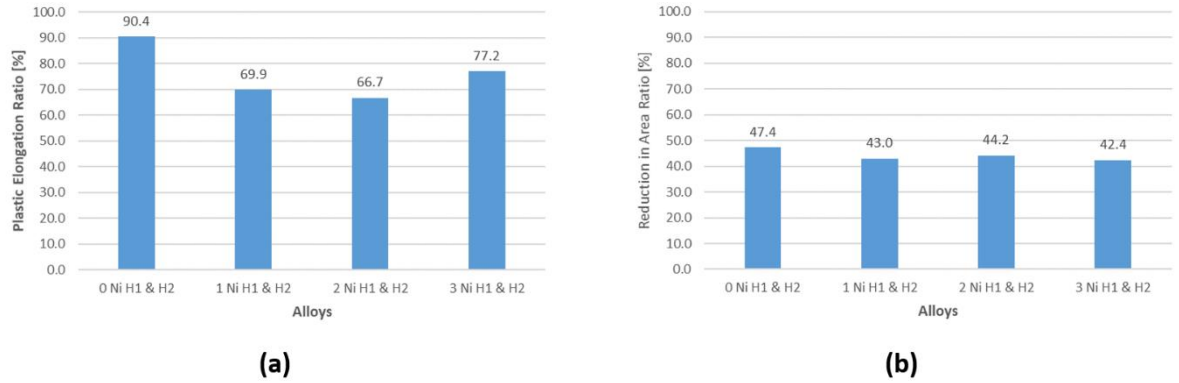

Figure 61 (a) Mean values of plastic elongation ratio for H1 & H2 tests (b) Mean values of reduction in area ratios for H1 and H2 tests.

The mean values of the plastic elongation and reduction in area ratios for the H3 and H3 tests are represented visually in *Figure 62*. As can be seen, all the values decrease with increasing Ni-contents.

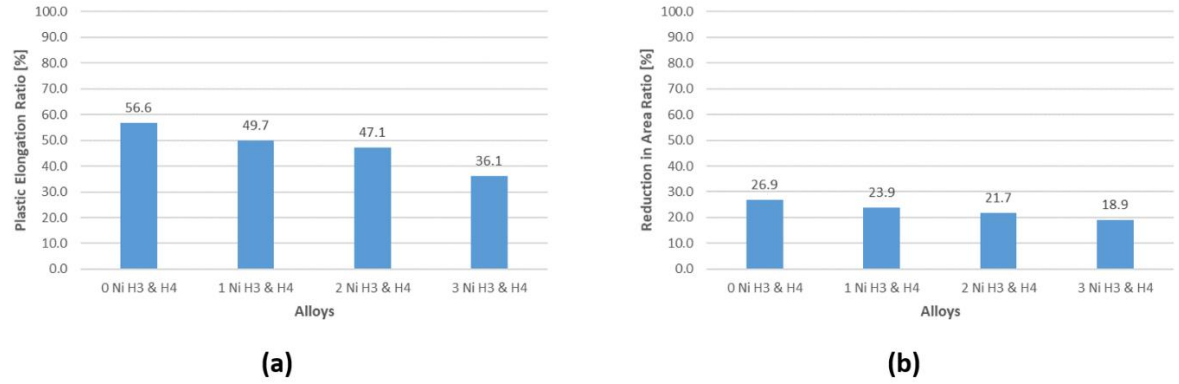

Figure 62 (a) Mean values of plastic elongation ratio for H3 & H4 tests (b) Mean values of reduction in area ratios for H3 and H4 tests.

4.4 Scanning Electron Microscopy

A brief overview of the fracture characteristics for each alloy in each environment is given in this section.

0 Ni

In air, the 0 Ni alloy was seen to have only ductile features. Significant necking occurred before fracture, as can be seen in *Figure 63 (a)*. The surface was characterized by dimple rupture, and several circular inclusions were found throughout the surface, as shown in *Figure 63 (b)*

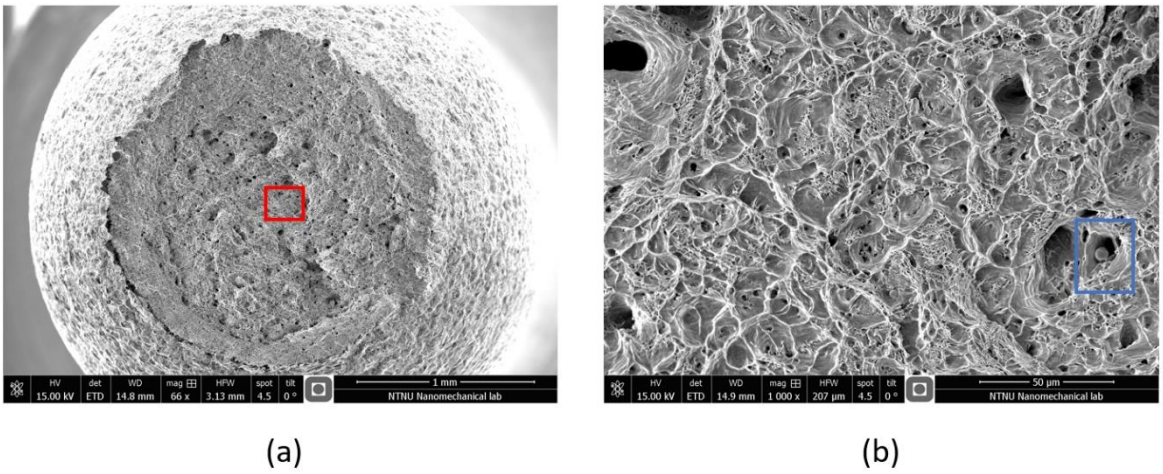

Figure 63 (a) Fracture surface at 66X (b) Close-up at 1000X of the area inside the red box marked in (a). The blue box shows a circular inclusion.

No signs of secondary cracks were found when viewing the sample from the side. A side view is shown in *Figure 64*.

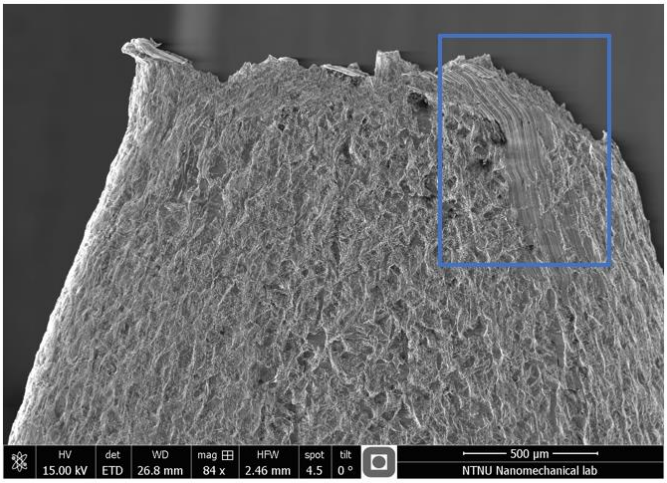

Figure 64 0 Ni Air side view at 84X. The smooth area marked in the blue box was caused by measuring the diameter of the fracture surface area with callipers after SSRT. This was noted, and calliper measurements were not taken of any of the other samples after fracture.

In the test series where hydrogen charging was used, the fracture surface took on more brittle features.

In test series H1 and H2, mixed features of ductile and brittle fractures were observed. Dimples, transgranular cleavage planes, and tearing are shown in *Figure 65*.

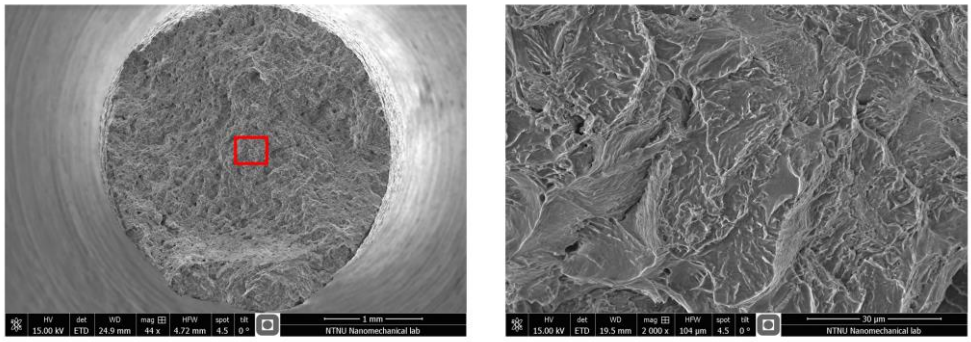

(a) (b)

Figure 65 (a) 0 Ni H1 at 44X (b) Close-up of red box at 2000X

In test series H3 and H4, the evidence of embrittlement was more pronounced. A lot less necking occurred, and there were larger transgranular cleavage planes. At high magnifications, areas of tearing and very small dimples were observed. Small pearlite grains were found between some of the brittle cleavage planes. These findings are shown in *Figure 66*.

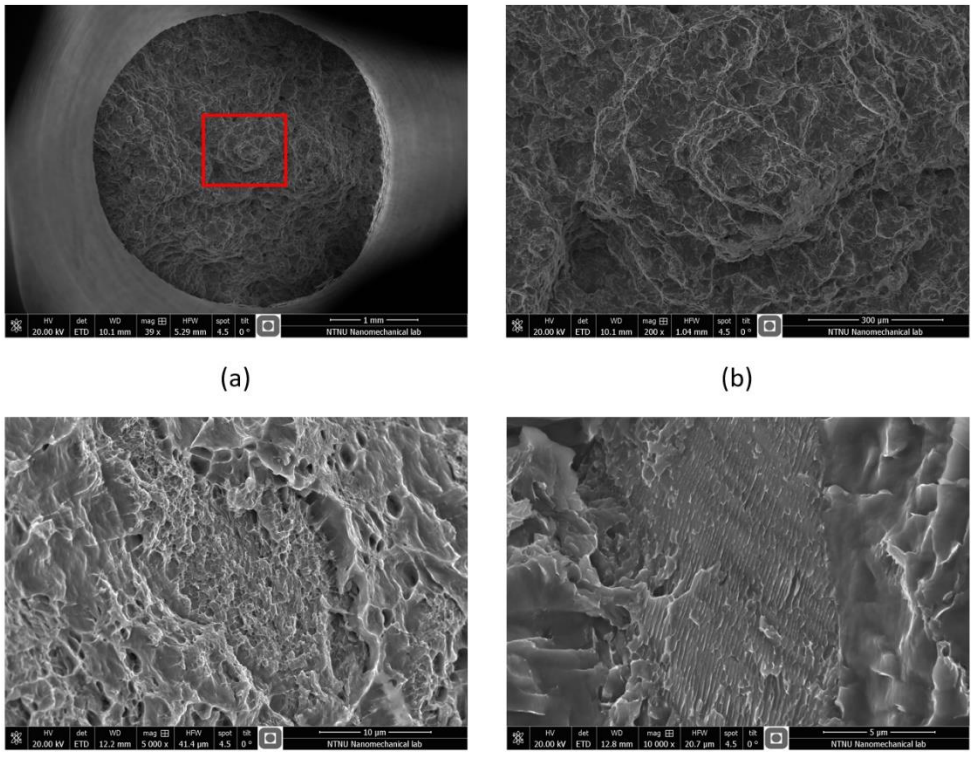

(a) (b)

(c) (d)

Figure 66 (a) 0 Ni H3 at 39X. (b) Close-up of the red box in (a) at 200X. (c) Small and shallow dimples at 5000X (d) Pearlite colony at 10000X

Figure 67 shows secondary cracks down the gauge length of the 0 Ni H2 tests. These were not observed along the entire gauge length

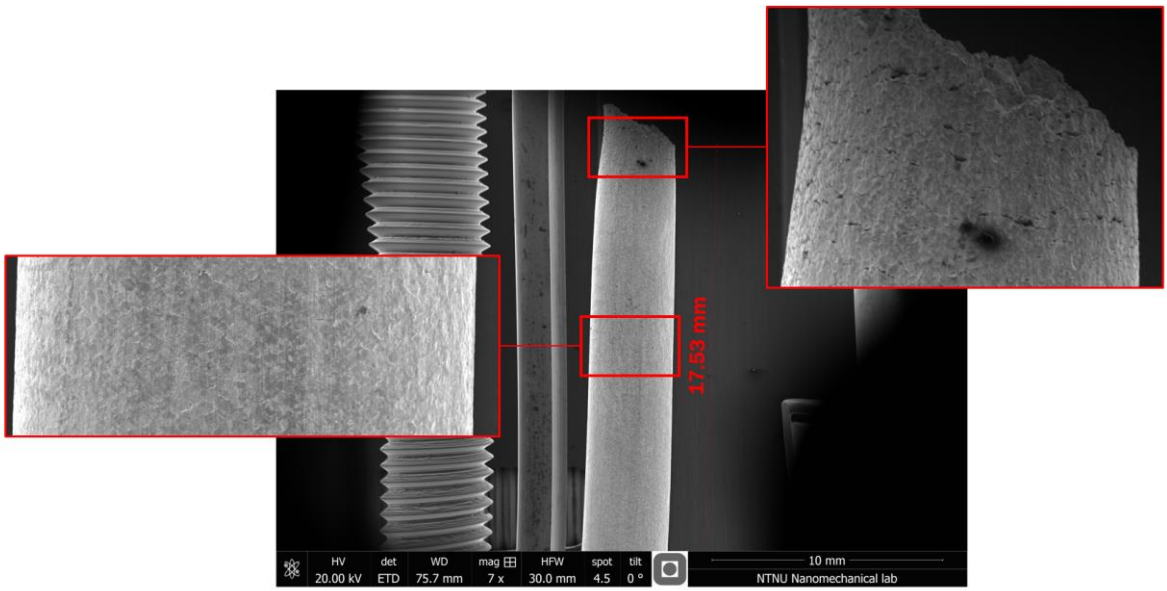

Figure 67 Secondary cracks 0 Ni H2. The highlighted areas show close-ups.

In 0 Ni H4, small secondary cracks were observed along the entire gauge length, as shown in *Figure 68*.

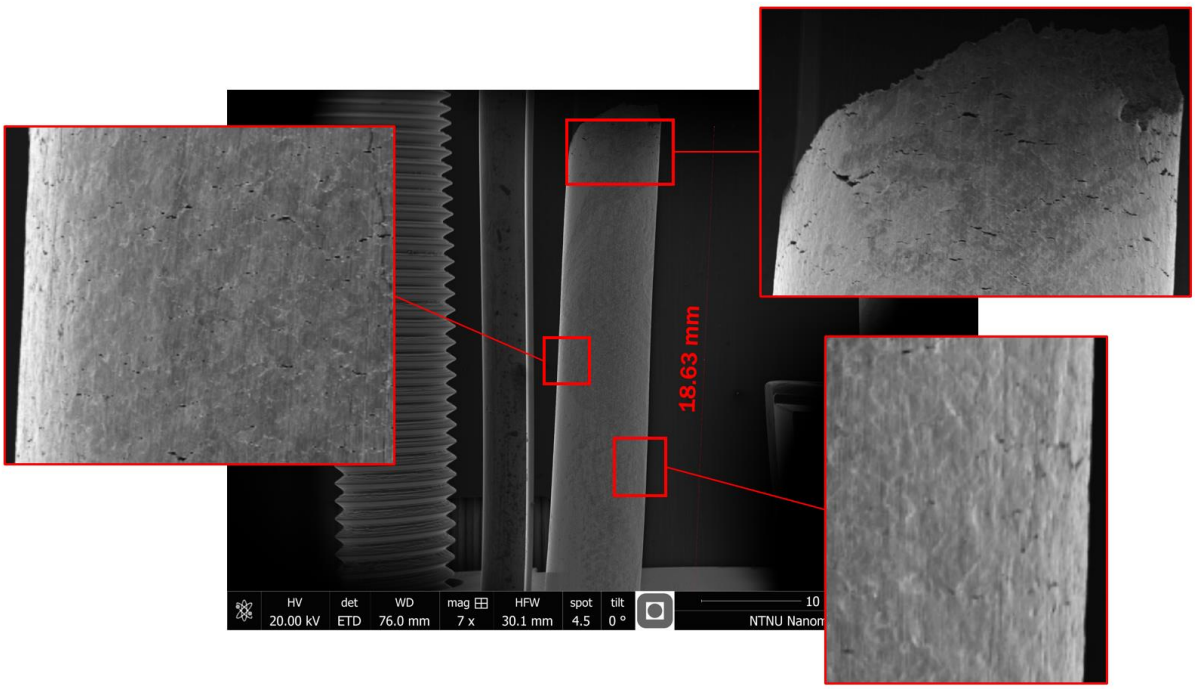

Figure 68 Secondary cracks in 0 Ni H4 with highlighted areas. Secondary cracks were found along the entire gauge length.

1 Ni

In air, ductile features were observed in 1 Ni. As can be seen in *Figure 69*, a lot of necking occurred, and there were deep dimples.

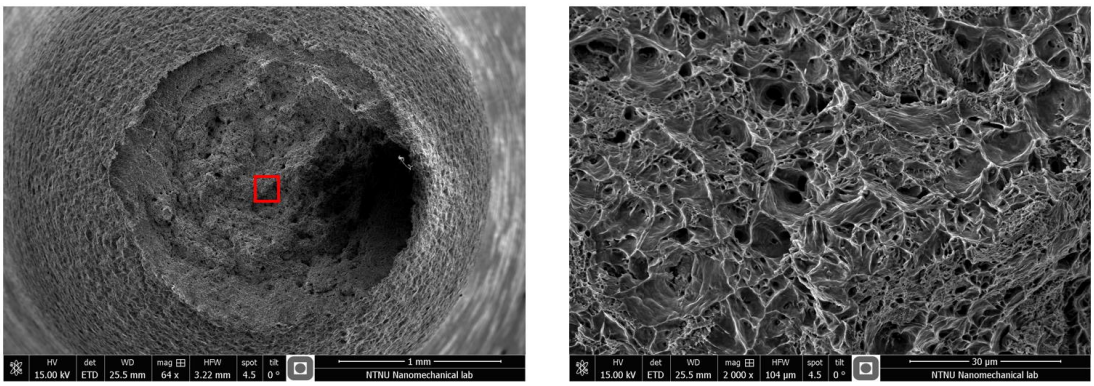

(a) (b)

Figure 69 (a) 1 Ni Air (b) Close up of red box marked in (a).

No evidence of secondary cracking was found, as shown in *Figure 70*.

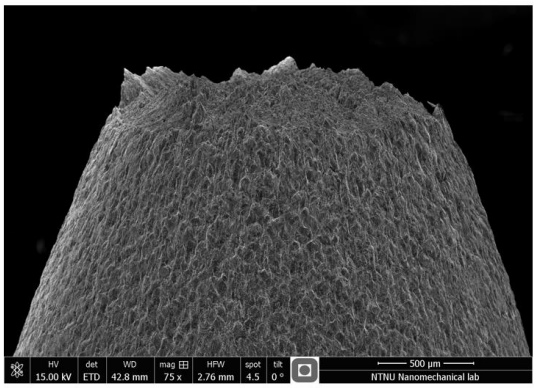

Figure 70 Side view at 75X of 1 Ni Air.

The H1 and H2 tests revealed mixed ductile and brittle features, such as dimple rupture, cleavage planes, and tearing, as shown in *Figure 71*.

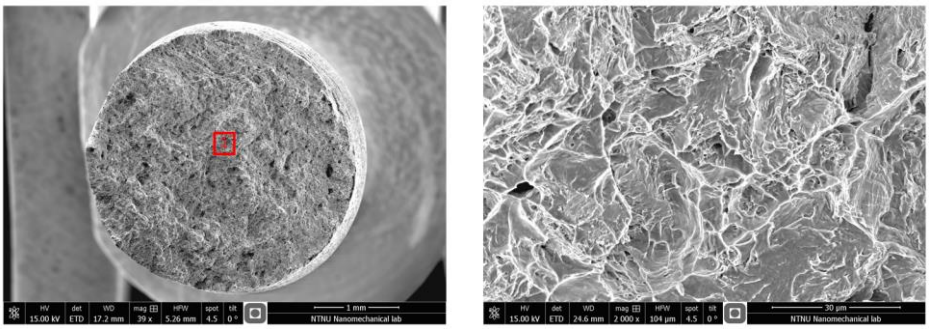

(a) (b)

Figure 71 (a) 1 Ni H2 at 39X (b) Close-up at 2000X of marked area in (a)

In the H3 and H4 tests, the features were increasingly brittle, as shown in *Figure 72*. At higher magnifications, observations of very shallow dimples, as well as pearlite grains, were made.

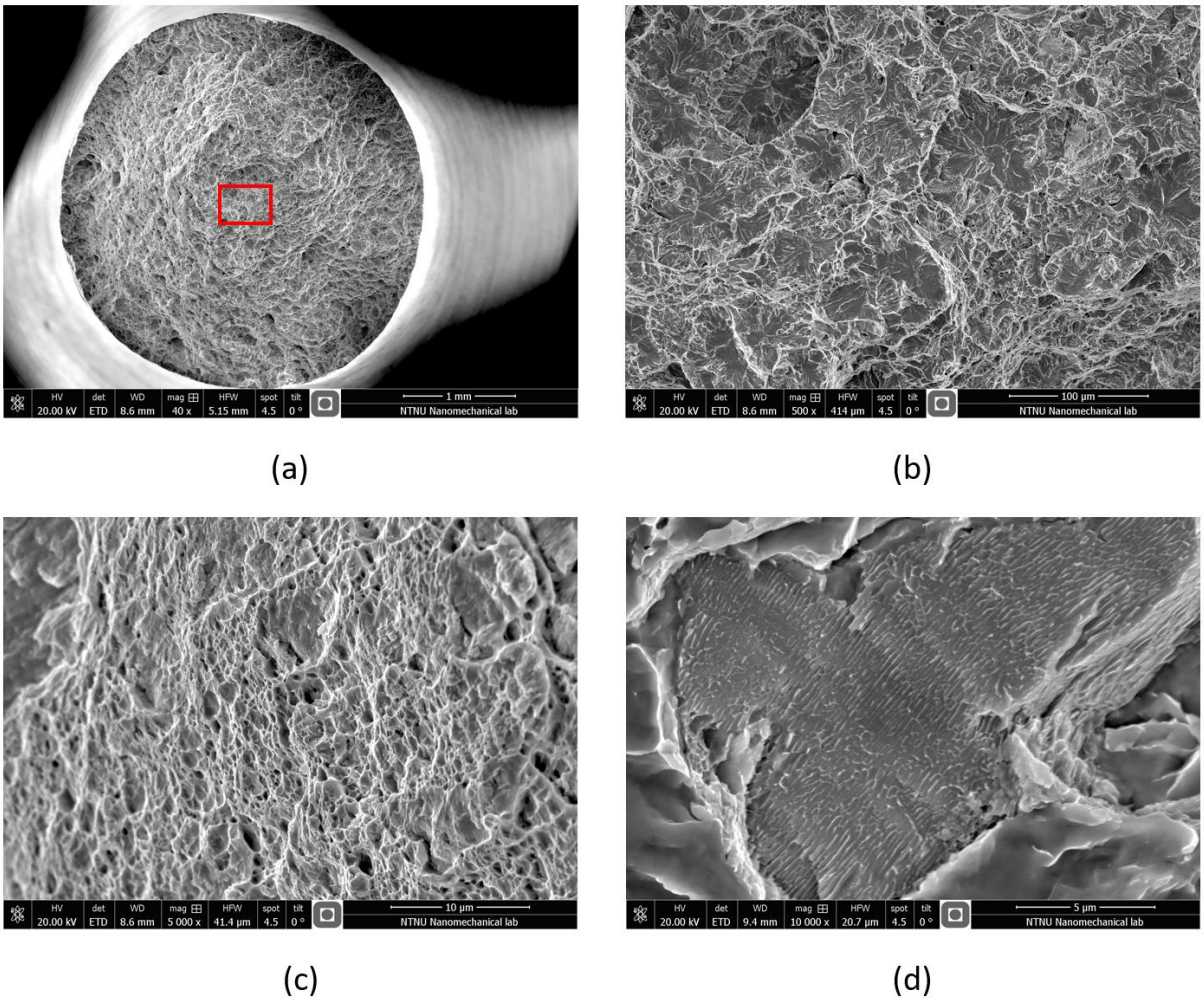

Figure 72 (a) 1 Ni H3 at 40X (b) Close-up at 500X of marked area in (a). (c) Shallow dimples at 5000X in 1 Ni H3 (d) Pearlite grain in 1 Ni H3 at 10000X.

Observations of circular inclusions were made. Usually, several were seen in the same area, as shown in *Figure 73*.

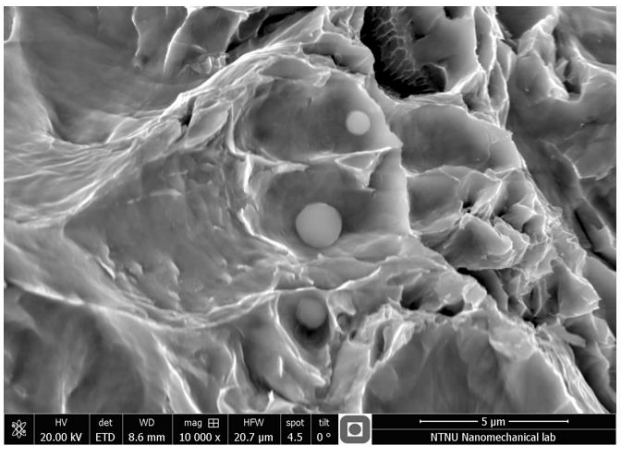

Figure 73 1 Ni H3 at 10000X. An area of multiple circular inclusions.

Figure 74 shows secondary cracks in the 1 Ni H2 test. The lowest highlighted area on the figure marks the lowest point where secondary cracks were observed.

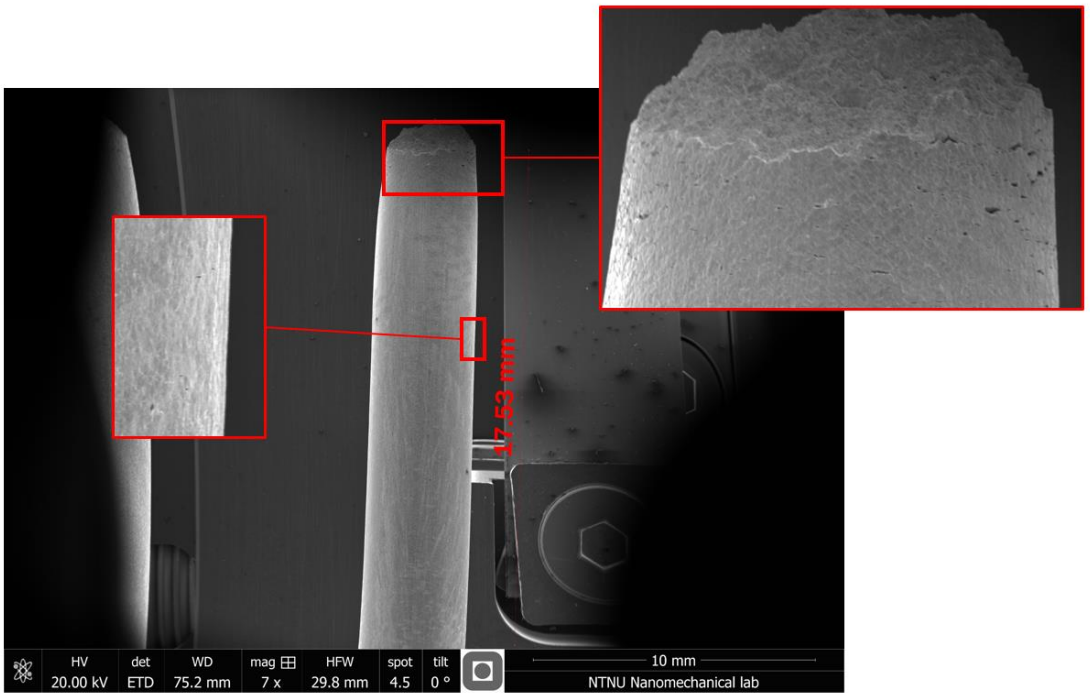

Figure 74 Secondary cracks in 1 Ni H2. The lowest highlighted area marks the lowest point where cracks were observed.

Figure 75 shows secondary cracks in the 1 Ni H4 test.

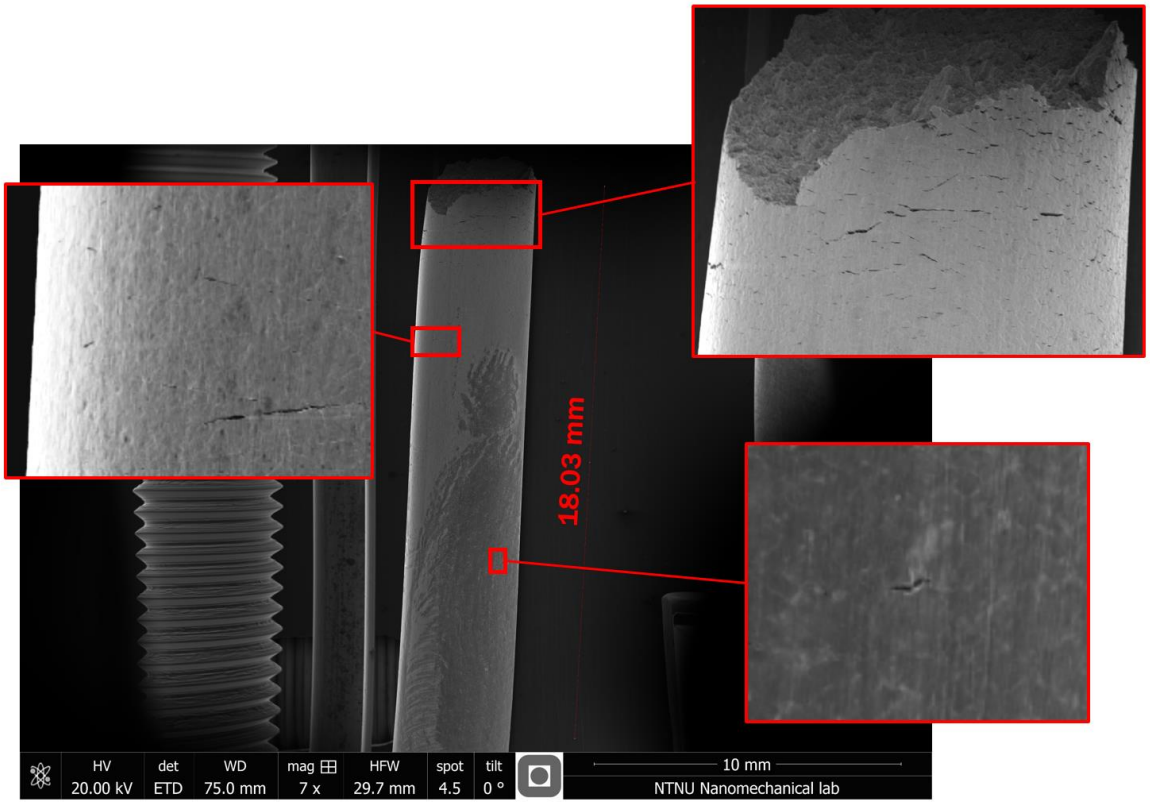

Figure 75 Secondary cracks in 1 Ni H4. The lowest highlighted area marks the lowest point where secondary cracks were found.

2 Ni

In the air tests, ductile features were found in 2 Ni, as shown in *Figure 76*.

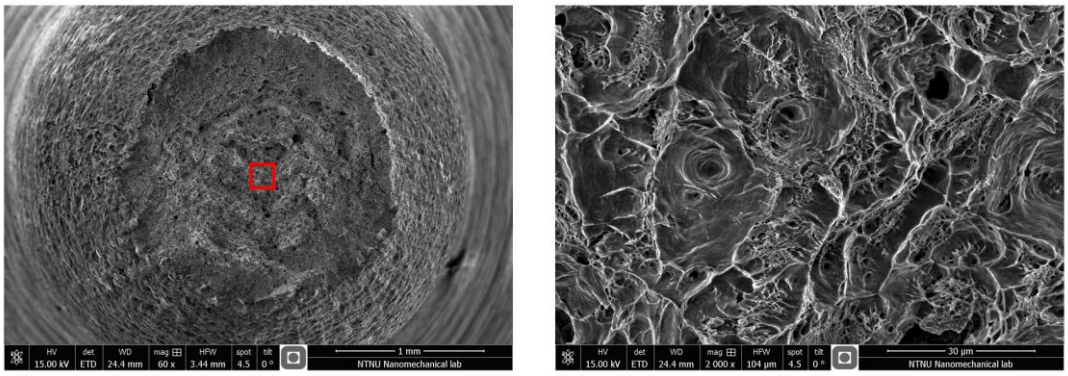

Figure 76 (a) 2 Ni Air at 60X (b) Close-up at 2000X of marked region in (a).

No secondary cracks were observed in the side views, as shown in *Figure 77*.

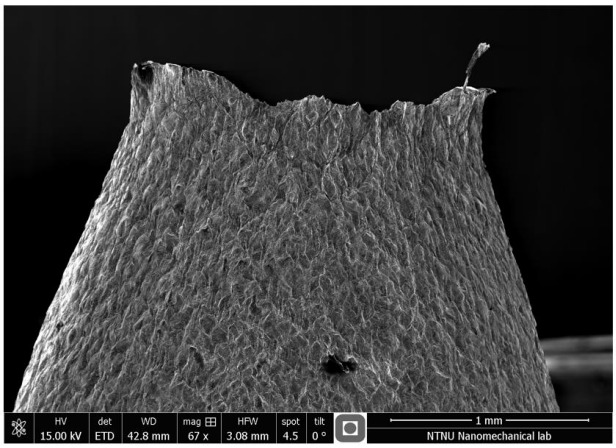

Figure 77 Side view at 67X of 2 Ni Air.

In test series H1 and H2, mixed ductile and brittle features were observed, as shown in *Figure 78*.

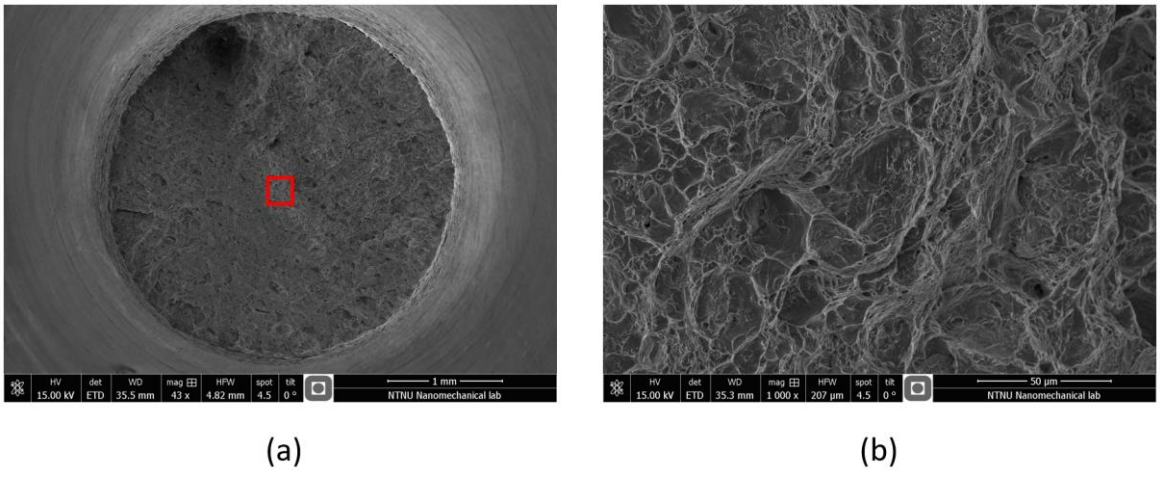

Figure 78 (a) 2 Ni H2 at 43X (b) Close-up of region in (a) at 1000X

Increasingly brittle features were found in test series H3 and H4, as shown in *Figure 79*.

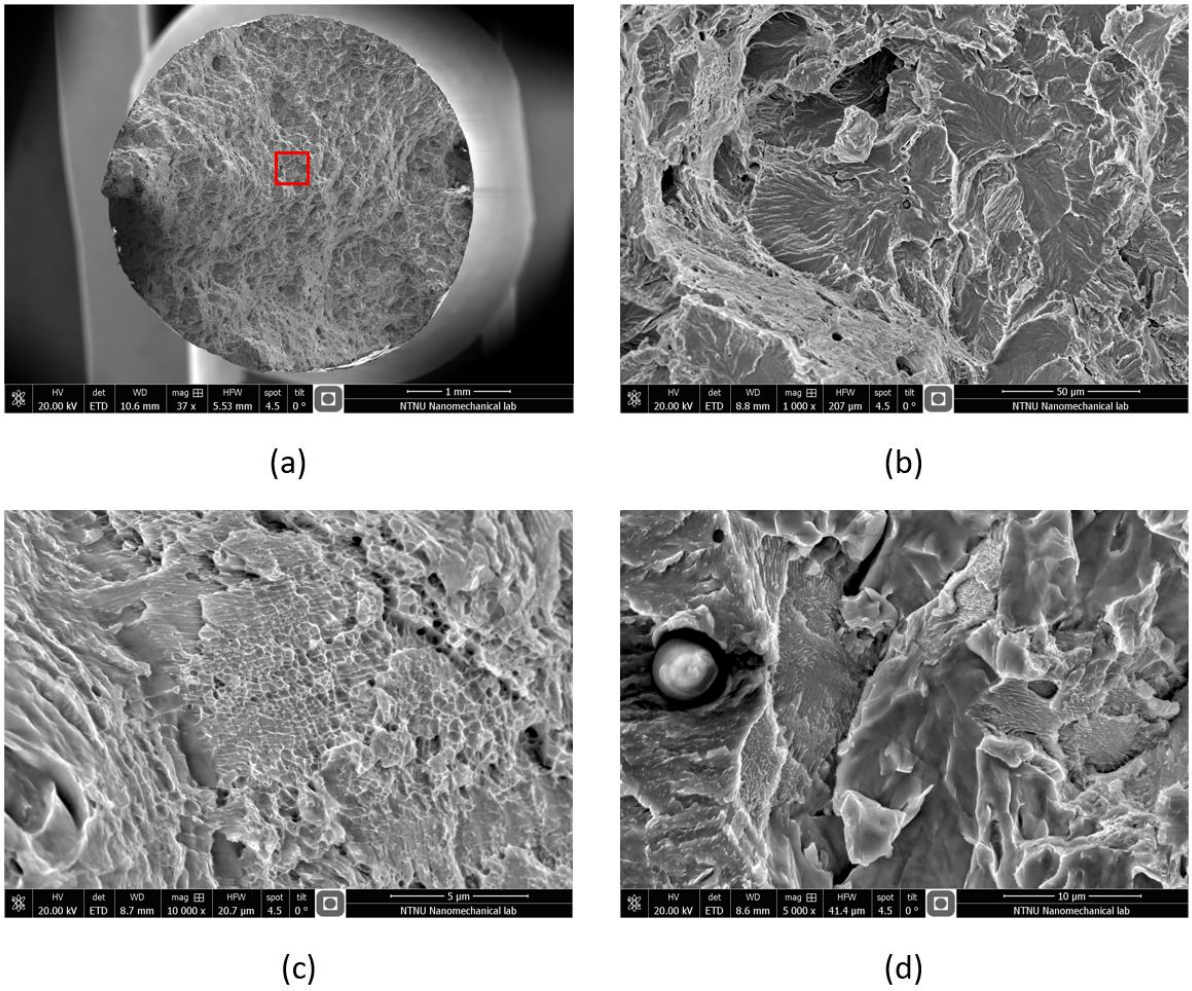

Figure 79 (a) 2 Ni H3 at 37X (b) Close-up of area marked in (a) at 1000X (c) Very shallow dimples at 10000X (d) Inclusion and pearlite grains seen at 5000X

Figure 80 shows secondary cracks along the 2 Ni H2 test. Cracks were observed beneath the area of fracture, and only at a small distance below this point.

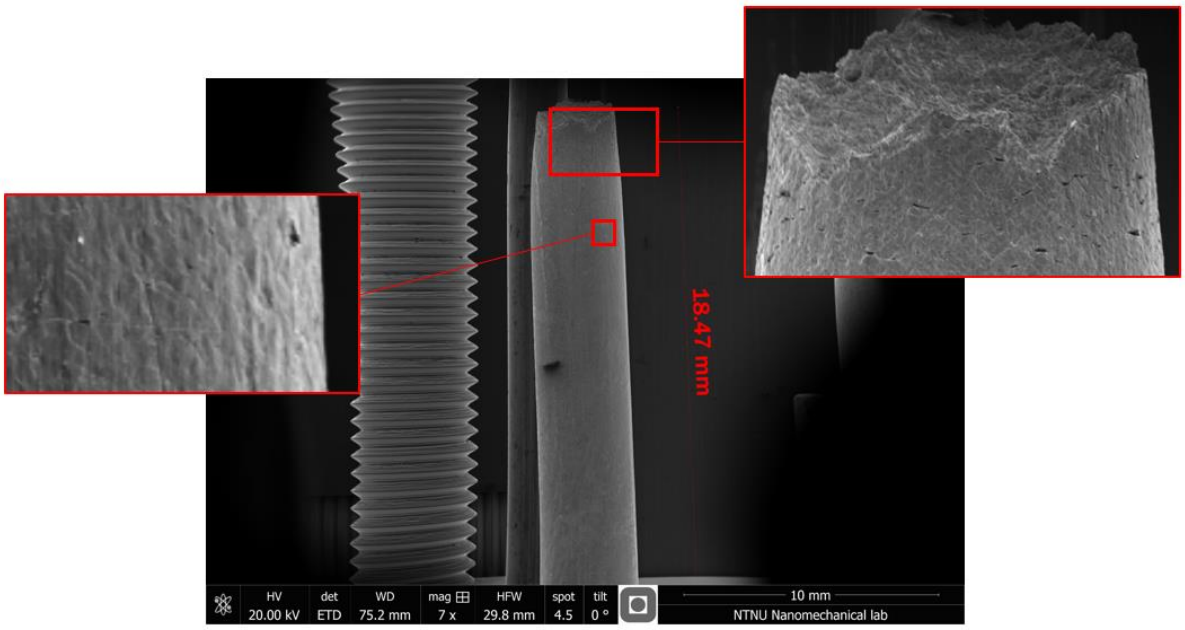

Figure 80 Secondary cracks of 2 Ni H2. The lowest highlighted area marks the lowest point where secondary cracks were found.

Figure 81 shows secondary cracking of the 2 Ni H4 test. Smaller cracks were observed down the gauge length.

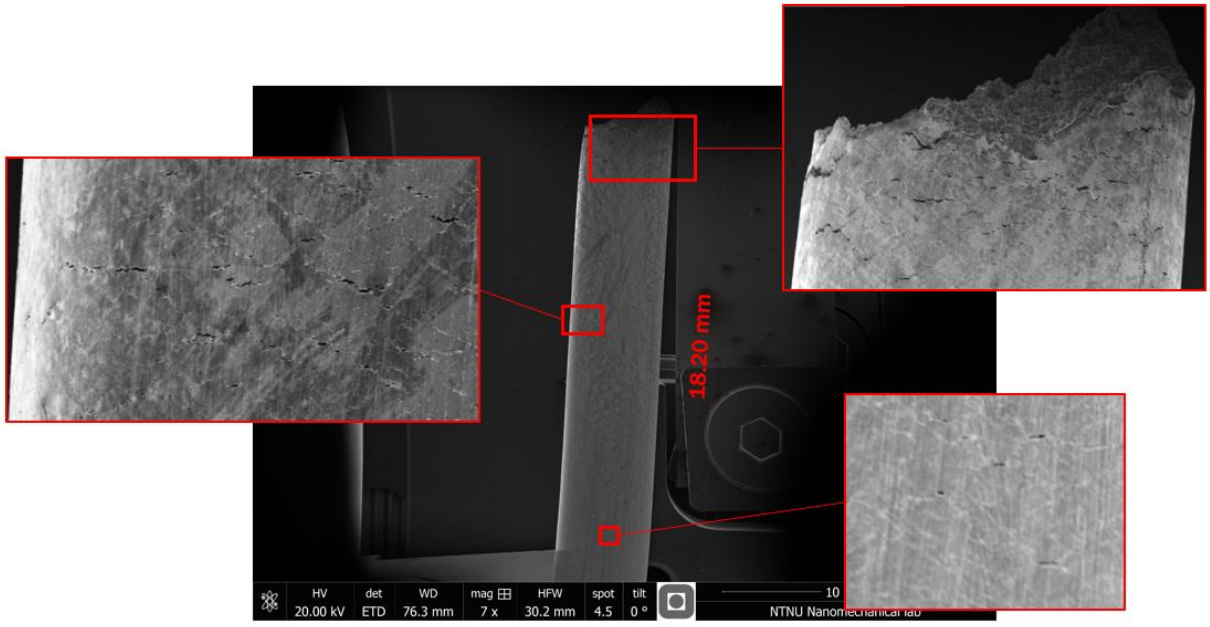

Figure 81 Secondary cracks in 2 Ni H4. The lowest highlighted area marks the lowest point where secondary cracks were found.

3 Ni

In the 3 Ni Air test, only ductile features were observed, as shown in *Figure 82*. As can be seen in *Figure 82 (b)*, a lot of circular inclusions were observed inside voids in dimpled areas.

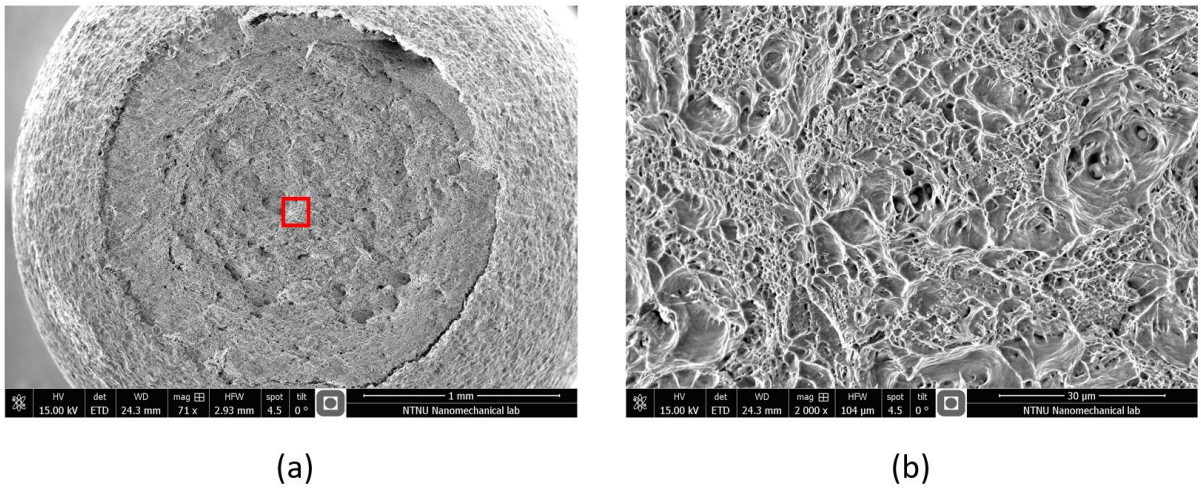

Figure 82 (a) Fracture surface at 71X (b) Close-up of marked area at 2000X

Figure 83 shows a side view of the 3 Ni Air test. This was the only test in air where a secondary crack was observed.

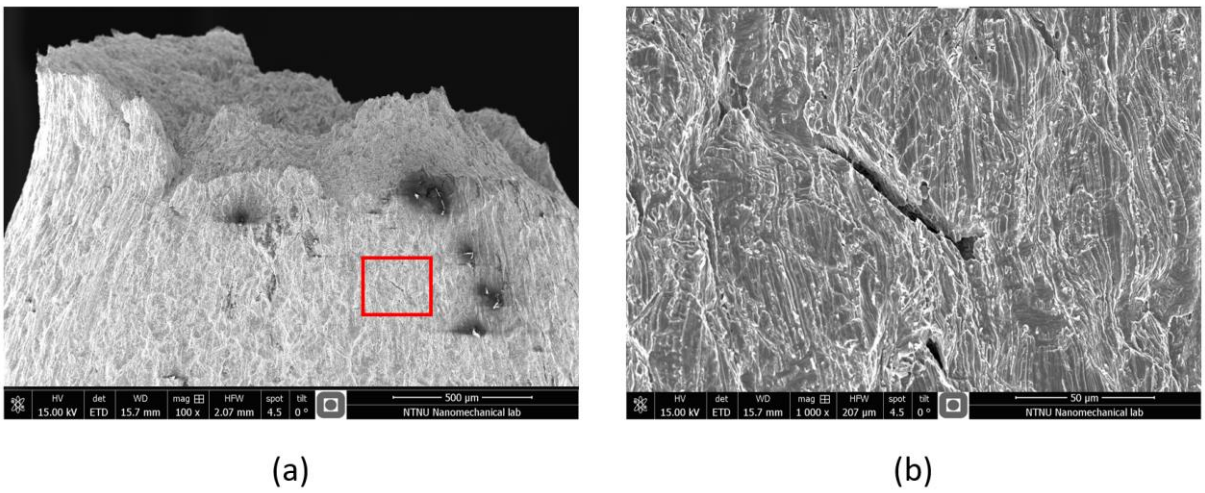

Figure 83 (a) 3 Ni Air at 100X (b) Close-up of marked region in (a).

In the H1 and H2 tests, mixed ductile and brittle features were observed, much like the other samples in these series. However, there were several cracks in the surface. An example of this is shown in *Figure 84*.

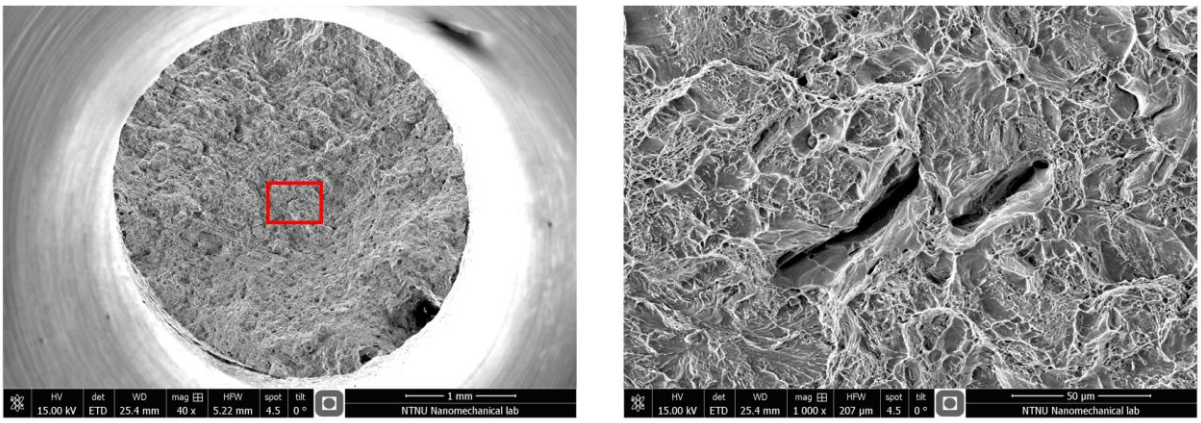

Figure 84 (a) 3 Ni H2 at 40X (b) Close-up at 1000X of marked area in (a)

Features of 3 Ni H3 are shown in *Figure 85*. In these tests, there were a lot of heavily striated transgranular cleavage planes, as shown in *Figure 85 (c)*. Several sites of cracking in the surface were observed, as shown in *Figure 85 (d)*. No pearlite grains were found in the surfaces of the H3 and H4 tests.

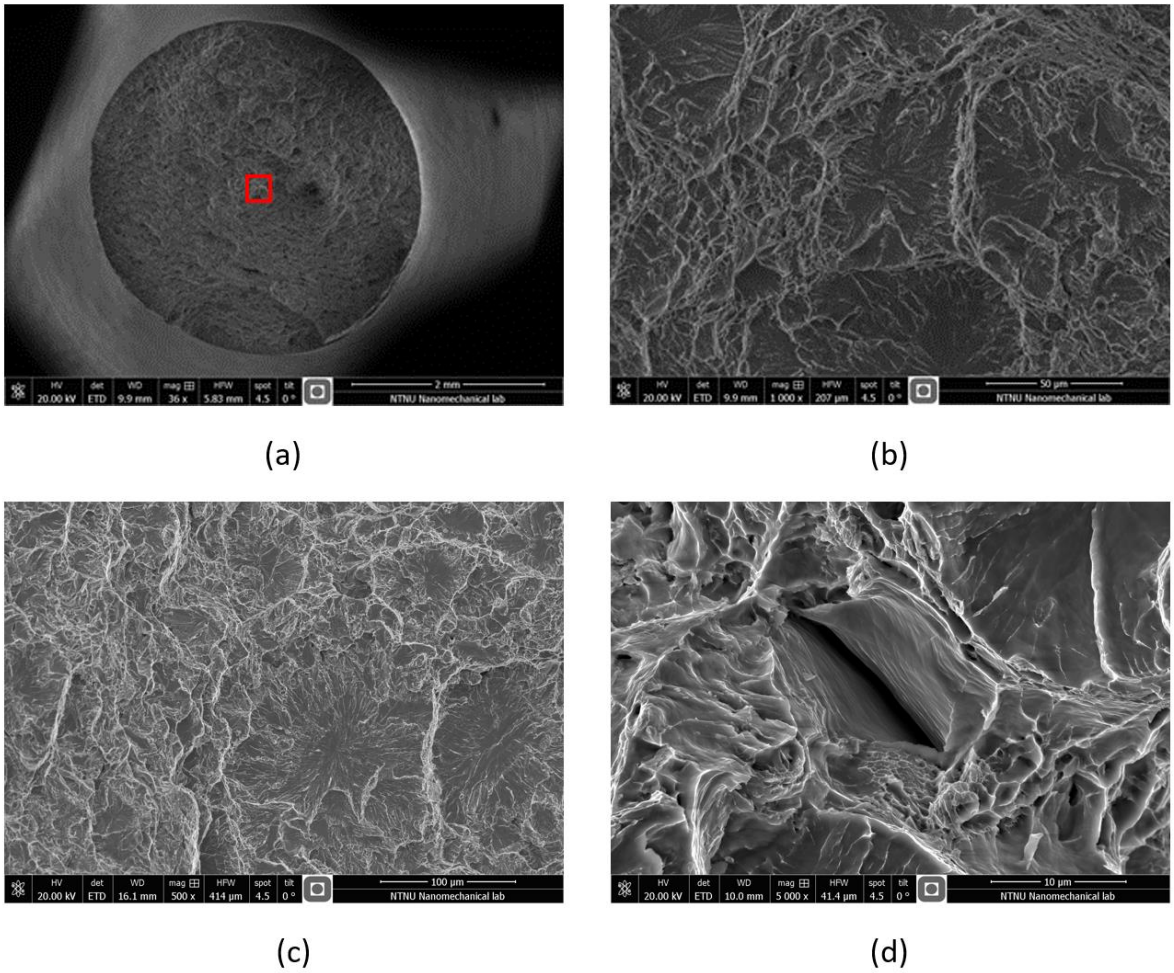

Figure 85 (a) 3 Ni H3 at 36X (b) Close-up of marked region in (a) at 1000X. (c) Heavily striated cleavage planes in 3 Ni H4 (d) Decohesion in surface of 3 Ni H4, surrounded by dimples.

In the H1 and H2 tests, comparatively few secondary cracks were observed. A picture of this is shown in *Figure 86*.

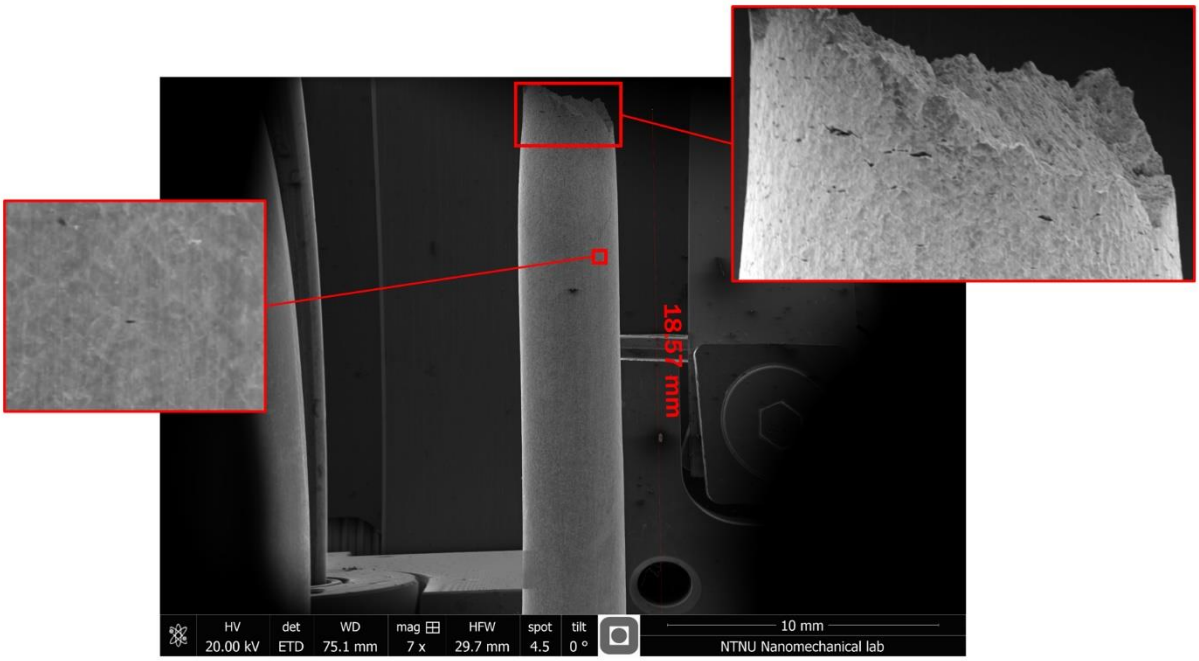

Figure 86 Secondary cracks of 3 Ni H2. The lowest highlighted area marks the lowest point where secondary cracks were found.

Similarly, there were also few secondary cracks in the 3 Ni H3 and H4 tests, as shown in *Figure 87*.

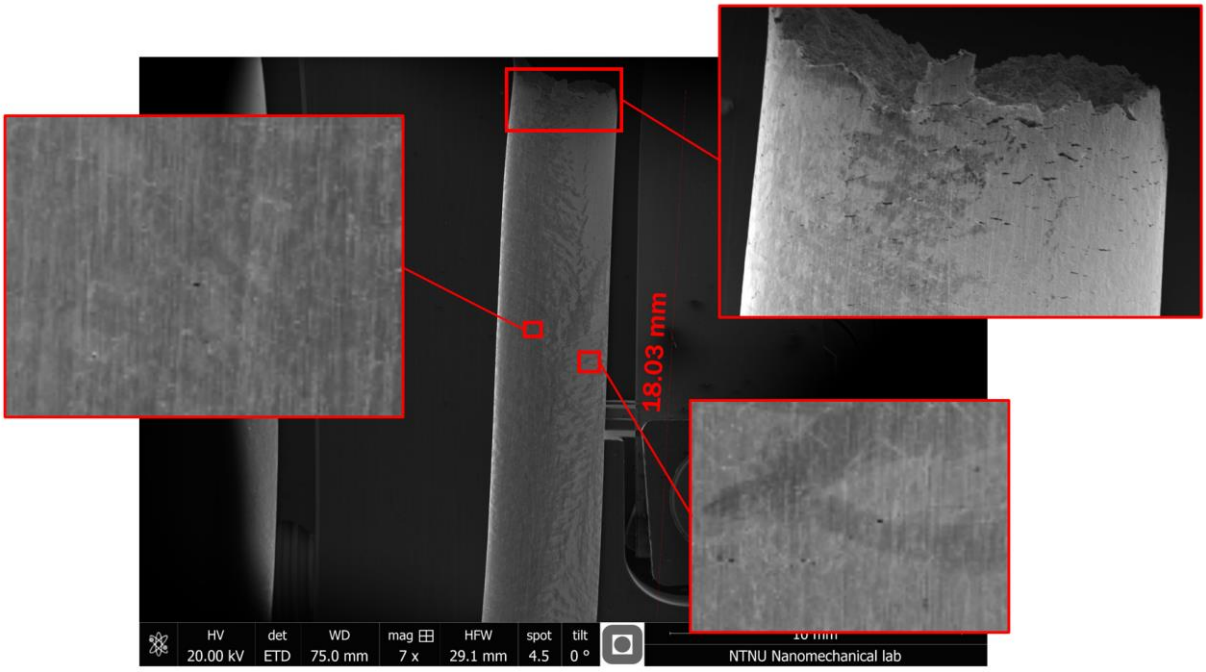

Figure 87 Secondary cracks in 3 Ni H4. The lowest point marks the lowest point where secondary cracks were found.

The fractographic features of both the 0 Ni and 3 Ni IRT tests were remarkably similar to their respective tests in air, and are thus not included here.

Severity of Cracks

To show the differences in the severity of cracks, side-by-side comparisons of the most severe cracks that were found are shown in *Figures 88* and *89*. *Figure 88* shows the most severe cracks that were observed during test series H1 and H2, and *Figure 89* the most severe cracks that were found during test series H3 and H4.

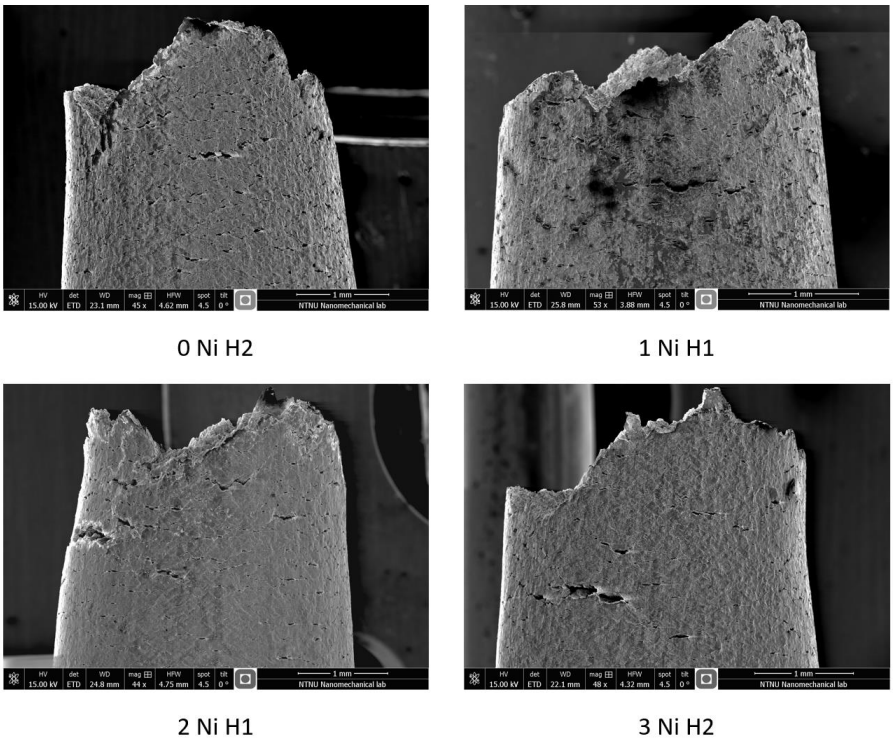

0 Ni H2 | 1 Ni H1

2 Ni H1 | 3 Ni H2

Figure 88 Most severe cracks observed for each alloy in test series H1 and H2.

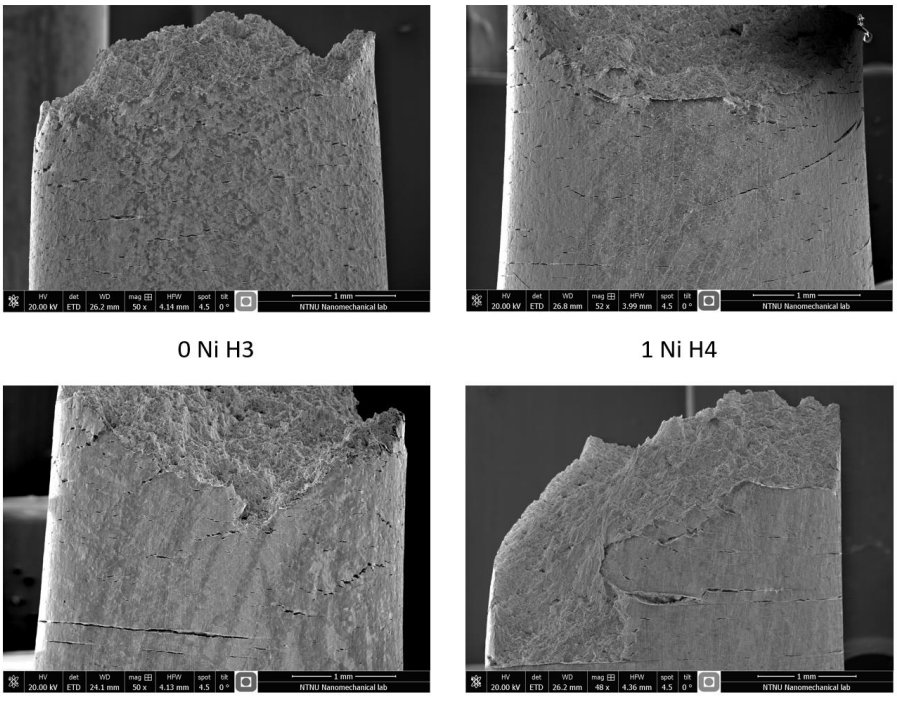

0 Ni H3 | 1 Ni H4

2 Ni H3 | 3 Ni H3

Figure 89 Most severe cracks observed for each alloy in test series H3 and H4.

5. Discussion

5.1 Material Characterization

The microstructures were characterized by their overall appearances, average grain sizes, pearlite fractions, and interlamellar spacings of pearlite. All the methods used were based on manual work and analysis, which introduced the factor of human error. Consequently, the results may be subject to errors from bias, performance, and skill level.

Due to deviations and randomness in the microstructures, it is unlikely to single out an area that is fully representative of the whole, unless an impracticably large sample size were taken. To counteract the influence of human bias when taking microstructure images, the regions that were taken pictures of were selected at random. Due to the grinding and electropolishing, though, selecting a random area would occasionally result in landing, as it were, in an area that was badly polished, contaminated, or had markings of the grinding process. As such, a certain amount of human bias was necessary when selecting areas to take pictures of.

Estimation of the average grain sizes by the intercept method is largely dependent on the person who performs the analysis; some may count an intersection at points where others do not. However, the general trends that were found should still be the same if several different people were to perform such an analysis, despite differences in the exact values. The average grain sizes for 0 Ni, 1 Ni, 2 Ni, and 3 Ni were 18.2, 13.5, 17.5, and 15.5 µm, respectively. When considering the heat treatments that were used, these results seem reasonable: 0 Ni and 1 Ni were both cooled at the same rate, and the differences in Ni-content caused a slower carbon diffusion rate, thus refining the grain size. 2 Ni and 3 Ni were also both cooled at the same rate, which was slower than for the other alloys. The difference in Ni-content caused a refinement of the grain size of 3 Ni.

Both the methods used to evaluate the pearlite fractions were somewhat imprecise. In addition, as mentioned above, the images of the microstructures that were used may not have been fully representative of the material. To counteract this, the images used were taken at low magnifications, to have them show a sufficiently large area of the microstructure. Thus, using the manual method, it was infeasible to cut out all the pearlite grains of the printed image, and some of the very smallest ones had to be neglected. Using the image editing software, the ferrite grains were filtered out by colour alone. This caused some of the visible ferrite inside the pearlite grains to also be filtered out. As such, both the methods used for evaluating the pearlite fractions are believed to have yielded results that were smaller than the actual pearlite fractions. The results of the manual method were 21.6%, 22.5%, 25.6%, and 29.3% pearlite for 0 Ni, 1 Ni, 2 Ni, and 3 Ni, respectively. The results of the image editing method were 18.5%, 19.6%, 23.0%, and 25.9% pearlite for 0 Ni, 1 Ni, 2 Ni, and 3 Ni, respectively. These results are higher than what would be expected when looking at the effect of Ni on the eutectoid composition, especially for 2 Ni and 3 Ni. This is most likely due to a synergistic effect of the Manganese (1.3 wt%) and Silicon (0.24%) that were also present in the alloys.

The interlamellar spacings of pearlite were determined by manually counting intersections between cementite lamellae in pearlite with a circular grid. To counteract the influence of bias, the pearlite grains were randomly selected, and a total of 15 images were used for each alloy. Some of the cementite lamellae were discontinuous and distorted, though, which caused some difficulties in counting. The average interlamellar spacings for 0 Ni, 1 Ni, 2 Ni, and 3 Ni were 351.4, 316.2, 323.9, and 271.9 nm, respectively. These results are also reasonable when considering the heat treatments that were used, and the trend is like that of the average grain sizes, in that the alloys with the same cooling rates see a decrease in interlamellar spacing of pearlite when the Ni-content increases. Notably, though, a larger decrease is seen between 2 Ni and 3 Ni than 0 Ni and 1 Ni.

5.2 Polarization Curves

In the polarization curves, seen in *Figure 56*, there are some unexpected and erratic turns of the curve, such as the zigzagging patterns that are formed in the cathodic region. These may be caused by ambient noise. The 0 Ni curve flattens out unexpectedly in the anodic region and suddenly shoots up again. This may be explained by a build-up of corrosion products.

Otherwise, the polarization curves are consistent with what one might expect, with 3 Ni being more noble than 0 Ni. Importantly, this makes the hydrogen evolution reaction happen faster on 3 Ni: it was found that at a potential of -1050 mV, the corrosion current densities were $0.30\ {}^{mA}/_{cm^2}$ and $0.38\ {}^{mA}/_{cm^2}$ for 0 Ni and 3 Ni, respectively.

For the potentiostatic hydrogen charging, this meant that a larger amount of hydrogen may have been present on the surfaces of the alloys with higher contents of Ni. This was the primary reason galvanostatic hydrogen charging was chosen for the two last test series (H3 and H4).

5.3 Slow Strain Rate Testing

Air Tests

When looking at the baseline curves and properties in air, there are some significant differences between the alloys. All tests were believed to be strengthened somewhat by Ni in solid solution in ferrite. Theory presented in chapter 2.1.3 is used to consider the differences in strength.

0 Ni has a yield strength of 250.7 MPa, a tensile strength of 398.4 MPa, and a plastic elongation of 0.3148.

1 Ni has a yield strength of 328.7 MPa, a tensile strength of 454.2 MPa, and a plastic elongation of 0.3361. The yield strength increase is mainly due to the refinement of the grain sizes. The increase in tensile strength is mainly due to the slightly higher pearlite fraction, as well as the smaller interlamellar spacing of pearlite. The change in ductility is due to the grain sizes being smaller.

2 Ni has a yield strength of 312.8 MPa, a tensile strength of 490.0 MPa, and a plastic elongation of 0.3008. The increase in yield strength is lower than 1 Ni, but still higher than what would be expected when judging by the grain sizes alone. Here the yield strength may be explained by the larger increase in pearlite content, and possibly due to acicular structures in the microstructure. The tensile strength is 100 MPa higher than for 0 Ni, and this is most likely due to the increased pearlite fraction, as well as the smaller interlamellar spacing. The decrease in ductility is mainly due to the increased pearlite fraction, but may also be somewhat due to the slightly smaller interlamellar spacing of pearlite.

3 Ni has a yield strength of 328 MPa, a tensile strength of 536.4 MPa, and a plastic elongation of 0.2667. Here the yield strength is the same as for 1 Ni, despite 3 Ni having coarser grains. This may be explained by the increased pearlite fraction of 3 Ni, and possibly also due to acicular structures. The tensile strength may be explained by the increased pearlite fraction and decreased interlamellar spacings. The decreased ductility is most likely due to the increased pearlite fraction, as well as the decreased interlamellar spacing of pearlite. Another observation on 3 Ni is that it is the only alloy that does not have the yield point elongation phenomenon.

H1 and H2 tests

For all the tests, the strengths were consistently seen to be higher in the hydrogen-containing environments than they were in air. *Table 18* gives the ratios of strengths in hydrogen when compared to the baseline tests in air. Mean values of both H1 and H2 tests are used.

Table 18 Average strength values were taken of both H1 and H2 tests for all alloys. The ratios are defined as dividing the property obtained in hydrogen by the property obtained in the respective air test, and multiplying by 100

Test	Upper YS Ratio [%]	Lower YS Ratio [%]	UTS Ratio [%]
0 Ni H1 & H2	112.0	103.2	102.5
1 Ni H1 & H2	102.8	102.2	102.2
2 Ni H1 & H2	101.2	100.2	101.0
3 Ni H1 & H2	101.4	0.0	101.2

In the H1 and H2 test series, higher yield strengths than in air were observed for all alloys, as seen in *Table 18*. The effect was especially pronounced for 0 Ni, where both tests saw an increase of 30 MPa. This may be related to the fact that 0 Ni had the highest ferrite fraction, which was documented by Shved et al. [31] to give the highest increase in strength when different carbon contents were tested. This is somewhat supported when looking at the other alloys, because the strengthening effect gets less pronounced as the Ni-content is increased, but 3 Ni does have a slightly higher strength increase than 2 Ni

Comparing the curves of the H1 and H2 tests for each alloy, the deviations between the strains at failure becomes larger for increasing Ni-contents. Looking at the measurements of the current on the counter electrode, there does not appear to be any correlation that would explain the deviations. Namely, 0 Ni, which had the smallest deviation between the two curves, had differences in the measured current that were larger than those of the 3 Ni tests, where the deviations were largest. The current on the counter electrode may have been affected by the fluid level in the chamber, or by impurities. There appears to be a small correlation between the ambient temperature and the current on the counter electrode, although this is very minor.

Table 19 Average values of ductility parameters for H1 and H2 tests.

Tests	Plastic elongation Ratio [%]	RA ratio [%]
0 Ni H1 & H2	90.4	47.4
1 Ni H1 & H2	69.9	43.0
2 Ni H1 & H2	66.7	44.2
3 Ni H1 & H2	77.2	42.4

Otherwise, comparing the average ductility parameters of the alloys in *Table 19* shows that 0 Ni was most resistant to hydrogen embrittlement. However, the ductility parameters of all Ni-containing alloys were largely similar, and it cannot be said that any dramatic effects were found from exceeding 1 wt% Ni, as ISO 15156:2 [1] states. An important difference, though, is that these tests

were conducted in a relatively mild environment, especially when compared to a sour oil & gas environment, and there may have been subtle differences that were too small to accurately measure. The 3 Ni test has the best average HE resistance of the Ni-containing alloys, but a large deviation was observed between 3 Ni H1 and H2.

H3 and H4 tests

In these tests, the environment was considerably harsher: not only was the current increased from approximately 10 mA (in tests H1 and H2) to 550 mA (tests H3 and H4), but it was also directly on the test specimen. This was approximated as a current density of 15 mA/cm^2 (see Appendix B). When judging by the ductility parameters, the tests are all more embrittled than they were in the previous environment. The yield strengths are also different, in that the peak of the upper yield points are considerably lower for 0 Ni, 1 Ni and 2 Ni. These types of occurrences have been reported in early literature on hydrogen embrittlement [17].

Table 20 shows the ratio of strengths that were recorded in hydrogen compared to air.

Table 20 Average strength values were taken of both H3 and H4 tests for all alloys. The increase is defined as dividing the property obtained in hydrogen by the property obtained in the respective air test, and multiplying by 100

Tests	Upper YS Ratio [%]	Lower YS Ratio [%]	UTS Ratio [%]
0 Ni H3 & H4	101.1	112.4	105.5
1 Ni H3 & H4	93.7	107.1	103.3
2 Ni H3 & H4	100.3	104.6	103.7
3 Ni H3 & H4	109.8	0.0	105.9

As seen in *Table 20,* the upper yield strengths do not appear to follow any trend. 3 Ni has the highest increase in yield strength by far. This may be somewhat related the acicular structures that were observed in the microstructure. These were also observed in 2 Ni as well, although to a smaller degree, and this may explain why the upper YS is comparatively higher than 1 Ni. Increases of the lower yield points follow the same trend as was seen in the H1 and H2 tests, in that the alloys with higher pearlite fractions see a smaller increase in strength. The ultimate tensile strengths ratios decrease from 0 to 1 Ni, which may be related to the pearlite fraction. Again, the UTS is comparatively higher for 2 Ni and 3 Ni despite the higher pearlite fraction, and this may also be related to the acicular structures, and possibly also the decreased interlamellar spacings of pearlite.

Table 21 Table of average ductility parameters for H3 and H4 tests.

Tests	Plastic elongation Ratio [%]	RA ratio [%]
0 Ni H3 & H4	56.6	26.9
1 Ni H3 & H4	49.7	23.9
2 Ni H3 & H4	47.1	21.7
3 Ni H3 & H4	36.1	18.9

As can be seen in *Table 21*, all the alloys with increasing Ni-contents are increasingly susceptible to hydrogen embrittlement.

For 1 Ni, the HE susceptibility would be expected to decrease, since the grain sizes are lower, and the pearlite fraction is slightly higher, which was found by Chan et al. to decrease the susceptibility [34]. However, the interlamellar spacing of pearlite is finer, which, judging by the results of Snape [35] was seen to increase the susceptibility to SSC. This was done by evaluating changes in threshold stress, though, and the results may not be directly applicable for this situation. Furthermore, no measurements of interlamellar spacings were given. In the mentioned study by Snape, the steel referred to as Plain Carbon, as seen in *Table 7*, was strengthened from a coarse pearlite structure with a yield strength of 34900 psi (240 MPa) to a finer structure with a yield strength of 54500 (376 MPa), without any changes in SSC susceptibility. The strength increase means that the reduction of the interlamellar spacing in Snape's study must have been significantly more pronounced than that from the 0 Ni to 1 Ni alloys studied in this thesis. In addition, the charging conditions in Snape's study were far more aggressive. As such, the interlamellar spacing is not considered to have played a very significant role in the embrittlement of 1 Ni.

A factor that may have played a part, is the strength difference between 0 Ni and 1 Ni. The yield strength of 1 Ni was almost 80 MPa higher than 0 Ni. Hardie et al. [33] found only small differences in the HE susceptibilities of banded ferrite/pearlite steels where the both yield strengths and tensile strengths were up to 300 MPa higher, when the testing was done at a low hydrogen fugacity, and larger differences when the hydrogen fugacity was higher. The high hydrogen fugacity that was first observed to increase embrittlement was when charging was done at a current density of 66 mA/cm^2, in a solution that contained 0.5 M H_2S and was poisoned with 5 g/l KH2AsO4. In comparison, the test environment used for the H3 and H4 tests were very mild, and the differences in HE susceptibility cannot thus be attributed to the strength increase.

For 2 Ni, the change in the pearlite fraction would be expected to increase the HE resistance. Also, the grain sizes, and interlamellar spacings of pearlite, are similar to those of 0 Ni. In addition, if yield strength were to be considered a factor, the yield strength is lower in air than it was for 1 Ni. Still, the HE susceptibility of 2 Ni is higher than both 0 Ni and 1 Ni. One possible explanation may be the observation of several needle-like structures in the microstructure, which was also observed by Koval [39] who also studied the embrittlement of ferrite-pearlite steels with increasing Ni-contents. In other studies, though, a structure that is dominated by acicular ferrite have been seen to be more resistant to HE than pearlite [40]. The case for 2 Ni may have been that the small amounts of brittle acicular structures within the microstructure caused a stress concentration that facilitated cracking. A very small amount of acicular structures were observed, though, and it is deemed unlikely that these played a significant role.

3 Ni was the most susceptible to HE. The pearlite fraction was estimated to be markedly higher than the other materials, which would have been expected to increase the HE resistance. The yield strength was the same as for 1 Ni in air. One significant difference though, was the interlamellar spacing of pearlite, which was by far the smallest for 3 Ni. Also, more observations of blunt and sharp needle-like grains were observed in the microstructure than 2 Ni. Still, though, as in 2 Ni, these were not very common.

IRT tests

The 0 Ni IRT test saw an increase in ductility, and a small increase in tensile strength, whereas the upper yield point decreased, and the lower yield point stayed mostly the same. This type of behaviour in ferrite-pearlite steels has been reported by Singh et al. [32], and is believed to indicate

that the hydrogen content in the steel is lower than the hydrogen solubility in the ferrite matrix. As such, only a small amount of irreversible trapping is believed to have occurred in the 0 Ni IRT test.

The 3 Ni IRT test had a yield strength that was higher than the H1 and H2 tests, an ultimate tensile strength that was the same as the H1 and H2 tests, and ductility parameter ratios that were lower than they were in air. Judging by the study by Singh. et al [32], this is believed to indicate that the hydrogen content in 3 Ni IRT was higher than the solubility in ferrite, and followingly that more irreversible trapping occurred in this sample than in 0 Ni. It is hard to tell if the irreversible trapping was a direct consequence of the Ni-content, though, as the increase in pearlite fraction and decrease in grain sizes are also known to increase trapping, as reported by Chan et al. [34].

5.4 Scanning Electron Microscopy

The fracture surfaces that were studied using SEM were found to be very similar in morphology. Despite significant time and effort, no intergranular cleavage fracture was found to occur. Although intergranular cracking is unusual in low-strength steels, increasing Ni-content can increase the likelihood of this because Ni tends to segregate metalloid elements and impurities to grain boundaries, as mentioned in chapter 2.3. As such, the absence of intergranular cleavage can to some extent be used as an indirect form of evidence that impurity levels and segregation of metalloid elements were not a major factor in the embrittlement of these steels.

Small circular inclusions were found in all alloys at high magnifications. Typically, a couple of them would be observed close to each other. These were later characterized by Energy Dispersive Spectroscopy (EDS), which revealed that they consisted of the elements Mn, Si, Al, O and S. It should be noted, though, that there did not appear to be any differences in the amounts that were observed in the different alloys, and they are thus not believed to have impacted the results.

As can be seen in Chapter 4.4, several sightings of pearlite grains were made when examining the fracture surfaces of the samples. It was speculated that these may have been related to hydrogen-induced cracking (HIC) and blistering, but no evidence of blisters was found in the samples. Also, blistering would typically not be a factor unless the charging current density were much higher and/or the electrolyte were poisoned with compounds that inhibit hydrogen evolution, such as H_2S and As_2O_3. As an example of this, in the study by Singh et al. [32] that is presented in Chapter 2.3.2, a charging current of 50 mA/cm^2 was used in a 0.1 N H_2SO_4-solution that was poisoned with 5 mg/l As_2O_3, and blistering was first seen to take place after charging for 16 hours.

An observation that may or may not be of importance regarding the pearlite grains that were observed, though, is that these pearlite grains were observed in all samples except for 3 Ni.

The observation of areas of very shallow dimples close to brittle features was noted. In 2 Ni and 3 Ni, there was a higher number of large cracks in the surface, and these were typically surrounded by very small dimples.

Secondary cracks were seen in all the hydrogenated samples; more so for the H3 and H4 tests, where a higher charging current was used. For the H1 and H2 tests, all the cracks where contained within a small area, and were not seen down the entire gauge length. In the H3 and H4 tests, a larger portion of cracks were seen down the gauge length. When considering the number of secondary cracks, 0 Ni was seen to have the most; very small cracks were observed along a larger portion of the gauge length than for the Ni-containing alloys. All the Ni-containing steels were seen to have fewer smaller cracks down the length of the gauge area. Amongst the fewer cracks that were observed in the Ni-containing steels, though, there was usually one or several continuous cracks that were more severe than any of those found in 0 Ni.

5.5 Overall Evaluation of Hydrogen Embrittlement Susceptibility

The results of the experimental work revealed that the tested ferrite-pearlite steels with higher contents of Ni were increasingly susceptible to hydrogen embrittlement. Visual examination of the fracture surfaces by use of SEM revealed similar morphologies, but the secondary cracks in the Ni-containing steels were more severe.

When comparing the microstructural features alone, the changes in hydrogen embrittlement susceptibility were deemed to be larger than what would be expected when comparisons were made with other hydrogen embrittlement studies. The exact influences of the interlamellar spacings of pearlite, as well as the acicular structures, were challenging to ascertain, given the limited amount of comparable literature that was found regarding these. However, when 0 Ni and 2 Ni were compared with respect to the studied microstructural features, the average grain sizes and interlamellar spacings of pearlite were found to be similar. The pearlite fraction of 2 Ni was markedly higher than that of 0 Ni. Only a very small amount of acicular structures was found in 2 Ni, and it is deemed unlikely that this would be enough to bring forth the changes in hydrogen embrittlement susceptibility that were found.

5.6 Suggestions for Further Work

Many of the effects that were believed to increase the hydrogen embrittlement of the Ni-containing alloys were related to changes in hardenability, such as the reduction of interlamellar spacing of pearlite, as well as the formation of acicular structures in the microstructure. Many of these results were challenging to quantify using the literature that was found. These factors could possibly be isolated by conducting similar studies where steels with other alloying elements that increase the hardenability, such as for instance Manganese, were tested. If the results were similar, the increase in embrittlement would be shown to be related to the hardenability increase rather than a property of Ni.

Many of the changes that were brought on by increasing the Ni-contents were related to carbon, such as the increase in pearlite fraction and the reduction in interlamellar spacing of pearlite. Using the literature that was found, the exact influences that these changes had on the hydrogen embrittlement susceptibility were challenging to accurately quantify. One possible solution to this might be to perform similar tests of decarburized steels that contained different amounts of Ni. This would, however, only be enough to study the effects of Ni on the ferrite phase. Possibly, if performing further testing of ferrite-pearlite steels, one could decrease the amount of carbon when increasing the amount of Ni, to attempt to keep the variables other than Ni-content constant.

Larger differences in the susceptibility to hydrogen embrittlement were seen as the hydrogen fugacity was increased. Further studies with higher charging currents, and possibly lower strain rates, should be performed to determine whether this trend increases.

6. Conclusion

Low alloy ferrite-pearlite steels with 0, 1, 2, and 3 wt% Ni were slow strain rate tested to evaluate the effects of exceeding the 1 wt% Ni restriction in ISO 15156:2. The materials were characterized by their overall microstructures, average grain sizes, relative fractions of pearlite, and the interlamellar spacings of pearlite. One of each alloy was tested in an ambient environment, two of each alloy were tested in a 3.5 wt% NaCl-solution with potentiostatic hydrogen charging, and two of each alloy were tested in a 3.5 wt% NaCl-solution with galvanostatic hydrogen charging. The irreversible trapping behaviour of the 0 wt% Ni and 3 wt% Ni samples were evaluated by charging them with hydrogen and storing them in a desiccator for 11 days before slow strain rate testing them. The surfaces and side views of all the tested specimens were examined by use of scanning electron microscopy (SEM). The following was found:

- In the test series where potentiostatic hydrogen charging was used, the samples with 0 wt% Ni were least susceptible to hydrogen embrittlement. However, the samples with 1, 2 and 3 wt% were found to be only slightly more susceptible to hydrogen embrittlement, and no obvious differences were found between them.
- In the test series where galvanostatic hydrogen charging was used, a higher cathodic charging current was used as well. The alloy with 0 wt% Ni was least susceptible to hydrogen embrittlement, and the other samples were increasingly susceptible with increasing contents of Ni. The increase in susceptibility was deemed to be larger than what would be expected when considering the literature available on the isolated effects of the changes in the microstructural features that were studied.
- In the test series where the irreversible trapping behaviour was evaluated, the alloy with 3 wt% Ni was seen to cause more irreversible trapping of hydrogen than the alloy with 0 wt% Ni. However, it was unclear whether this was due to the increased pearlite fraction of the sample with 3 wt% Ni.
- For all alloys tested, the embrittling behaviour could be classified as a loss in tensile ductility. No differences were found in the fracture morphologies of the samples. In the Ni-free alloy, there were more secondary cracks along the gauge area. However, the cracks in the Ni-containing alloys were more severe.

7. References

1. ISO, *15156 - Petroleum and natural gas industries -- Materials for use in H2S-containing environments in oil and gas production*, in *Part 2: Cracking-resistant carbon and low-alloy steels, and the use of cast irons*. 2015.
2. Kappes, M., et al., *Sulfide stress cracking of nickel-containing low-alloy steels.* Corrosion Reviews, 2014. **32**(3-4): p. 101-128.
3. William D. Callister Jr. , D.G.R., *Materials Science and Engineering - An Introduction*. Vol. 9. 2013: Wiley.
4. Dieter, G.E., *ASM Handbook, Volume 20: Materials Selection and Design. Vol. 20*. 1997, C R C Press LLC.
5. ASM, *ASM Handbook, Volume 1: Properties and Selection: Irons, Steels, and High-Performance Alloys. Vol. 1*. 1990.
6. Smith, W.F. and J. Hashemi, *Foundations of materials science and engineering*. 4th ed. ed. McGraw-Hill series in materials science. 2006, Boston: McGraw-Hill.
7. ASM, *ASM Handbook, Volume 11: Failure Analysis and Prevention*. 2002.
8. Cramer, S.D. and B.S. Covino, *ASM Handbook, Volume 13A: Corrosion: Fundamentals, Testing, and Protection. Vol. 13*. 2003, A S M International.
9. Gray, H., *Testing for Hydrogen Environment Embrittlement: Experimental Variables*, in *Hydrogen Embrittlement Testing*. 1974, ASTM International. p. 133-155.
10. ISO, *15156 - Petroleum and natural gas industries — Materials for use in H2S-containing environments in oil and gas production*, in *Part 1: General principles for selection of cracking-resistant materials*. 2015.
11. Phull, B. and B. Phull, *Evaluating hydrogen embrittlement*. Vol. 13A. 2003. 617-624.
12. Nisancioglu, K., *Corrosion Basics and Engineering*.
13. Cramer, S.D. and B.S. Covino, *ASM Handbook, Volume 13C: Corrosion: Environments and Industries. Vol. 13*. 2006, A S M International.
14. Pickering, H.W., E. Pennsylvania State Univ University Park Coll Of, and S. Mineral, *A Review of the Mechanism and Kinetics of Electrochemical Hydrogen Entry and Degradation of Metallic Systems*. 1990.
15. Crank, J., *The Mathematics of Diffusion*. Vol. Second edition. 1975, Oxford: Clarendon Press.
16. Nagumo, M., *Fundamentals of Hydrogen Embrittlement*. 2016: Springer Singapore. *239*.
17. Oriani, R.A., Hirth, John P.; Smialowski, Michael, *Hydrogen Degradation of Ferrous Alloys*. 1985, Knovel: William Andrew Publishing/Noyes.
18. Lynch, S., *Hydrogen embrittlement phenomena and mechanisms*. 2012. p. 105.
19. NACE, *TM 0177 Laboratory Testing of Metals for Resistance to Sulfide Stress Cracking and Stress Corrosion Cracking in H_2S Environments*. 1996.
20. NACE, *Slow Strain Rate Test Method for Screening Corrosion-Resistant Alloys for Stress Corrosion Cracking in Sour Oilfield Service*. 2011.
21. ASTM, *G129 Standard Practice for Slow Strain Rate Testing to Evaluate the Susceptibility of Metallic Materials to Environmentally Assisted Cracking*. 2013.
22. Victor Kerlins, M.D.A.C., Austin Phillips, Metallurgical Consultant, *ASM Handbook, Volume 12: Fractography, Modes of Fracture*. 1987: ASM International.
23. Craig, B., *Review of nickel's role in sulfide stress cracking of low alloy steels.* Corrosion (Houston, TX, USA), 1988: p. 776-782.
24. Jarvis, A.R. and J.H. Bulloch, *The effect of nickel content on the environmental assisted cracking (EAC) behaviour of low alloy steels in sour environments—A review.* International Journal of Pressure Vessels and Piping, 1992. **49**(3): p. 271-307.
25. R. Treseder, T.S., *Factors in sulfide stress cracking of high strength steels.* Corrosion (Houston, TX, USA), 1968: p. 31-37.

26. Dunlop, A., *Stress corrosion cracking of low strength, low alloy nickel steels in sulfide environments.* Corrosion (Houston, TX, USA), 1978: p. 88-96.
27. Hideo Kobayashi, K.H., Hiroshi Kayakabe, Hajime Nakazawa, *Influence of Hydrogen on Fracture Toughness of High Strength Steels.* 1981.
28. Sieradzki, K., *On the embrittlement of steels by hydrogen sulfide.* Scripta Metallurgica, 1981. **15**(2): p. 171-176.
29. Minozaki, Y.Y.a.Y., *Sulfide Stress Cracking Resistance of Low-Alloy Nickel Steels.* NACE, 1986.
30. Hui, W., et al., *Effect of nickel on hydrogen embrittlement behavior of medium-carbon high strength steels.* Materials Science and Engineering: A, 2016. **674**: p. 615-625.
31. M. Shved, N.Y.Y., and L. M. Bilyi, *Effects of Hydrogen on the Strength and Fracture of Steel with Different Carbon Concentrations.* Translated from Fiziko- Khimicheskaya Mekhanika Materialov, Vol. 12, No. 5, pp. 14-16, September-October, 1976.
32. S. K. Singh, B.S., *Effect of Ferrite Grain Size on Tensile Behaviour of a Hydrogenated Low Alloy Steel.* ISIJ International, Vol 39, 1999: p. 371-379.
33. D. Hardie, E.A.C., A.H. Lopez, *Hydrogen embrittlement of high strength pipeline steels.* 2006.
34. S.L. I. Chan, J.A.C., *Effect of carbon content on hydrogen occlusivity and embrittlement of ferrite-pearlite steels.* 1986.
35. Snape, E., *Roles of Composition and Microstructure in Sulfide Cracking in Steel.* 1968.
36. Chan, S.L.I., *Hydrogen trapping ability of steels with different microstructures.* Journal of the Chinese Institute of Engineers, 1999. **22**(1): p. 43-53.
37. Demarez, A., A.G. Hock, and F.A. Meunier, *Diffusion of hydrogen in mild steel*. 1954. p. 369-369.
38. Devanathan, M.A.V. and Z. Stachurski, *The Adsorption and Diffusion of Electrolytic Hydrogen in Palladium.* Proceedings of the Royal Society of London. Series A, Mathematical and Physical Sciences (1934-1990), 1962. **270**(1340): p. 90-102.
39. Koval, V., L. Karvatskii, and R. Koval'chuk, *Influence of carbon, nickel, manganese, and vanadium on stress-corrosion cracking of steels in a medium containing hydrogen sulfide.* Soviet materials science : a transl. of Fiziko-khimicheskaya mekhanika materialov / Academy of Sciences of the Ukrainian SSR, 1979. **15**(2): p. 161-164.
40. Zhao, M.-C., et al., *Role of microstructure on sulfide stress cracking of oil and gas pipeline steels.* Metallurgical and Materials Transactions A, 2003. **34**(5): p. 1089-1096.
41. Hans Husby, A.B., Mariano Iannuzzi, Roy Johnsen, *Effect of nickel in solid solution on hydrogen transport kinetics in low alloy steels.* EUROCORR/16, paper no. 66667 (Montpellier, France: European Federation of Corrosion, September 11-15, 2016). 2016.
42. ISO, *17081 - Method of measurement of hydrogen permeation and determination of hydrogen uptake and transport in metals by an electrochemical technique*. 2014.
43. ASTM, *E122-12 Standard Test Methods for Determining Average Grain Size*. 2013.
44. Vander Voort, G.F. and A. Roósz, *Measurement of the interlamellar spacing of pearlite.* Metallography, 1984. **17**(1): p. 1-17.

Appendix A – Hydrogen diffusion

Figure 90 shows the solution to the hydrogen diffusion equation presented in *Equation 24*. The diffusion coefficient used is from the article by Husby et al. [41], who studied hydrogen diffusion in a glycerine/borax solution using samples of the same materials that were used for this thesis. The diffusion coefficient of 3 Ni in 15℃ was used, as it was the lowest diffusion rate that was found. By the solution in *Figure 90,* a time of 48 hours was deemed to be sufficient.

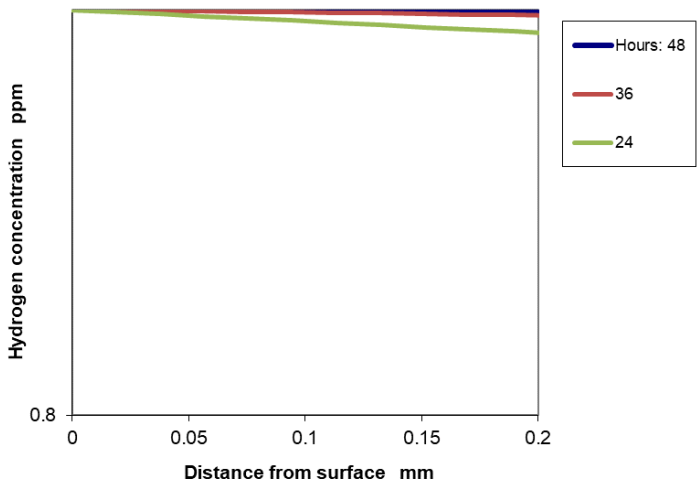

Figure 90 Hydrogen diffusion

Husby conducted further diffusion experiments using the same 3.5 wt% NaCl solution that was used as the electrolyte during the experimental work of this thesis. The updated diffusion coefficients were received, and were seen to be significantly higher than the previous ones. With these new diffusion coefficients, a charging time of 24 hours was deemed sufficient, as shown in *Figure 91*.

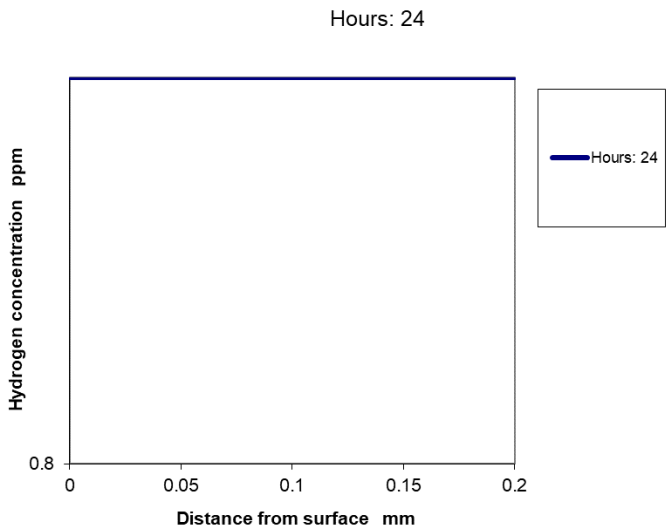

Figure 91 Hydrogen diffusion with updated diffusion coefficient

Appendix B – Estimate of Current Density

The wires from the potentiostat were fastened at both ends of the specimen as shown in *Figure 92*. The wire was used to polarize with a cathodic current of 550 mA. Liquid was assumed to be present between the grip component and specimen, and between the ceramic washer and the specimen, but not between the nuts and the specimen. Furthermore, liquid was not assumed to be present between the interfaces of the two nuts, nor between the interface of the ceramic washer and the octagonal nut. There was no metallic contact between the specimen and the grip component, due to the ceramic washer.

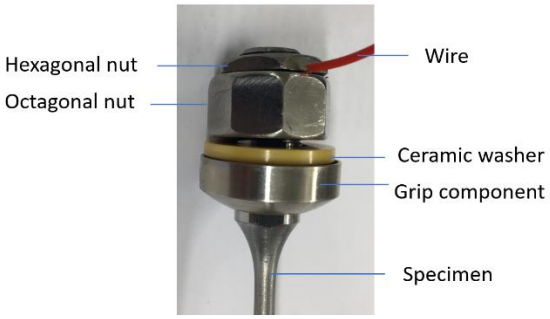

Figure 92 Assembly with marked components.

A simplified schematic sketch of the assembly is shown in *Figure 93*. The fillet area was assumed to be a cylindrical trapezoid, and the specimen was assumed to be fully circular.

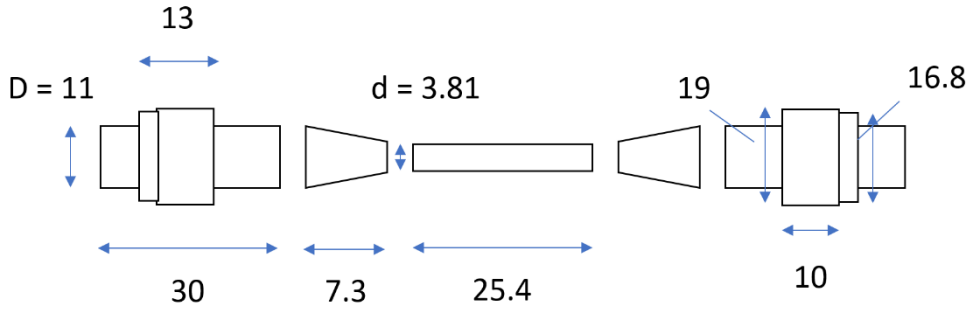

Figure 93 Sketch of assembly. All numbers in mm.

With the assumptions stated above, the polarized area of the specimen is estimated in *Equation 29*.

$$Polarized\ area = 2\ (cylinders + cross\ sections) + 2\ circular\ trapezoids + 1\ cylinder \quad (29)$$

$$2\left(\frac{\pi}{4}11^2 + \pi * 11 * (30 - 13)\right) mm^2 + 2 * \left(\pi\left(\frac{11+3.81}{2}\right)\sqrt{\left(\frac{11-3.81}{2}\right)^2 + 7.3^2}\right) mm^2 + \pi * 3.81 * 25.4 mm^2 = (1365 + 378.6 + 304)\ mm^2 = 2047.6\ mm^2$$

The polarized lateral surface area of both octagonal nuts is calculated in *Equation 30*.

$$Polarized\ area\ (two\ nuts) = 2 * Perimeter * Height \quad (30)$$

$$2\left(\frac{19}{2} * 2tan\left(\frac{180}{8}\right) * 8 * 10\ mm^2\right) = 1259.2\ \ mm^2$$

The polarized lateral surface area of both hexagonal nuts is calculated in *Equation 30*.

$$Polarized\ area\ (two\ nuts) = 2 * Perimeter * Height \quad (31)$$

$$2\left(\frac{16.8}{2} * 2tan\left(\frac{180}{6}\right) * 6 * 3\ mm^2\right) = 349.2\ \ mm^2$$

The polarized cross-sectional areas of all nuts are neglected. Thus, the current density is estimated in *Equation 32*.

$$Current\ density = \frac{550\ mA}{(2047.6 + 1259.2 + 349.2)\ mm^2} \quad (32)$$

$$= 15\ mA/cm^2$$